Ionic Conduction Mechanisms In Nano-Composite Electrolyte And Their Relationship To Micro-Structural Features

by Shalima Shawuti

Submitted to the Graduate School of Engineering and Natural Sciences in partial fulfillment of the requirements for the degree of Doctor of Philosophy

Sabancı University April 2014

Ionic Conduction Mechanisms in Nano-composite Electrolyte and Their Relationship to Micro-Structural Features

Shalima Shawuti

Materials Science and Engineering, PhD Dissertation, 2014

Dissertation supervisor: Professor Dr. Mehmet Ali Gülgün

Keywords: Nano-composite Electrolyte, Interface, Impedance Spectroscopy, SDC, SOFC

Abstract

This study is based on a nano-composite electrolyte that is made up of samarium doped cerium oxide (SDC) skeleton within a sodium carbonate matrix. These nano-composites have high ionic conductivities, even at temperatures as low as 400 °C. Our work revealed that the high interfacial interaction enhanced the ionic conduction behavior of the nano-composites by forming an interlayer between the oxide phase particles and the carbonate matrix which also provided structural connectivity. Consequently, the objective in this work is to address how the inter-phase affects

ionic transport mechanisms, and under which circumstances the ionic conduction properties can be improved, especially in a two-phase nano-composite.

The strength of influence of interfaces in ionic transport was also controlled by varying the amount of specific interface areas of the samarium doped ceria (SDC) particles in the nano-composite. In addition, the measurements conducted with composites with different amounts of the specific interface area of the SDC oxide particles in the electrolyte revealed insights into ionic conductivity of the composite. To control the value of specific surface area (SSA), the inverse relationship between the average particle size and SSA for SDC particles was employed. SDC particles with micron and nano-meter size distributions were mixed in order to obtain differing amounts of SSA in the composites between 47 $m^2.g^{-1}$ and 203 $m^2.g^{-1}$.

The micro-structural investigations with SEM and TEM revealed that the Na_2CO_3 phase served as the glue in the composite. The glass-transition-like behavior was apparent in the thermal response of the nano-composite at 350 °C. Furthermore, the experimental results demonstrated that the overall ionic conductivity below 400 °C was controlled by the SSA. The activation energies for ionic conductivity were determined in temperature range of 25-600 °C using the Arrhenius conductivity (σT) versus inverse temperature plots in order to identify the ionic conductivity mechanisms. The activation energies are consistent with the calculated dissociation energy of the carbonate phase. The spectral elemental mapping by TEM-EELS mode showed that carbonate phase constituted the majority of the matrix. A rim around the SDC oxide particles with a high concentration of carbon was imaged.

The strong dependence of the conductivity on the SSA, the differences in the activation energies, and spectral elemental mapping results suggested that the oxide surface acted as a dissociation agent for the carbonate phase. As a conclusion, the high ionic conductivities in the nano-composite electrolyte were the consequence of the oxide surface “liberating” ions, which can move more easily in the interaction region surrounding the oxide particles. The dependence of the ionic conductivity on the oxide particle amount was consistent with percolation type behavior of this interaction region, termed the “interphase” in this work.

Nano-Bileşik Elektrolitlerde İyonik İletkenlik Mekanizması ve Mikroyapısal Özelliklerle İlişkisi

Shalima Shawuti

Malzeme Bilimi ve Mühendisliği, Doktora Tezi, 2014

Tez Danismanı: Prof. Dr. Mehmet Ali Gülgün

Anahtar Kelimeler: Nano-Bileşik Elektrolit, Arayüzey, Empedans Spektrometresi, SDC, SOFC

Özet

Yapılan çalışma, sodyum karbonat matrisindeki samaryum katkılı seryuk oksit (SDC) iskeletinden yapılan nano-bileşik elektrolitler üzerinedir. Bu tip nano-bileşikler, 400 °C gibi düşük sıcaklıklarda bile yüksek iyonik iletkenliğe sahip yapılardır. Bizim çalışmamızda, karbonat matrisinin yapısal bağlantı sağladığı nano-bileşik tabaklar arasında oluşan oksit fazlarının iyonik iletimi arttırdığı anlaşıldı. Sonuç olarak yapılan çalismadaki temel hedef; fazlar arası etkileşimin iyonik iletkenlik mekanizması ve yüksek ara-yüzeylere sahip nano-bileşik tabakların, iyonik iletimlerindeki artışların sebepleri belirlendi anlaşılmasıdır.

Samarium katkılı seryum (SDC) parçacıkları nano-bileşikler içinde değişen miktarda karıştırılarak; bileşik içindeki özgün arayüzey alanlarının (SSA) iyonik iletime etkisi kontrol edildi. Buna ek olarakta; bileşik içindeki farklı miktarlarındaki SSA'ların iyonik iletimde arayüzeyin etkisini değiştirdiği belirlendi. SSA 'larını kontrol edebilmek için, ortalama parcacık boyutu ile SDC parçacıklarının SSA değerleri arasindaki ters ilişki kullanıldı. 47 $m^2.g^{-1}$ ile 203 $m^2.g^{-1}$ arasında SSA değerlerine sahip bileşikler elde edebilmek için, micron ve nano boyutta sahip SDC parcacıkların farklı karışımları kullanıldı.

SEM ve TEM ile yapılan mikro yapısal araştırmalar, Na_2CO_3 fazının bileşik içinde yapıştırıcı olarak hizmet ettiğini gösterdi. Nano-bileşiklerin termal değişim ölçümleri, 350 °C sıcaklık değerinde camsal yapıya dönüştüklerini belirledi. Ayrıca, yapılan elektriksel incelemeler, 400 °C sıcaklık altındaki genel iyonik iletkenliğin SSA tarafından kontrol edildiğini gösterdi. İyonik iletkenlik mekanizmalarındaki değişimleri sayısal tespit etmek amacıyla, aktivasyon enerjileri Arrhenius iletkenlik ($\sigma(T)$) eşitliği yardımı ile hesaplandı. Yapılan hesaplamalar, 25-600 °C sıcaklık aralığındaki elektriksel ölçüm sonuçları için yapıldı. Aktivasyon enerjilerindeki farklılıklar, karbonat fazına bağımlı hesaplanan ayrışma enerji değerleri ile tutarlıdır. TEM-EELS modu göre spektral element haritalama ölçümleri ile de yapısal matris içinde büyük çoğunluğu karbonat fazının oluşturduğunu gösterdi. Jant halindeki SDC parçacıkların, etrafında yüksek konsantre karbon resmedildi.

SSA değerine güçlüce bağımlı iletkenlik, aktivasyon enerjisindeki farklılıklar, ve spektral element haritalama sonuçlarına göre; oksit yüzeylerin, karbon fazları için ayrıştırma ajanı gibi davrandığını göstermektedir. Sonuç olarak, nano bileşik

elektrotlarda yüksek iyonik iletkenlikler, oksit parçacıkların çevrelendiği etkileşim yüzeylerinde kolaylıkla hareket edebilen oksit yüzeylerdeki "enerjik" iyonların sonucudur. İyonik iletkenliğin oksit parçacık miktarına bağımlılığı, etkileşim bölgesinde kararlılığını devam ettirmektedir. Bu bölge "arafaz" olarak adlandırılır.

Acknowledgement

I would here like to express my special thanks and my deep gratitude to the people during my stay in Sabanci University.

I have been very fortunate to work with my supervisor, Prof. Dr. Mehmet Ali. Gülgün, who motivated me keep improving both academically and personally during those four years. I want to express my sincere gratitude to him not only for opening the door of new and different life for me, but also for his unconditional support, invaluable guidance and of course for his immense patience. It was a great honor and a lifetime bless for me to work with him and to be a part of his group at SU.

I always enjoyed discussing science and daily life matters with my co-supervisor, Associate Prof. Dr. Cleva OW Yang, who helped me to gain deep insight into many important topics in solid state physics and thermodynamics. I am very much appreciating her helpful advices and encouragement which have made it possible to achieve the present form of my dissertation. Thank you for not only keeping me on a good track during my research, but also for being guru for everything.

My special thanks to Professor Dr. Yuda Yürüm and Professor Dr. Melih Papila, who honored me for accepting to be my Jury member. My special thanks to Associate Prof. Dr. Ebru Alkoy, from University of Maltepe, who honored me for accepting to be my Jury member and gave me useful comments.

I am very much obliged to thank my lab colleagues as well as friends Melike Mercan Yildizhan, Gülcan Çorapçioglu, and Dilek Çakiroglu for all the beautiful times we spend together. I am indebted to my colleagues and my friends at MAT-SU for providing a friendly environment. I am especially grateful to my ex-colleagues Dr.Çinar Öncel who helped me to understand most of the important tricks in ceramic processing at the beginning of my study. I would like to thank Dr. Saso Strum and Mr. Ömer Deniz (GYTE) for their valuable help on TEM measurements. I also would like to thank Dr. Bariş Yağci (Koç University) for kindly help on DLS measurements.

The administrative and technical secretary staff of SU-MDBF and SU-SUNUM, thanks for their guidance and assistance for all the administrative and technical matters. I am grateful to everyone who directly or indirectly involved and supported my research activities. I would like to acknowledge the financial and academic support of the Turkish Foundation for Fundamental Research (TUBİTAK) and Sabanci University.

Lastly, I would like to express my deep thanks to Dr. Musa Mutlu Can for being part of my life. Thanks for be with me on my most difficult times and keep motivate me to be strong.

I am especially grateful to my mum Roxian and my father Savut for raising me up, educating me, loving me with lots of prays. I thanks to my sisters, Gulixian and Rena, who keep protect me from my childhood, and guide me on both study and life,

support me with their best effort. For my niece Reyyan and Nephew Mustafa, for giving me lots of smiles.

Contents

Figure

Table

ABRIVATION

ASR:	Area Specific Resistance
BET:	Brunauer-Emmett-Teller
BSCF:	Barium and iron doped strontium cobaltite
BSE:	Back scattered electron
CGO:	Cerium Gadolinium Oxide
CN:	Coordination Number
DC:	Direct Current
DTA:	Differential Thermal Analysis
EDX:	Energy Dispersive X-Ray Spectroscopy
EIS:	Electrochemical Impedance Spectroscopy
EELS:	Electron Energy Loss Spectroscopy
FIB:	Focus Ion Beam
JCPDS:	Joint Committee on Powder Diffraction Standards
HDPE:	High density polyethylene
HR-TEM:	High Resolution Transmission Electron Microscopy
IT-SOFC:	Intermediate Temperature Solid Oxide Fuel Cell
LT-SOFC:	Low Temperature Solid Oxide Fuel Cell
LDC:	Lanthanum Doped Ceria
LPG:	Liquefied Petroleum Gas
LSC:	Strontium Doped Lanthanum Cobaltite
LSCF:	Strontium and iron Doped Lanthanum Cobaltite
LSF:	Strontium doped Lanthanum Ferrite
LSGM:	Strontium and magnesium doped lanthanum gallate
LSM:	Strontium Doped Lanthanum Manganate

RT:	Room Temperature
SCF:	Iron Doped Strontium Cobaltite
SDC:	Samarium Doped Ceria
SEM:	Scanning Electron Microscopy
SOFC:	Solid Oxide Fuel Cell
STA:	Simultaneous Thermal Analysis
SSSA:	Specific Surface Area
TEC:	Thermal Expansion Coefficient
TEM:	Transmission Electron Microscopy
TPB:	Triple Phase Boundary
TGA:	Thermal Gravimetric Analysis
YDC:	Yttrium Doped Ceria
YSZ:	Yttria Stabilized Zirconia
XRD:	X-Ray Diffraction
3D:	Three Dimensional

CHAPTER 1: INTRODUCTION

1.1. Fuel Cell Overview

Fuel cells (FC) may be an important enabling technology for the world's energy portfolio. They have the potential to revolutionize the ways we power our daily electronic equipment, tools, and even factories. Particularly household heating systems, small factories' energy systems, and the recycling of factory fuel sources rely on the FC [1]. The attractiveness of FCs lies in their abilities to offer a clean, efficient and quiet choice to the power stations that rely on combustion of other fossil fuels such as natural gas, gasoline etc. FCs are hoped particularly to replace the internal-combustion engine in vehicles. FCs offer electrical power in stationary and portable power applications. They are energy-efficient, clean, and fuel-flexible [1]. Current research and development now focus on eliminating the few remaining technical barriers left to FC commercialization which are related to high temperatures (T > 900 °C) required for their efficient use. Future research most likely would focus on the development of dependable, inexpensive, and high-performance FC system components for transportation. This study focuses on an alternative FC system that has a potential to bring the operating temperatures to more manageable temperature range of 300 °C to 500 °C.

1.1.1. Principles of the Fuel Cell

Fuel cells are electrochemical devices that convert chemical energy in fuels directly into electrical energy. A fuel cell is electrochemically similar to a battery; however, a fuel cell uses externally supplied fuels, while a battery consumes internal fuels to generate electricity.

A fuel cell can produce electricity continuously as long as the fuel is supplied; By contrast a battery needs to be recharged once the internal fuel is depleted [2]. In addition, fuel cells produce power with minimal pollutants and noise footprint. Therefore, fuel cells are considered as one of the most promising power generation devices [3].

Scientists and inventors have designed many different types and sizes of fuel cells in the search for greater efficiency; and the technical details of each kind vary. Many of the possibilities facing fuel cell developers are constrained by the choice of electrolyte. The choice of the electrolyte determines the decision on the cathode and anode candidates [3- 4]. The design and the materials of electrodes depend on the type of the electrolyte. Today, the main electrolyte types are alkali, molten carbonate, phosphoric acid, proton exchange membrane and solid oxide [4-6].

The type of fuel also depends on the electrolyte. Some cells need pure hydrogen gas, and therefore demand additional equipment such as a 'reformer' to purify the fuel. Other cells can tolerate some impurities but might need higher temperatures to run efficiently [7]. Liquid electrolytes circulate in some cells, which require pumping and they are mostly corrosive. The type of electrolyte also dictates a cell's operating temperature. ''molten'' carbonate cells run at high temperature (T >650 °C), just as the name implies [8]. Each type of fuel cell has advantages and drawbacks compared to the others, and none is yet cheap and efficient enough to widely replace traditional ways of generating power, such coal-fired, hydroelectric, or even nuclear power plants [3].

1.2 Types of Fuel Cell

Generally FCs are categorized by the electrolyte materials used, such as proton exchange membrane fuel cell (PEMFC), alkaline fuel cell (AFC), phosphoric acid fuel cell (PAFC), molten carbonate fuel cell (MCFC), and solid oxide fuel cell (SOFC). A comparison of different kinds of FCs is listed explicitly in table 1 [6, 9,10].

Table 1.1.Comparison of the types of fuel cell [6, 9, 10].

Fuel Cell Types	Type of Electrolyte	Temperature (°C)	Electrical Efficiency	Advantage	Disadvantage
PEM	Polymer solid membrane	50-100	53-60% (mobile) and 25-35% (stationary)	Low operating temperature; Absence of corrosive liquid electrolyte; Fast start up; Simple cell structure; cost	Low CO tolerance; Drying of membrane; Waste heat has low values

AFC	Aqueous alkaline	50-200	60 %	Mature technology; Very reliable; High efficiency; Low cost materials	Not CO_2 tolerant
PAFC	Phosphoric acid	200-250	40%	Mature technology; Very reliable; Fast responsive time; High efficient with partial load	Too expensive; waste heat has low values; rather low efficiency; CO≤1%,
MCFC	Molten carbonate	600-700	45-47%	High efficiency; CO tolerant; Internal reforming; No noble metal catalysts; High quality waste heat	Material problems of cell and stack components; CO_2 circulatio; S tolerance is low
SOFC	Solid oxide	500-800	45-70%	High efficiency ; high quality heat waste; simple system; without reformer, fuel flexible; High sulphur tolerance	Still expansive; Thermal expansion Porosity Temperature gradients; Mixed conduction

1.2.1 Working Principles of SOFCs

SOFCs are popular among the different types of fuel cells because of their high energy conversion efficiency and fuel flexibility. However, the current SOFC technology operating at around 1000 °C is costly and would benefit from new materials that can work more efficiently at lower temperatures [11]. Current SOFCs still operate at high temperatures and therefore employ ceramics as functional elements of the cell. There are three basic components of a single SOFC: a porous anode, a dense electrolyte, and a porous cathode. Its electrolyte is a solid oxide [11-15].

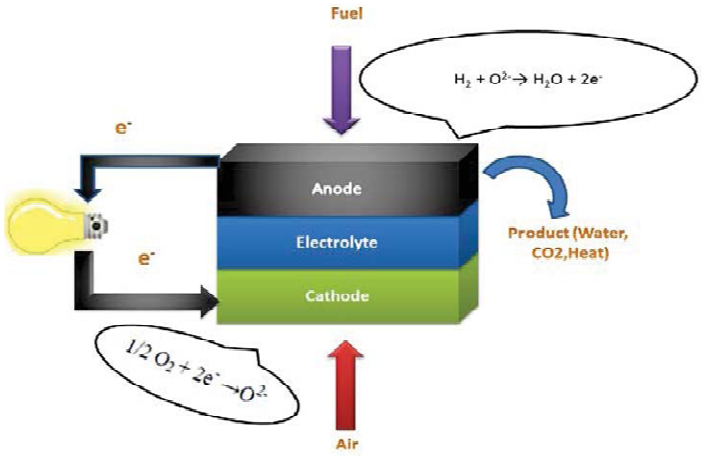

Figure 1.1. Working principle of Solid Oxide Fuel Cell (SOFC) [16].

The working principle of the SOFC is shown in Figure 1.1. Typically, oxygen atoms are reduced on the porous cathode surface by electrons, generating oxygen ions. Under the chemical potential between the anode and the cathode, the oxygen ions diffuse through the ionic conductor electrolyte to the fuel-rich and porous anode, where they will meet and react with the fuel (H_2) and release electrons (e′) to an external circuit. Thus, the final products of an SOFC will be electricity, heat and water. The reactions at the cathode can be expressed as in the following Equation (1.1) [1],

$$½\ O_2\ (g) + 2e' = O^{2-} \qquad \text{Equation (1.1)}$$

where O^{2-} is the mobile oxygen ion. Oxygen in the gas phase is reduced to oxide ions, consuming two electrons in the process. The reactions at the anode can be expressed as in the following Equation (1.2) [1],

$$O^{2-}\ (s) + H_2\ (g) = H_2O\ (g) + 2e^- \qquad \text{Equation (1.2)}$$

In summary, the electrical work that can be generated from chemical reactions by the fuel cell is determined primarily by the difference in the electrode potentials, but limited by the mobility of the charge carriers.

1.2.2 The Current Status of SOFCs

SOFCs are efficient (fuel input to electricity output) electricity generators currently being developed world-wide. They are flexible in the choice of fuel such as carbon-based fuels. SOFCs can also be fuelled by externally reforming heavier hydrocarbons, such as gasoline, diesel, or bio-fuels [17]. Such reformates are mixtures of hydrogen, carbon monoxide, carbon dioxide, steam and methane, formed by reacting the hydrocarbon fuels with air or steam in a device upstream of the SOFC anode [11-14]. SOFC technology is most suited to applications in the distributed-generation (*ie.,* stationary power) market because it's high conversion efficiency. It provides the greatest benefit when fuel costs are higher, due to long fuel delivery systems to customer premises. SOFCs have a modular and solid state construction and do not contain any moving parts. They are quiet enough to be installed indoors. The high operating temperature of SOFCs produces high quality "heat by-product" which can be used for co-generation, or for use in combined cycle applications. They do not contain noble metals that could be problematic in resource availability and price issue in high volume manufacture. They do not have problems with electrolyte management (liquid electrolytes, for example, which are corrosive and difficult to handle) [18]. SOFCs have extremely low emissions by eliminating the danger of carbon monoxide (CO) in exhaust gases, as any CO produced is converted to CO_2 at the high operating temperature. SOFCs have a potential long life expectancy of more than 40,000–80,000 hours [19]. SOFC power systems can increase its efficiency by using the heat given off by the exothermic electrochemical oxidation within the

fuel cell for endothermic steam reforming process. Theoretical efficiency of a SOFC device can exceed 60 % [20]. To sum up, the high operating temperature makes SOFCs suitable candidates for application with heat engine energy recovery devices or combined heat and power generation, which further increase overall fuel efficiency.

However, there are several disadvantages of current SOFCs due to their high operating temperature. Current SOFC's most fuel-efficient operating temperature is at 1000 °C. Unfortunately, this high temperature decreases the cell lifetime and increases the cost of the cell stack due to expensive materials. For example, expensive high-temperature alloys are used to house the cell, and costly ceramics are used for interconnects, increasing the cost of the fuel cell stack substantially [6].

Lowering operating temperature has been recognized worldwide as the main issue for low-cost and low-temperature SOFCs. The reduction in the temperature will allow the use of cheaper interconnecting and structural components. The aim is to use stainless steel. A lower temperature will also ensure greater overall system efficiency and a reduction in the thermal stresses in the active ceramic structures. Thus, it leads to a longer expected lifetime of the system [21, 22]. The critical issue is to reduce operating temperature without reducing SOFCs performance. The cell performance is very sensitive to operating temperature. A 10 % drop in temperature results in 12% drop in cell performance due to an increase in the internal resistance to the flow of oxygen ions [23]. The high temperature also demands that the system include significant thermal shielding to protect personnel and to retain heat. An extensive range of research effort has been devoted to develop alternative electrolyte materials for SOFCs that operate at low temperatures, such as 400-500 °C [10].

1.3. Fuel cell Component Requirement

Table 1.2 illustrates the requirement for each SOFC component. The electrolyte is the principal component of importance for SOFC. An ideal SOFC electrolyte should have the following characteristics: high ionic conductivity; low electronic conductivity; good thermal and chemical stability in relation to the environment and the contacting electrode materials; closely matched thermal expansion coefficients between the electrodes and contacting components; fully dense structure to maximize conductivity and minimize cross-over of reactants; low cost and environmental friendliness [4-6, 10].

Table1.2. Requirement For The Fuel Cell [4, 5,6,10].

FC Component Requirements	Catalytic Activity/Cost	Conductivity	Density/ Porosity	Compatibility	Stability
Electrolyte	Lower cost	High ionic conductivity and negligible electronic conductivity	Fully dense and gas tight	Thermally, chemically, and mechanically compatible with electrodes	Chemically, morphologically, and structurally stable in fuel and oxidant
Anode	High catalytic activity and lower cost	Mixed conductor: high e electron but low ionic conductivity electronic conductivity to transfer (10:1)	Porous for mass transport of gases	Thermally chemically compatible with electrodes to prevent the segregation and crack	Chemically, morphologically, and structurally stable in fuel environments
Cathode	High catalytic activity and low cost	Mixed conductor: High electronic conductivity and lower ionic conductivity	Porous for mass transport of gases	Thermally chemically compatible with electrodes	Chemically and structurally stable in oxidant environments
Interconnect	Lower cost	High electronic, conductivity, with no ionic conductivity	Fully dense	Thermally compatible with electrode to prevent the crack of cell	Stable in fuel and oxidant

1.4. Electrolyte Materials

Materials with the fluorite crystal structure, such as zirconia-based oxides and ceria-based oxides [24], and materials with perovskite structure, such as $LaGaO_3$ based materials are the most commonly used oxygen ion conductor electrolyte materials for SOFC [25,26]. A common feature of those oxides is capability of hosting various dopants. Introduction of dopant ions produces a material with a high concentration of mobile oxygen vacancies and thereby high oxygen ion conductivity.

1.4.1. Conventional Electrolyte Materials for SOFC

Many of the common classical oxygen ion conductors (electrolyte material) are fluorite-type oxide, which is defined with the general formula of AO_2. The fluorite crystal structure (see Fig. 1.2) is a face-centered cubic arrangement of cations with oxygen ions occupying all the tetrahedral sites, leading to a large number of octahedral interstitial voids. The addition of cations with lower valence than the host cation produces oxygen vacancies, resulting in improved oxygen ion conductivity [27]. For example, cubic zirconia (c-ZrO_2) has the fluorite structure and addition of 8 mol% of yttria i.e. $(ZrO_2)_{0.92}(Y_2O_3)_{0.08}$ (8YSZ) leads to the highest oxygen ion conductivity (0.06071 $S.cm^{-1}$@1073K). Yttria stabilized zirconia (cubic YSZ) is the most commonly used electrolyte for SOFCs, which has good chemical and physical stability as well as negligible electronic conductivity [28]. Similarly, scandia stabilized zirconia (SSZ) also attracted some attention due to its improved conductivity. In addition to ZrO_2, doped cerium oxide (DCO), is also considered to be a promising electrolyte for LT-SOFC [29]. Samarium doped ceria (SDC) and gadolinium doped ceria (GDC) are the most extensively studied ceria based electrolytes, with the maximum ionic conductivity occurring

at 10–20 mol% dopants. Compared to YSZ, DCO has a higher conductivity and lower activation energy below 800 °C [29]. However, DCO suffers from the partial reduction of Ce^{4+} to Ce^{3+} in reducing atmosphere and at high temperatures (≥600 °C). DOC undergoes an undesirable structural change and has an electronic conductivity that reduces its performance due to electronic leakage currents between the anode and cathode [30].

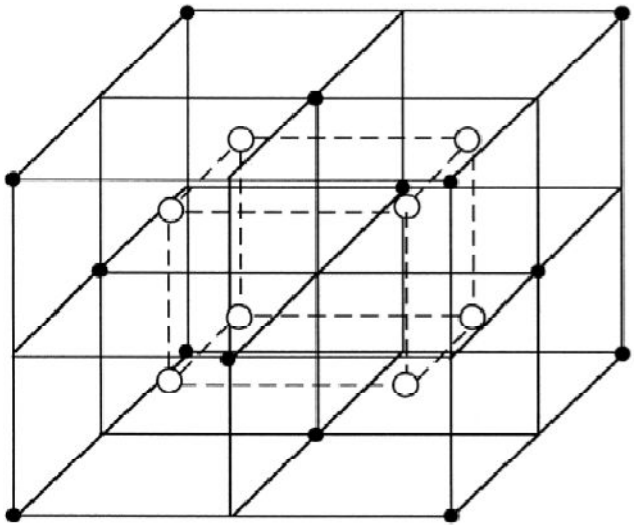

Figure 1.2. The fluorite crystal structure [31]. (Black close dots represent cations, open circles represent oxygen).

Perovskites are one of the most versatile classes of solid oxide materials. Perovskite structured oxide, which has the general formula of ABO_3 with an oxygen face-centering. In ABO_3 structure, A and B are the cations of very different sizes and O is the anion that bonds these two cations. The A site cation is larger than the B site cation. The ABO_3 perovskite structure is extremely amenable to doping on both the A and B cation sites. A large variety and concentration of dopants can be accommodated in a wide range of host compounds. Introduction of divalent dopant ions, typically Sr and Mg ions, on to the La and Ga sites, respectively, of lanthanum gallate produces a material with a high concentration of mobile oxygen vacancies and thereby high oxygen ion conductivity [31]. The exceptionally high

conductivity of the particular composition La0.9Sr0.1Ga0.8Mg0.2O3-d (LSGM) was reported by Goodenough and co-workers and by Ishihara and co-workers [31]. The transport properties of LSGM, as it is known, are comparable to those of scandia-doped zirconia. The conductivity is entirely ionic over an extremely wide oxygen partial pressure range at temperatures as high as 1000 °C. However, it is not as high as that of a doped ceria. Thus, the conditions under which LSGM might be preferable to doped ceria appeared to be limited to the temperature range of 700–1000 °C. Moreover, lanthanum gallate suffers from the reactivity with nickel, the typical SOFC anode electro-catalyst. To address this issue, ceria buffer layers (LDC) have been incorporated between the electrolyte and the anode [32].

1.4.2. Limitation of SOFC Conventional Electrolyte Materials

There are also some disadvantages of the single phase electrolyte materials.

$$\sigma\sigma(T) = \frac{\sigma_0}{T}\left(-\frac{E_a}{K_B\,T}\right) \qquad \text{Equation (1.3[33])}$$

where T indicates the absolute temperature, K_B the Boltzmann constant, E_a the activation energy. Within the crystal structure unit, a strong interaction between oxygen ions and cations contributes to the major part of the high E_a values on the order of 1.0 eV (although around 0.5 eV is required for super ionic conduction [33]). Therefore, such structural effects put strong limitations on the conventional SOFC materials. They result in a high activation energy, low oxygen ion vacancy concentration, and mobility. Thus, a high temperature is required to activate a sufficiently high ionic mobility [34].

In order to enhance the conductivity of electrolytes, the concept of heterogeneous doping has been applied.

1.4.3. Heterogeneous and Doped Liquid Electrolyte

Networks of inorganic particles formed within organic liquids play an important role in electrolytes for Li-based batteries with a fascinating combination of mechanical and electrical properties [35]. A new class of ionic conductor composites consists of dispersions of solid insulating oxide particles (*e.g.*, SiO_2, Al_2O_3,etc.) into liquid non-aqueous lithium salt solutions (*e.g.*, $LiClO_4$ in MeOH, THF etc.). Usually, oxide particles with sizes in the range from 5-300 nm were employed in such composite [36-40]. The variation of conductivity with oxide fraction shows a percolation type of behavior like the one depicted in Figure 1.3 for ionic conductivity, which is typical for interfacial phenomena (*i.e.*, in this case, conductivity).

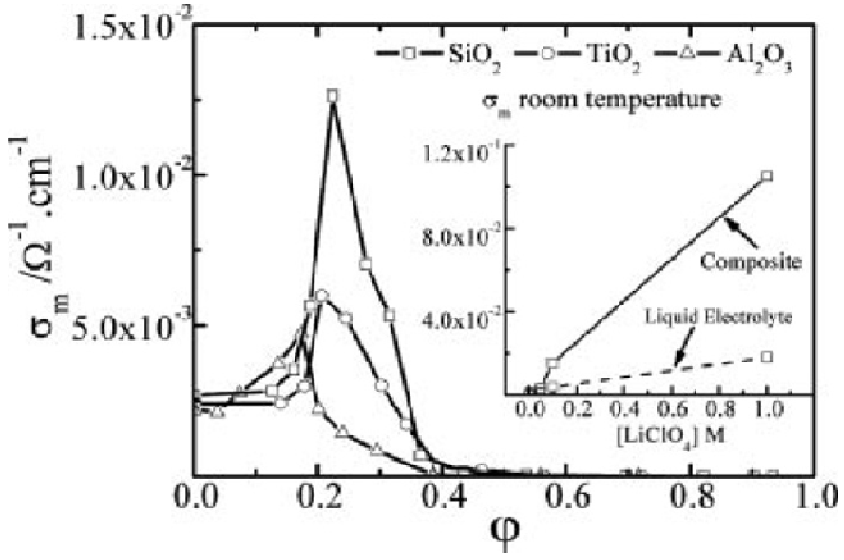

Figure 1.3. Room temperature variation of composite conductivity versus volume fraction (φ) of various oxide with different surface acid-base character in 0.1 M $LiClO_4$/ MeOH solution.

Inset: Variation of $LiClO_4$-MeOH solution and of composites with SiO_2 as a function of $LiClO_4$ concentration ($\varphi \sim 0.28$) [36].

In the regime of high conductivity, the composites possess favorable mechanical properties of soft matter similar to that of 'Soggy Sand', such as favorable viscosity [41]. By dispersing fine oxide particles such as silica nano-particles in non-aqueous liquid solutions, 'Soggy Sand' electrolytes have higher ionic conductivity and increased viscosity at constant shear rate compared to the neat liquid electrolytes. These beneficial features make these 'Soggy Sand' electrolytes promising for application in electrochemical devices such as rechargeable lithium batteries and Dye-Sensitized Solar Cells (DSSCs) [36,40-41].

For these composites, the conductivity behavior changes with the amount of second phase oxide contents (φ). It is comprised of approximately three regimes: i) the colloidal regime ($\varphi \leq 0.2$) with low enhancements; ii) ''Soggy Sand'' ($0.2 \leq \varphi \leq 0.5$), the regime with the highest conductivities and iii) dry sand, where the composite exhibits lower conductivities compared to the non-aqueous solution matrix [36]. Figure 1.3 refers to a solution of $LiClO_4$ in methanol and shows the remarkable variation in the overall effective ionic conductivity with volume fraction (φ) for different oxides. In all cases, the composite conductivity exhibits a percolation type behavior, which is expected for composites with enhanced interfacial conductivity, *i.e.,* low conductivity at low oxide content, a pronounced increase with marked maximum and subsequent decreases at higher volume fraction [42]. In the lower oxide fractions (such as colloidal regime), the double layer repulsions work against percolation and leads to poor conductivities. As soon as the particles are forced into a sufficiently narrow spacing, the interfacial conductivity percolates. At very high volume fraction, the insulating spherical particles should be in direct contact and creating porosity in between, eventually

leading to blocking of the pathways by dry oxide particles. The blocking is occurring quite abruptly and comparatively early indicating pronounced non-homogeneities [36].

The ionic conductivity magnitude of the liquid electrolyte also depends on ion association, solvent dielectric constant, solvent viscosity and surface acidity of the oxide [42]. Figure 1.3 also shows that the composites conductivity is highly influenced by the change of surface acid-base property of the oxides. The conductivity improvement is higher for the acidic oxide SiO_2 (pH of zero charge in aqueous solution (pzc) ~3) when compared to the more basic Al_2O_3 (pzc ~8.1), while TiO_2 (pzc ~5) shows an intermediate response. This influence of iso-electric point suggests that the conductivity enhancement in the liquid-solid composite can be attributed to an adsorption of anion to the oxide surface. This adsorption would break-up the ion pair, leading to an enhanced Li^+ concentration in the charged double layer surrounding the oxides. Even more importantly, the ability of Li^+ ions to move can be significantly increased when the counter ion is immobilized [43].

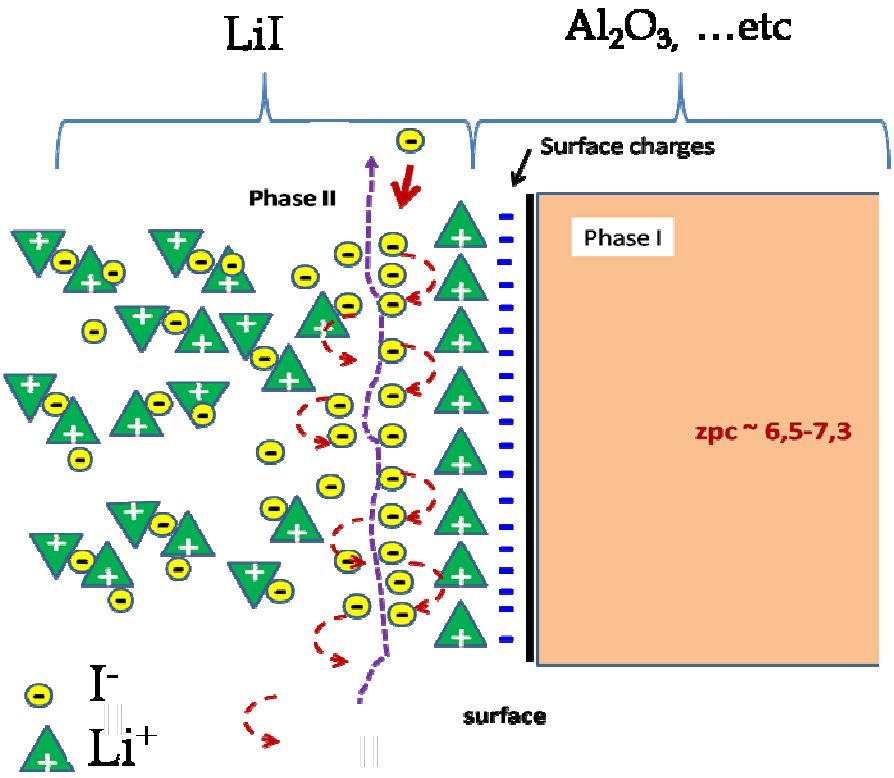

Figure 1.4. Schematic of the soggy and composite electrolyte where the oxide surface charge is slightly negative.

The Figure 1.4 explains how the soggy sand works in the composite. For example, in the case of a basic oxide, such as Al_2O_3 dispersions in LiI, Li^+ ions are adsorbed at the oxide surface, leading to an increased vacancy concentration in the Li sub-lattice in Figure 1.4. On the other hand, in the case of acidic oxide, such as SiO_2 anion adsorption at the SiO_2 surface leads to breaking up of ion pairs; thus, increasing the concentration of free Li ions and the Li^+ surface conductivity. Since this effect can be related to preferential ion diffusion along the network of the insulating particles, these electrolytes rely on the formation and stability of an interconnected network of surfaces [44].

In general, the un-dissociated ground state is broken up, and the counter carrier, that is ClO_4^-, in this case, set free Li^+. In the context of liquid electrolytes, the "ground state" is the un-dissociated ion pair, which does not contribute to the Li^+ conductivity [44]. Hence, adsorption of the anion (if acidic oxide, such as silica) will lead to dissociation of the LiX ion pair and enhancement of Li^+ ions in the space charge layer in the vicinity of the oxide layer. In the heterogeneously doped solid electrolytes, conductivity enhancement was attributed to a space-charge layer with an enhanced carrier concentration and an almost temperature-independent interfacial concentration [44].

1.5. The Effect of Microstructure on Ionic Conductivity

Most of the ceramic electrolytes are polycrystalline and consist of grains, grain boundaries and pores. Thus, the microstructure of the electrolyte influences oxygen ion conductivity. Grain boundary often also has a predominating role on influencing on overall properties [45]. Therefore, studies of the grain boundary behavior are essential to design ceramic materials and to optimize the ionic conduction properties. In conventional polycrystalline solid electrolytes, the grain boundaries partially hinder the ionic transport, causing an extra contribution to the total resistance. Thus, the total conductivity decreases with decreasing grain size. Grain boundaries or interior contacts between the particles are usually barriers that limit the ionic conductivity since the grain boundary conductivity could be much lower than that of the grain; thus, it may block the ionic transport [46]. The grain boundaries are also the location of lower oxygen vacancy concentration. Still, both grains and grain boundaries contribute to the conductivity of the polycrystalline electrolyte. Figure 1.5 displays schematically the situation in a polycrystalline electrolyte, where the continuous grain

boundaries' network with high resistivity surrounds the grains. The schematic illustrate that the micro-structure is very important for optimizing the ionic conductivity [47].

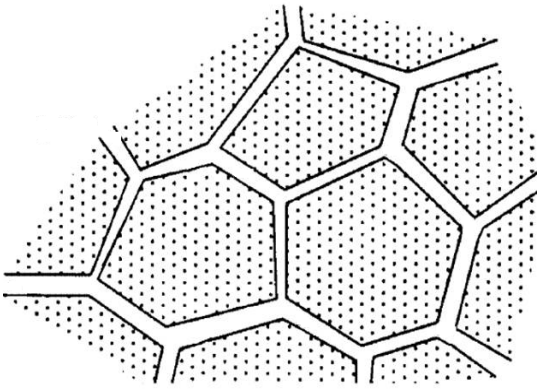

Figure 1.5. A schematic of continuous grain boundaries network that are highly resistant surround grains in the polycrystalline electrolyte [47].

The micro-structural morphology plays an important role in determining the conductivity [46]. Therefore, importance should be placed on the engineering of the grain boundaries by enhancing the local charge carrier concentrations at the grain boundaries. Highly conductive materials can be obtained by lowering the grain boundary resistance. Thus, engineering of the grain boundaries is essential in improving the materials' ionic conductivity [48]. However, when discussing of nano-sized materials the conductivity is different. Recent developments on nano-size materials for the conventional SOFC electrolytes support this new paradigm. Studies have shown that the nano-structured ceria-based materials and YSZ exhibited high conductivity enhancement, due to significantly larger area of grain-boundary and/or interface, which increases the concentration of the mobile ions defects in the space-charge zone [48]. The ionic conduction in the grain-boundary was claimed to turn from a negative effect in the micro-meter sized materials to a positive effect in the nano-sized materials. These new shifts in paradigm disagree with the conventional single phase SOFC materials as described in

Section 1.2.

It is argued that the reduced particle size may cause completely different ion transport phenomena [49]. In the micrometer sized particle, the grain boundary blocks the ion transport ways, thus leading to a highly resistive gap between the grains. The ions migrate from one grain into another forming a discontinuous path and causing low ion conductivity (see Figure 1.5) [47]. Therefore, in the conventional materials, the approach is to limit the grain boundaries to a minimum level in order to obtain high conductivity material. However, when the grain sizes are reduced to nanometers, a different observation was made. The situation changes to the opposite direction where the grain boundaries appeared become ion conduction highways [47]. Grain boundaries in the nano-sized single phase materials and interfacial contacts in the two phase materials were optimized for high ionic conductivity. In the micrometer-sized materials, the O^{2-} ions can migrate through the grains; while for the nano-scale materials it was suggested that, the significantly small size difference between the mobile ions and the grains lead to a strong expulsion force to resist the O^{2-} migration as the ion approaches the grain. Therefore the observed high values of ionic conduction were explained by grain boundaries or interface path leading to a 'fast-path' for ions to move around the grains [47]. Nano-structured materials were suggested to enhance the conductivity due to highly conductive grain-boundary effects. However, the single phased and nano-sized when oxide conductors are single phased and are made up of nanometer sized grains; they are not stable, especially at high temperature SOFC environment. The nano-structured single phase materials, such as, YSZ and doped ceria may not function properly at high temperatures. Those high temperatures together with strong reducing and oxidizing environments can easily destroy the nanostructures. Furthermore, in the nano-sized ceria based electrolytes, the following negative effects might occur [49];

1. Transition from ionic to e^- conduction when the particle turns to the nano-scale,
2. Electronic conductivity increases for the nano-sized particle,
3. Ionic activation energy, E_a may also be increased with decreasing grain sizes.

Thus, the single phased nano-ceria materials may not be used in SOFCs at all temperatures. Hence, the development of stable and functional nano-materials suitable for SOFC electrolyte applications is still an open field of research for materials science.

1.6. Composite Electrolyte for SOFC

Composite electrolytes are physical mixtures consisting of two or more solid phases that possess different ionic conductivity properties. Studies illustrated that composite electrolytes have enhanced ionic conductivity [10-11,30,46, 50]. The enhanced effects were not the result of simple addition of two constituent phases; rather they were synergistic in the way that the total conductivity was significantly higher than in both of the constituent phases. The conductivity enhancement effects of composite electrolyte were first reported on LiI:Al_2O_3 composite in 1973 by C. C. Liang [35]. Since then, extensive research has been performed to investigate the conductivity improvement effects of diverse composite systems. For instance, insulator-conductor systems (dispersing an insulating oxide like Al_2O_3, SiO_2 in a moderate ion conductor like Li^+) and conductor-conductor system (Ag^+ conductivity enhancement in AgBr-AgI; nano-sized ionic CaF_2/BaF_2 hetero-structures) are key examples [40-45]. The conductivity improvement, also called the composite effect, was suggested to be due to high ionic conductivity in the interface region between components [40-45].

In the recent years, for the development of new solid electrolytes for LT-SOFC, the composite approach has been actively utilized. Good example is the ceria-based composite electrolyte. In the last decade, much work has been done to develop alternative electrolytes for LT-SOFC with this composite approach [41-45]. These composite materials mainly consisted of two-phases: the host phase (ceria-based oxide) and second phase (various salts). Numerous combinations of dopants have been used on various ceria-based composites (such as SDC, GDC, and YDC), which were incorporated with different salts and hydrates (such as chlorides, fluorites, carbonates, sulphates). (See Table 1-2) [30].

1.6.1. Composite Electrolyte and Performance

The ceria–based composite electrolytes have displayed a high ionic conductivity of 10^{-2}–1.0 $S.cm^{-1}$ and excellent fuel cell performances between 300–1100 mW cm^{-2} at 400 – 600 °C. The development of ceria–based composite electrolyte has led to a new horizon in the LT-SOFCs research field. The conductivities of the composites with different oxides are listed in the Table 1.3 [51].

Table 1.3.Conductivity and FC performance of ceria-based composite electrolytes [51].

Doped Ceria	Second phases	Conductivity ($S.cm^{-1}$)	Temperature (°C)
GDC	20wt% (1LiCl:1 $SrCl_2$)	0.015-0.21	400-600
GDC	15wt%NaOH	0.02-0.45	380-620
GDC	22wt% (2$LiCO_3$:1 Na_2CO_3)	0.01-0.80	400-660
SDC	20wt% (1LiCl:1 $SrCl_2$)	0.02-0.24	380-660
SDC	15wt%NaOH	0.03-0.50	400-660
SDC	22wt% (2$LiCO_3$:1 Na_2CO_3)	0.002-0.90	400-660
SDC	40mol%Li_2SO_4	0.01-0.40	450-650
YDC	22wt% (1$LiCO_3$:1 $SrCl_2$)	0.01-0.18	400-660
YDC	15wt%NaOH	0.02-0.40	380-620
YDC	22wt% (2$LiCO_3$:1 Na_2CO_3)	0.01-0.78	400-660

In the literature, the composite electrolyte for LT-SOFCs was defined as a two phase material, which exhibits multiple functions and unique characteristics [47]. These unique characteristics were listed as follows;

1. The composite electrolyte consists of two-phases with interfaces. The material functionalities are created through the two-phase interfacial regions at the nano-sized oxide phase.
2. The ionic transport phenomena differ from the conventional bulk effects, which do not play a major determining role in two-phase composite electrolytes. Instead, the interfacial mechanisms and/or fast super-ionic conduction through the interfaces determine the overall electrical properties [47].
3. Together with interfacial super-ionic conduction, the source ions (O^{2-} and H^{+}) significantly enhance SOFC power output at 300-600 °C.
4. Interfacial and surface redox reactions might provide new opportunities for the further development of functional nano-composites for advanced fuel cell technology.

Ceria based carbonate composite electrolytes can be used as a prototype of the new nano-composite FCs. Such composite electrolyte has been considered to be a new class of ionic conductors due to their high conductivity at low temperature. It is suggested that ionic transport occurs via interfaces; thus, make these materials promising potential applications in LT-SOFCs [52, 53]. With the enhanced ionic conductivity, ceria based composite electrolytes could achieve good performance when used together with compatible electrode materials. So far, the mixtures of NiO and composite electrolyte have been widely used as the anode materials while lithiated-NiO was commonly used as the cathode material. Table 1.2 above gives the summary of the conductivity and FC performances for various ceria-based

composite electrolytes [51]. The large variety of fuels, such as biomass, nature gas, coal gas, alcohol and ammonia were directly fed and operated for the ceria-based composite electrolyte IT/LT-SOFCs. Table 1.4 listed FC performances using ceria-based composite materials operated by various fuels [51].

Table 1.4. Performance of SDC-carbonate composite electrolyte cell with various fuels [51].

Fuels	Performance ($W.cm^{-2}$)	Temperature (°C)
H2	0.98	600
Natural Gas (10%H_2)	0.68	660
Coal Gas (syngas)	0.72	660
Biomass Gas (syngas)	0.45	600
CH_3OH	0.35	600
C_2H_5OH	0.31	600
CH_3COCH_3	0.11	660
Alcohol	0.1-0.3	620
Ammonia	0.62	620

The enhanced oxygen ion conductivity was explained by an interface conduction mechanism [49,51,54]. Compared with the single phase electrolyte (SDC and YSZ), the composite electrolyte contains a high amount of interface regions between the two constituent phases. Thus, the interface may supply a conduction pathway for ionic conduction, which has the capacity to increase mobile ion concentration above that of the bulk [55]. The defect concentrations can be much higher in space charge zones near phase boundaries than that in the bulk. These space charge regions were suggested to account for higher ionic diffusivity and mobility than the defect contributions in the bulk would [55].

From the solid and ionic electrolyte point of view, the ceria based carbonate electrolyte system was regarded as a multi-ion transport system. Extensive work has been performed to understand the ionic transport process in the ceria based carbonate electrolyte. The research

output in the literature implied that the SDC carbonate electrolyte system could be a pure proton conductor under the controlled source environment composition [46].

In general, the so-called nano-composite electrolytes are composed of doped ceria particles embedded in alkali salts (carbonate, chloride, hydrate, or sulphate) [46,47]. The existing knowledge in scientific literature presumes that oxide particles provide a skeleton for containing the carbonate phase at the operating temperatures (400 °C-650 °C). Furthermore, it is assumed that such nano-composite electrolytes remained as two stable phases under the optimized operating conditions [46,55]. Impressively, this type of composite electrolyte has achieved a conductivity of 0.1 $S.cm^{-1}$ at 600 °C, attributed to the co-transport of H^+ ions and O^{2-} ions [50, 56]. Because of these remarkable characteristics, the leading candidate electrolyte for a new generation of fuel cells is doped ceria nano-composites. Tang *et al*. investigated the morphological and electrical properties of composites with particle sizes varying from the micrometer to the nano-meter size scale. They found that nano-composite have significant lower impedance values compared to the micron-sized composite [57]. Liu *et al.,* have proposed that the interface layers between SDC and Na_2CO_3 matrix were the origin of the enhanced conductivity [58]. According to their findings, the interfaces would allow a 'dual' conduction mechanism through the composite, via H^+ and O^{2-} transport. Furthermore, the pathways for H^+ ions were suggested to exist along the interface between the components phases [58]. The O^{2-} transport was assumed to occur through the interconnected SDC phase. In the composite electrolyte cell, water was formed within a porous mixed oxygen ion and proton conductive layer sandwiched by two respective dense oxygen ionic and proton conductive membranes. In this suggested model, the oxygen ion and the proton would meet in the porous mixed conductive layer, producing water. This reaction was suggested as the reason for the enhanced ionic conductivity due to the high number of charged species.

Benamira *et al.*, [59] suggested that the OH^- was formed by the following chemical reaction (Equation 1.4-1.7):

$$H_2O + O^{2-} = 2OH^- \quad \text{Equation (1.4)}$$

While H_2O was produced from the oxidation reactions:

$$H_2 + (CO_3)^{2-} = H_2O + CO_2 + 2e^- \quad \text{Equation (1.5)}$$

$$H_2 + O^{2-} = H_2O + 2e^- \quad \text{Equation (1.6)}$$

In addition, the water can form when H^+ and O^{2-} meet in the cell [45]

$$2H^+ + O^{2-} = H_2O \quad \text{Equation (1.7)}$$

Even though the formed H_2O may not be in the liquid form at such a high temperature (*i.e.,* 600 °C), H^+ conduction might actually be promoted and might occur through proton transfers along the network [60]. No explanation was given about the pressure build up within the cell if water was to form at such high temperatures. The kinetics of these reactions has led to further investigations concerning the type of transported ion. Additionally, formation of water on both anode and cathode sides were interpreted to be due to dual ions (H^+ and O^{2-}) transports in the same cell at the same time.

According to theoretical calculations, conductivity of the composite electrolyte depended on the volume ratio of SDC to Na_2CO_3. In theoretical studies, Liu *et al.* have proposed that the interface layers between SDC and Na_2CO_3 matrix are the origin of the enhanced conductivity [15]. According to their findings, the interfaces would allow a 'dual' conduction mechanism through the composite, via H^+ and O^{2-} transport. Furthermore, the pathways for H^+ ions were

suggested to exist *along the interface between the component phases* [15]. The O^{2-} transport was assumed to occur through the interconnected SDC phase. According to theoretical calculations, conductivity of the composite electrolyte depended on the volume ratio of SDC to Na_2CO_3. Another study suggested that H^+ transport occurring along the "implied" interface dominated ionic conduction inside the electrolyte in the temperature range between 300 °C and 600 °C [58]. A conductivity of 0.1 $S.cm^{-1}$ was reported for a 20 wt% SDC-Na_2CO_3 nano-composite electrolyte at 300 °C [10, 49, 60]. This was the optimum carbonate amount in the composite according to the Zhu *et al.* [58]. It was argued that conductivity resulted neither from the SDC or from the Na_2CO_3 phase, as individual SDC and Na_2CO_3 phases are good electrical insulators at ~300 °C [58]. No other phase was detected in the composite. Hence the interface formed between the two phases was proposed to serve as a new conduction pathway for the nano-composite, offering on one hand a high-conductivity pathway for ionic conduction, and on the other hand, a presumed capacity to increase mobile ion concentration beyond that of the bulk [58]. No mechanisms have yet been suggested for either phenomenon. Furthermore, Wang et al. claimed that the high conductivity of the nano-composite electrolyte was attributed to interfacial oxygen ion conduction rather than to bulk oxygen ion conduction [55]. The conduction across the interface was claimed to require low activation energy for O^{-2} transport, although no explanation was given. The conductivity of pure Na_2CO_3 is on the order of 10^{-5} - 10^{-4} $S.cm^{-1}$ at the temperature range from 500 °C to 580 °C [58]. This value is much lower than the values reported for the nano-composite electrolyte in the literature [55]. However, in the literature for SDC - Na_2CO_3 nano-composite, the role of the Na_2CO_3 matrix was not discussed in detail.

A synergistic effect was suggested to exist between different ionic species, which leads to enhanced ionic conductivity in the composite electrolyte and many other observed related

phenomena. To summarize, the ceria-salt two-phase composite systems have complex charged ion species. Furthermore, the effect of multiple parameters, such as the electrolyte composition, the microstructures, particle size distribution, morphology, temperature and the most importantly, the applied in-situ atmospheres, are attributed to complicated multi-ion conductivity [46]. Therefore, the ceria-carbonate composite electrolytes offered a very interesting fundamental research from material science, ionics, electrochemical FC device, technologies, and applications fields. It opens a new era with significant importance for both fundamental and applied research.

1.6.2. Phase Reaction

Previous research existing in the literature reported that powder XRD diffraction of the composite displayed negligible phase interaction. Thus, all XRD patterns of the composite were dominated by the fluorite-type DCO, whereas smaller additional peaks could be ascribed to the carbonate phases, presumably predominantly amorphous [61]. The carbonate was suggested as existing as an amorphous phase co-existing with the SDC. It is highly likely that the carbonate phase covers the SDC particles since during the heat treatment, the carbonate would have been molten [61,62]. The composite electrolyte showed only the diffraction pattern of the cubic fluorite structure, identical to the pure SDC phase. The absence of peaks belonging to the carbonate phase could be indicative of carbonate in the composite electrolyte existing as an amorphous phase, which was also observed in a previous study [63].

1.7. Objectives

So far, the developments of composite electrolyte materials for LT-SOFC applications are still at their initial stage. There are a large number of investigations on the different phases of the salts, types of ions transported, and micro structure. It appeared necessary to study these new type electrolytes for a deeper understanding of the improved ionic conduction in the two-phase composites. In this study, we aimed to design and fabricate high ionic conductor composite electrolytes for LT- SOFC (<600 °C). We have investigated the ionic conduction behavior of the ceria based composite electrolyte in the temperature range from RT to 600 °C by electro-chemical impedance spectroscopy (EIS) techniques. In order to unravel the oxide's role, we also prepared different composite materials whose oxide backbone was different than ceria.

Composite electrolyte systems have been studied in this work in 4 main sections. In the first part, the design and fabrication of a nano-composite electrolyte with a controlled total interface area (SSA) between the SDC particles and the Na_2CO_3 matrix for a fixed mass ratio of components was the topic of the research. Varying the amount of specific interface area between constituent phases in the nano-composite fuel cell electrolyte revealed insight into the role of interfaces in ionic conductivity. This objective was accomplished by taking advantage of the inverse relationship between the average particle size and specific surface area (SSA) for ceria particles of micron and nano-meter size distributions.

The second part is about the percolation properties of composite material based on SDC-Na_2CO_3 as a function of the Na_2CO_3 amount, such as 5 wt%, 10 wt%, 15 wt% and 20 wt%. For some special cases, the 50 wt% carbonate composite was also fabricated.

The third part contains electron microscopy investigation on the FIB thinned composite (SDC-Na_2CO_3 10 wt% and SDC-Na_2CO_3 15 wt%). This part is concerned with the imagining of the interface in SDC (HP)-Na_2CO_3 based nano-composite electrolyte pellets. It includes their detailed characterization using high resolution electron microscopy (HR-EM) techniques for the complimentary analysis on morphological and structural properties at the micro and nano-scale for the first time in the literature.

The forth part contains a survey of SDC-Na_2CO_3, Al_2O_3-Na_2CO_3, TiO_2-Na_2CO_3, LSGM-Na_2CO_3, MgO-Na_2CO_3 and YSZ-Na_2CO_3 with 20 wt% Na_2CO_3 based composite materials for these different oxide-backbones. The objective was to observe the effect of different oxide surfaces on the ionic conductivity of the composite.

The study is targeted on understanding the role of interfaces in the enhanced ionic conductivity of the composite electrolytes. The ionic conductivity of the composites were tuned by the varying the types of oxides embedded into Na_2CO_3 matrix in order to understand the role of oxide surface iso-electric point to the electrical properties of composites. Thus, the concentration of the Na_2CO_3 in the composite was fixed at 20 wt% in order to compare the efficiency of oxides surfaces, which were yttrium-stabilized zirconia (YSZ), $La_{0.80}Sr_{0.20}Ga_{0.80}Mg_{0.20}O_{3-x}$(LSGM), MgO, TiO_2, Al_2O_3 and SiO_2 on the ionic conductivities in the composites. The electrical conductivities of all the composites were evaluated by the electrochemical impedance analysis (EIS) at varied temperatures.

CHAPTER 2: EXPERIMENTAL PROCEDURES

2.1. Materials

In the experimental part of this study, two kinds of Samarium doped Ceria (SDC; $Sm_{0.2}Ce_{0.8}O_{1.9}$) powders with different particle sizes were used. Nano-meter sized powders, SDC ($Sm_{0.2}Ce_{0.8}O_{1.9}$) N20, and micrometer-sized powders, SDC ($Sm_{0.2}Ce_{0.8}O_{1.9}$) HP, were purchased from FUEL CELL METARIALS (Ohio, USA). SDC HP powders had particles with sizes in the range between 60 nm and 150 nm with a measured specific surface area of 11 $m^2.g^{-1}$. The SDC N20 was nano-meter sized powders with sizes in the range of 5 nm-10 nm with a measured specific surface area (SSA) of 203 $m^2.g^{-1}$. The Na_2CO_3 anhydrous powder and $NaHCO_3$ were purchased from Aldrich (Germany). AKP-500 alumina powders, with an average particle diameter of 0.21 μm were purchased from Sumitomo Chemical (Japan). 8mol% Yttria Stabilized Zirconia (YSZ) powders were purchased from Inframat Advanced Materials LLC, (Manchester, USA). LSGM powders were purchased from FUEL CELL METARIALS (Ohio, USA). Flash dry Silver paste was from SPI Supplies (West Chester, USA).

2.2. Fabrication Technique

The fabrication method used in experimental study was particularly based on dry ball milling procedure. In addition, the solution based composite processing procedure was also investigated for comparison.

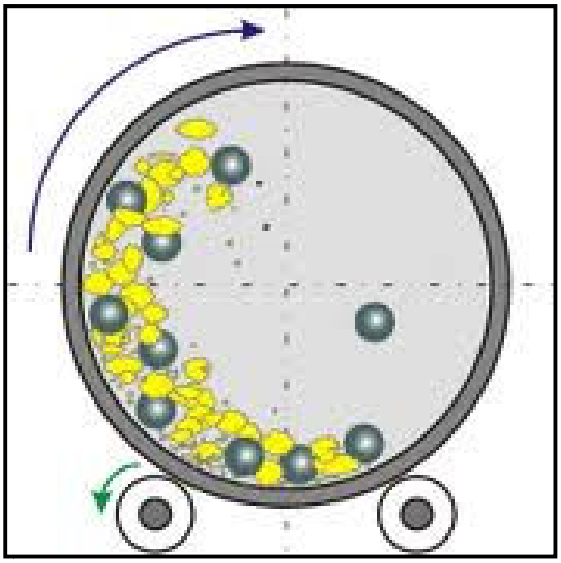

Figure 2.1. The ball milling technique [64].

A ball mill is a type of grinder used to grind materials into extremely fine powder [64]. Ball mills rotate around a horizontal axis, partially filled with the material to be ground plus the grinding medium. The ball milling process is schematically presented in Figure 2.1.

In the dry ball milling process, SDC crystalline powders were combined with Na_2CO_3 powders in the specified weight ratios to form composite mixture. The weighed stoichiometric powder mixtures were dry-milled by using 3 mm-(diameter) sized YSZ milling media for 6 hours. Then, the powders were collected and re-ground by hand in an agate mortar and pestle, before being uniaxially pressed into a pellet. Pellets made from the composite electrolyte were further subjected to isostatic compaction under 40 MPa in one step, to form a green compact with a diameter of 9 mm and a thickness of 1 mm. The pellets were heat-treated at 700 °C in air for 1 hour. The heating rate was 5 °C/min.

In the solution process, SDC (N20) crystalline powders were combined with Na_2CO_3 powders in the specified weight ratios to form a composite. The weighted powder mixtures were added to de-ionized water and stirred for 6 hours. The solution was kept in room temperature hood for 12 hours then placed in 80 °C furnace for 12 hours. Then, the powders were collected and re-ground by hand in an agate mortar and pestle before uniaxially pressing them into a pellet. Pellets made from the composite electrolyte were further subjected to isostatic compaction under 40 MPa in one step, to form a green compact with a diameter of 9 mm and a thickness of 1 mm. The pellets were heat-treated at 700 °C in air for 1 hour. The heating rate was 5 °C/min.

2.3. Production of Solid Composite SDC Na_2CO_3 Electrolyte

SDC (SDC (HP) and SDC (N20)) crystalline powders were combined with Na_2CO_3 powders in a weight ratio to form a 5 wt%, 10 wt%, 15 wt%, and 20 wt% Na_2CO_3 composites. The Table 2.1 describes the prepared samples and characterization tools. In some special cases composites with 50 wt% Na_2CO_3 were also prepared for specific investigations.

Table 2.1. The specimens and performed characterization techniques

	5wt%	10 wt%	15 wt%	20 wt%
SDC(HP)	XRD; SEM; EIS; Raman			
SDC(N20)				

The measured specific surface areas (SSA) of the SDC (N20) and SDC (HP) powders were 203 $m^2.g^{-1}$ and 11 $m^2.g^{-1}$, respectively. Micrometer-sized SDC (HP) and nano-meter sized SDC (N20) powders were mixed in the weight ratios of 4.35, 1.35, 0.92, 0.5, and 0.1 to form

oxide powder mixes with SSA of 47 $m^2.g^{-1}$, 93 $m^2.g^{-1}$, 110 $m^2.g^{-1}$, 140 $m^2.g^{-1}$ and 185 $m^2.g^{-1}$. Afterwards, all oxide powders were combined with anhydrous Na_2CO_3powder (Aldrich, Germany) to form a 10 wt% Na_2CO_3-SDC composite with specific interfacial area determined by the oxide powder SSA. The table 2.2 describes the prepared samples and characterization tools used in the investigation.

Table 2.2. The specimens and performed characterization techniques

$[SDC(N20)/SDC(HP)]_{wt}$	4.35	1.35	0.92	05	0.1
Sample name	47SSA	93SSA	110SSA	140SSA	185SSA
Performed Tests	SEM XRD EIS TEM				

Fabrication of composites SDC/$NaHCO_3$ electrolytes followed the procedure described in section 2.2. Similarly, fabrication of composites SDC/Na_2CO_3, TiO_2/Na_2CO_3, YSZ/Na_2CO_3, Al_2O_3/Na_2CO_3, LSGM/Na_2CO_3, SiO_2/Na_2CO_3, and MgO/Na_2CO_3 electrolytes followed the same procedure, as described above. Different oxide powders were combined with Na_2CO_3 powders in a weight ratio to form 20 wt% Na_2CO_3 composites. The table 2.3 describes the prepared specimens and tools used in the characterization.

Table 2.3. The specimens and performed characterization techniques

Composite	SDC/ Na_2CO_3	TiO_2/ Na_2CO_3	YSZ/ Na_2CO_3	Al_2O_3/ Na_2CO_3	LSGM/ Na_2CO_3	SiO_2/ Na_2CO_3	MgO/ Na_2CO_3
Na_2CO_3 (wt% ratio)	20 wt%	20 wt%	20 wt%	20 wt%	20 wt%	20 wt%	20 wt%
Characterization Methods	EIS, Zeta potential, SEM						

2.4. Heat Treatment

Pellets were cold compressed under 40 MPa in one step to form a pellet with a diameter of 9 mm and a thickness of 1mm. The pre-shaped pellet underwent wet-bag iso-static pressing of 40 MPa. The pellet was heat treated at 700 ^oC for 1 hour with the heating rate of 5 ^oC/min. In the wet-bag iso-static pressing, pre-shaped pellet was encased in a rubber sheath, which was immersed in a liquid which transmitted the pressure uniformly to the pellet.

2.5. Characterization Methods

In this study, complimentary characterization methods were used in order to get comprehensive structural and chemical information from the investigated materials at both micro- and nano-scale. These include:

- X-ray diffraction (XRD) for examining the crystallinity and phase distribution of the composite powders.
- Differential Thermal analysis (DTA) to determine the melting temperature of the Na_2CO_3 and to detect any possible thermal event.

- Scanning Electron Microscopy (SEM) to analyze the morphologies of the produced electrolytes at high magnifications and as a quality control tool to assure the homogeneity of the composite microstructure.
- Energy Dispersive X-ray Spectroscopy (EDX) to perform elemental analysis at the micro-scale, for obtaining chemical information.
- Focused Ion Beam (FIB) to prepare ultra-thin and uniform lamellas for further TEM analyses.
- Transmission Electron Microscopy (TEM) to obtain detailed information from the materials at nanometer scale resolution.
- Dilatometer to determine phase transition of the composite electrolytes.
- Dynamic light scattering (DLS) to measure the zeta potential of the oxides.

Detailed information on each of these characterization techniques and related experimental work will be given in the following sections of this chapter individually as follows.

2.5.1. X-Ray Diffraction (XRD)

X-ray diffraction (XRD) is an analytical technique looking at X-ray scattering from primarily crystalline materials. Each material produces a unique "fingerprint" of X-ray intensity versus scattering angle that is characteristic of its crystalline atomic structure. Qualitative analysis is possible by comparing the XRD pattern of an unknown material to a library of known patterns. This information can be fruitfully used for 3D quantitative analysis of specimens as well [65].

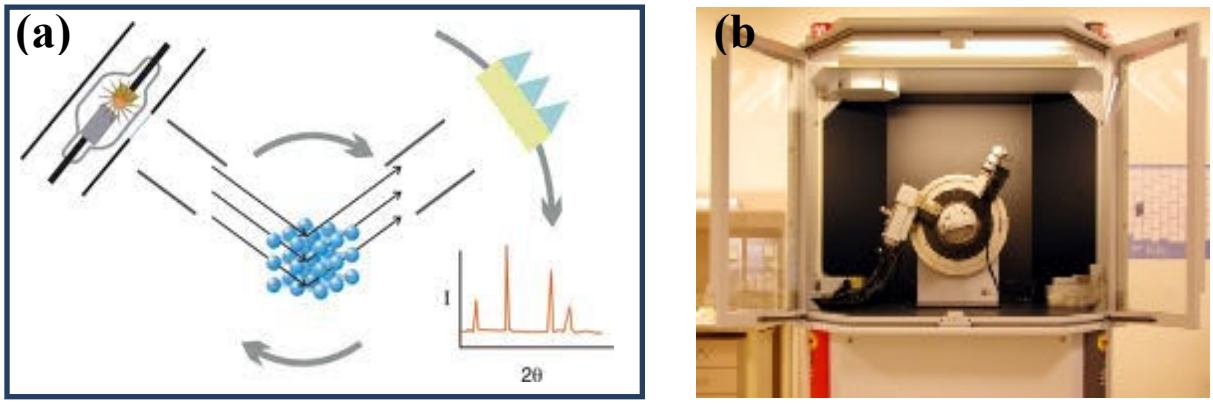

Figure 2.2. (a) The diagram showing the working principle of an XRD [65] and (b) the XRD set up at Sabanci University.

The measurements were performed at 40 kV and 40 mA, using CuKα radiation (λ=1.5418 Å). In all measurements, the step size was 0.02°, and data collection period was 1 s. in each step. $K\alpha_2$ peaks were suppressed in the X-ray diffraction measurements by a monochromator. Bragg Conditions: The two parallel incidents rays and make an angle θ with these planes. A reflected beam of maximum intensity will result if the waves represented by first and second are in phase. The difference in path length between first to first and second incidents rays must then be an integer number of wavelengths. The relationship is mathematically explained in Bragg's law [66].

$$2d \sin \theta = n \lambda \qquad \text{Equation (2.1)}$$

The process of reflection is described here in terms of incident and reflected (or diffracted) rays, each making an angle θ with a set of fixed crystal planes. A reflection occurs from planes set at angle θ with respect to the incident beam and generates a reflected beam at an angle 2θ from the incident beam. The possible d-spacing defined by the indices (*h,k,l*) are

determined by the shape of the unit cell. Therefore the possible 2θ values, where we can have reflections are determined by the unit cell dimensions. However, the intensities of the reflections are determined by the distribution of the electrons in the unit cell. The highest electron density is found around atoms. Therefore, the intensities depend on what kind of atoms we have and where in the unit cell they are sitting. Planes going through areas with high electron density will reflect strongly, planes with low electron density will give weak intensities [65].

The average crystallite size (d) can be evaluated from the peak broadening of the diffraction pattern, based on the following Scherer's Equation (2.2).

$$d = \frac{0.94\lambda}{\beta cos\theta}$$ Equation (2.2)

λ is the X-ray wavelength; β is the line broadening at the maximum intensity; θ is the Bargg angle. For phase identification, the experimental spectra were compared with the characteristic X-ray card files in the JCPDS database. The crystal structure and phase distribution of the powders were analyzed using the X-ray diffractometer at Sabanci University (Bruker AXS-D8, Karlsruhe, Germany).

2.5.2. Differential Thermal Analysis (DTA)

Differential Thermal Analysis (DTA) is a thermo-analytic technique. In DTA, the material under study and an inert reference are exposed to identical thermal cycles, while recording any temperature difference between the sample and reference. Changes in the sample, either

exothermic or endothermic, can be detected relative to the inert reference. Thus, a DTA curve provides data on the transformations that have occurred, such as glass transitions, crystallization, melting and sublimation [66]. The area under a DTA peak corresponds to the enthalpy change that is not affected by the heat capacity of the sample. Thermal properties of the composites were studied using differential thermal analysis (Netzsch STA 449C Jupiter, Selb, Germany). All samples placed inside a pure alumina crucible were heated up to 1000 °C in the furnace of the DTA with a heating rate of 5 °C/min.

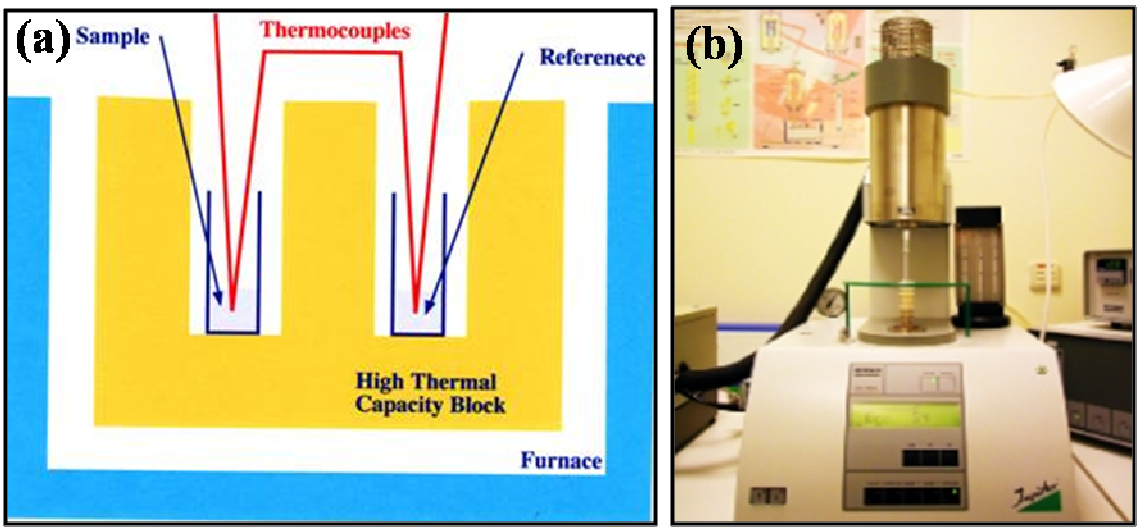

Figure 2.3.(a) Working principle diagram of DTA [66] and (b) the photo image of the DTA.

2.5.3. Scanning Electron Microscopy and Energy Dispersive X-ray Spectroscopy

The scanning electron microscope (SEM) is a type of electron microscope that images the sample surface by scanning it with a high-energy beam of electrons. Unlike TEM, SEM can image and analyze bulk specimens [67]. If the specimen is very thin, then electrons may be

transmitted through it unabsorbed and used to form the image in TEM. If the specimen is thicker, then electrons are no longer transmitted so only particles (e.g. electrons, x-rays and photons) emerging from the surface can give us information. These are the signals used in a conventional SEM [67]. SEM can provide information on surface topography, crystalline structure, chemical composition and electrical behavior of the top 1 μm of the specimen.

Usually, the spatial resolution of the SEM depends on the electron spot size, which in turn depends on both the wavelength of the electrons and the electron-optical system which produces the scanning beam. The resolution is also limited by the size of the interaction volume, or the extent to which the material interacts with the electron beam [65,67]. When the primary electron beam interacts with the sample, the electrons will lose energy through repeated scattering and absorption within a teardrop-shaped volume of the specimen (also known as the interaction volume) which extends from less than 100 nm to around 5 μm into the surface. The size of the interaction volume depends on the electron energy, the atomic number (Z) and density of the specimen. The energy exchange between the electron beam and the sample, results in the reflection of high-energy electrons by elastic scattering, emission of secondary electrons by inelastic scattering and the emission of electromagnetic radiation. Various signals from the specimen can be collected and used to form images (Figure 2.4), as follows: Secondary electron (SE), backscattered electron (BSE) images, and X-rays [67].

Secondary electron images are those formed by signals from electrons that have escaped from the specimen with energies below 50 eV. These provide the highest spatial resolution images, as they can only escape from a very shallow (around 100 angstroms), near-surface layer of material and the signal comes from an area about the size of the electron probe. Primarily,

they give topographic information. Since a few BSE are collected by the secondary electron detector, compositional contrast is also presented by backscattered electrons.

BSE are those incident electrons that approach the nucleus of an atom sufficiently close to be scattered through a large angle and re-emerge from the surface. Their number is less than secondary electrons, but they have much higher energies. Images have slightly less resolution than secondary electron images, because they come from slightly deeper in the specimen. Thus, the area giving rise to the signal is larger than the probe size. Mostly, they provide compositional information: elements of higher atomic mass give brighter contrast. BSE can also provide crystallographic information, as electron channeling occurs [66,67].

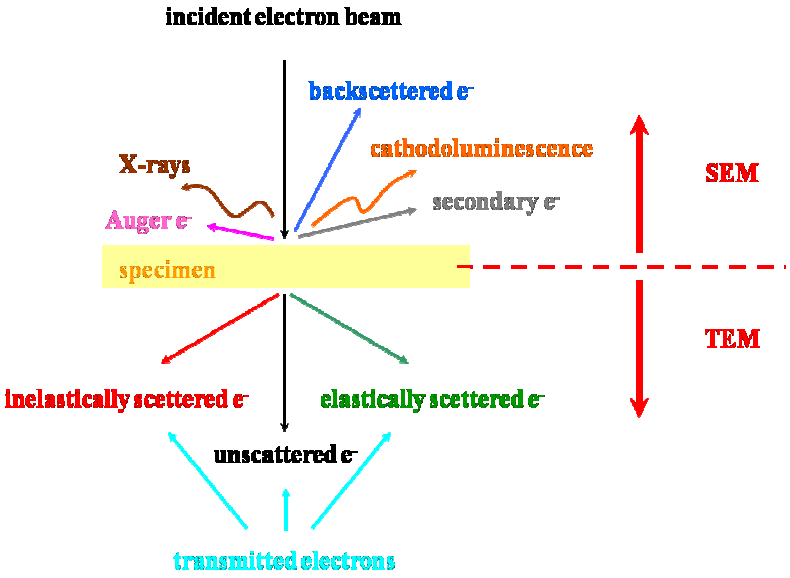

Figure 2.4. Signal generation due to specimen-electron beam interaction [67].

In an SEM, magnification results from the ratio of the dimensions of the raster on the specimen and the raster on the display device. Magnification is controlled by the current supplied to the x-y scanning coils and not by objective lens power [66]. For the

microstructure observation, such as the morphology and size distribution, scanning electron microscopy (FEG-SEM Leo Supra 35, Oberkochen, Germany) was employed. Energy dispersive X-ray spectrometry (EDS, Röntec, Germany) was used for elemental analyses. The observations of the cross-sections including pore size, the distribution of two phases, and the dense structure of electrolyte were examined by using SEM. Elemental mapping of the SEM images, point and line analyses for the specified regions on the samples were acquired by using EDX. Density of sintered pellet was measured from images taken from the polished surfaces with the help of a SEM.

2.5.4. Transmission Electron Microscopy (TEM) and Focus Ion Beam (FIB)

2.5.4.1. TEM

TEM is the technique where the transmission of a beam of electrons through an ultra-thin specimen induces electron-specimen interactions. An image is formed from the electrons transmitted through the specimen, magnified and focused by an objective and consecutive lenses [66, 67]. TEM give information about the microstructure, crystal quality and defect concentrations in a layer. Crystal symmetry and lattice parameter data can be obtained from diffraction patterns, and the composition of the specimen can be obtained from techniques such as energy dispersive X-ray analysis and Electron Energy Loss Spectroscopy (EELS) [67].

In multilayer specimens, TEM can give information about the thickness of each layer, its composition and the quality of the interface between the layers. However, information which

is obtained only from a small area may not be representative all the times. Therefore, other analytical techniques like XRD and (surface) EELS are often used to complement TEM [67].

Figure 2.5. The JEOL ARM 200 CFEG system equipped with EDS and EELS from Gatan at SUNUM.

2.5.4.2. FIB and FIB Sample Preparation

Focused ion beam (FIB) is a technique used in the materials science fields for milling, micromachining, and manipulation and TEM sample preparation of materials [68]. FIB instrument is very similar to a SEM, except that the beam scanned over the sample is an ion beam rather than an electron beam [68].

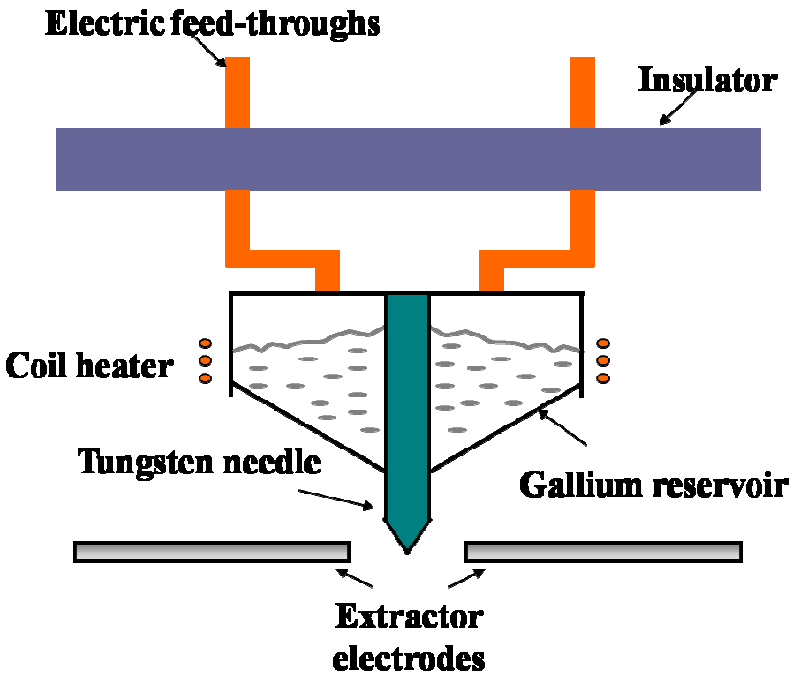

Figure 2.6. A commercial LMIS with Ga reservoir used at the FIB [68].

The basic single-beam FIB instrument consists of a vacuum system and a chamber, a liquid metal ion source, an ion column, a sample stage, detectors, gas delivery system and a computer to run the complete instrument, as shown in Figure 2.6 [68]. The liquid metal ion source (LMIS) will generate focused beam of metal ions. A typical LMIS contains a tungsten (W) needle attached to a reservoir that holds the metal source material. Gallium is commonly preferred in commercial FIB instruments.

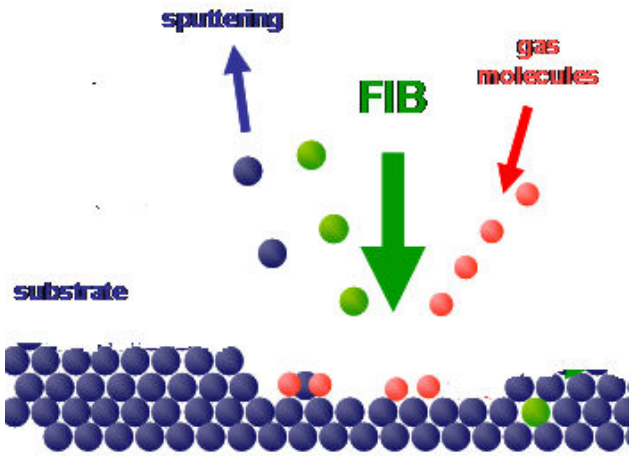

Figure 2.7. The schematic of the FIB working principle.

In this dissertation FIB was particularly focused on the preparation of TEM specimen for the materials that have interface micro-structure. Also “slice and view” process, which allows sequential cross-sectioning by ion milling and in-situ electron beam imaging simultaneously, is also available by dual-beam instruments. By this means, while the sample in the TEM provides 3D information at the nano-meter scale and below; via FIB cross-sectioning, the information in the scale ranging from micrometers to tens of nano-meters is collected from the identical sample. The main approach in special TEM sample designs is to overcome the sample preparation limitations. This is also supportive in the direction of improving the quality of the production and the final composite.

For the preparation of electron transparent and uniform samples for TEM analysis of SDC-Na_2CO_3 structures, a Carl-Zeiss Cobra FIB/HR-SEM platform was used. Cross sectioning of specimens was performed by *in-situ* lift-out technique. The entire sample was gold-plated (10 nm around) beforehand via metal sputtering prior to FIB-SEM analysis and nano-structuring. To prevent gallium implantation, two individual (EBID and IBAD) local protective layers of platinum with circular geometries (4-5 μm) were deposited on top of the region of interest on

the sample as a starting point in the TEM specimen preparation. For the initial step, two protective platinum layers were deposited on top of the interested region before trenching, to prevent gallium implantation. The first layer was applied by electron beam assisted deposition of platinum which provided a film thickness of about 500 nm. Second layer was applied on top of the former, giving a layer thickness of approximately 2 μm In order to form the two sides of the region of interest; ion milling was applied at 30 keV with relatively high ion currents. After trenching, consequent milling was performed using rather low ion currents (3 n Å to 1 n Å), approaching from both sides until a 1-2 μm thick cross-section was formed. In this step of milling, a small angle tilting (± 2-3 °) was used to maintain a wedge shape on the section, which helps to remove the bottom part from the bulk material. Then, the bottom and the side trenches were cut away using 1 n Å until the section is hold by the bulk sample from its shoulders. For the lift-out step, the micromanipulator was inserted and glued to the section, using an ion beam assisted platinum connection. This was followed by cutting the shoulders away and leaving the sample free to move by the manipulator for transportation.

The free section was then mounted on a TEM grid using platinum deposition again, and the sample was thinned by ion milling using currents (from 1 n Å down to 0.1 n Å) until a thin lamella (below 100 nm) was formed. As the final stage, the sample was polished at 5 keV ion energy and p Å-range ion current for the removal of gallium, which might have been implanted on the specimen surface during the milling process. In order to obtain a pin-form TEM sample finally, the milling process was performed using annular patterns until a pillar on the original sample matrix was formed. This was followed by transferring the pillar (a few micrometers in diameter) to a TEM semi-grid using a micromanipulator, which is also called the in-situ lift-out technique. The pillar on the sample was then subjected to further fine ion-

milling process in order to form a very thin and sharp tip on the edge to be used as a uniform TEM sample.

2.5.5. Electron Energy Loss Spectroscopy (EELS)

Many of the electrons, which have passed through a thin sample in a transmission electron microscope, will undergo inelastic scattering and their energy loss provides information about the chemical and structural properties of the specimen. The amount of energy loss can be measured via an electron spectrometer and interpreted in terms of what caused the energy loss [68].

The excited states decay by emitting the transferred energy in the form of an X-ray, a visible photon Auger electron, heat, etc in Figure 2.8. EELS is the most important among all spectroscopes, since it probes the primary excitation (i.e. absorption) and therefore registers each excitation event independently of the exact de-excitation mechanism. Electron energy loss spectroscopy of inner shell losses therefore provides a convenient method of identifying atoms in different types of structural environments [69].

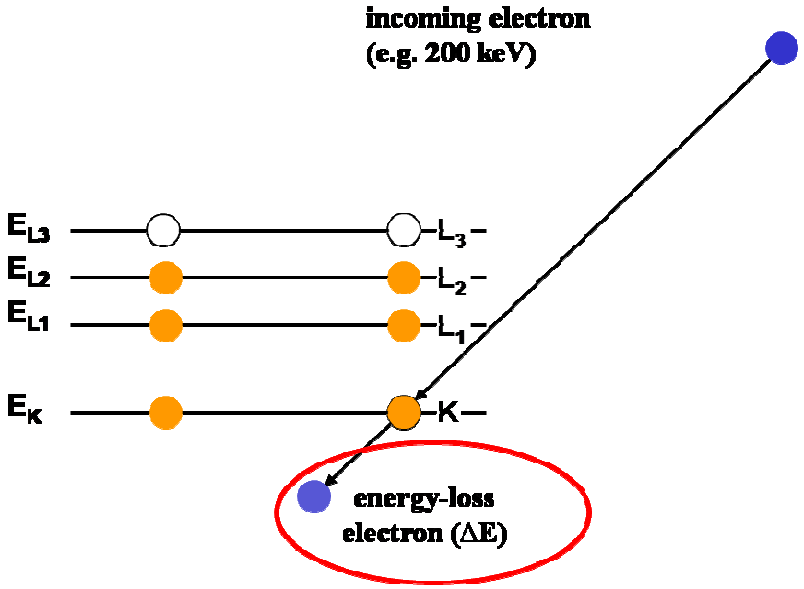

Figure 2.8. The formation of energy loss [69].

EELs spectra can be recorded over the entire energy range of valence and core electronic excitations, with a very high spatial resolution (down to 0.1 nm probe size). This can be useful to solve problems particularly in the field of interface analysis.

TEM is widely used to investigate a sample's morphology, including the size and shape. In addition, it also can provide crystallographic information such as the arrangement of atoms in the specimen and their degree of order. In this study we have employed several TEMs and FIBS such as, TEM (JEM-ARM200F with Cold Field Emission Gun, at Sabanci University), a JEM-2100F (TEM, JEOL, Japan), and TEM (FEI Helios 600 NanoLab Platform FIB) at Jozef Stefan Institute, Slovenia. The powder and thinned pellet specimens were loaded onto carbon-coated copper grid and special indexed FIB/TEM grids.

2.5.6. Dilatometer

A dilatometer is a thermo-mechanical analytical tool used for obtaining highly precise measurements of volume changes in solids, powders and pastes. The change depends upon the temperature variation, chemical reactions, absorption of fluids, and physical stress, *i.e.,* pressure on a solid substance. To examine the phase transitions, chemical reactions (oxidation) and solid-state reaction, the dilatometer is very useful [65]. Thermal expansion behaviors of the composite constituents were analyzed in the temperature range of RT to 1000 °C with a heating rate of 5 °C/min. With a pushrod type dilatometer (DIL 402 PC push rod, Netzsch, Selb, Germany).

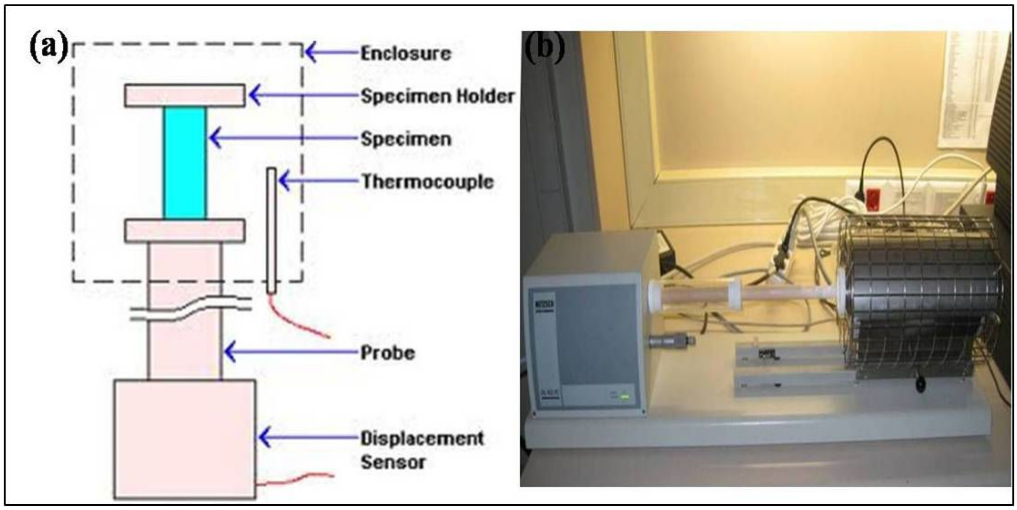

Figure 2.9. (a) Diagram of the dilatometer [65] and (b) the photo image of the Dilatometer.

2.5.7. BET- Surface Area Analyses

"Brunauer-Emmit-Teller (BET)" theory describes a well-known phenomenon for the physical adsorption of gas molecules on a solid surface. The BET method is widely used to determine the effective surface areas of the solid materials with complicated shapes, such as porous

powders, by physical adsorption of gas molecules [66]. The observation of the so-called adsorption and adsorption isotherms is used to determine the amount of gas molecules adsorbed to a surface. A total surface area S_{total} and a specific area S_{BET} are evaluated by the following Equation (2.4):

$$D_{BET}=\frac{6\times10^3}{\delta_{th}S_{BET}} \qquad \text{Equation (2.4)}$$

δ_{th} is skeletal density, which is the mass of the solid divided by the volume of the solid excluding open and closed pores. D_{BET} is the particle diameter [66]. Surface area of the powder mixtures used in this study were determined using the BET method from the low temperature adsorption of nitrogen, performed at -196 °C after degassing at 350 °C for 3 hours.

2.5.8. Raman Spectroscopy

Raman Spectroscopy is a vibration spectroscopy technique used to obtain information on chemical structures and physical forms. The Raman spectroscopy measurements were performed to identify the substance with characteristic spectral patterns. Infrared absorption is much more widely used than Raman spectroscopy, largely due to the limitation of the sample degradation and fluorescence [70].

Since Raman is a form of vibrational spectroscopy, energy transitions arise from molecular vibrations. Because these vibrations involve identifiable functional groups, they can be used to identify the molecule, if the energies of these transitions are plotted as a spectrum. The

working principle of the Raman was shown in Figure 2.10. The tables for the characteristic Raman vibrational frequencies of organic groups can be found in the instrumental books [71]. In a Raman instrument, a laser is used to excite the spectra because it gives a coherent beam of monochromatic light. This provides sufficient intensity to produce a useful amount of Raman scatter and allows for clean spectra. Lasers for Raman spectroscopy must exhibit good wavelength stability and low background emission to perform accurately.

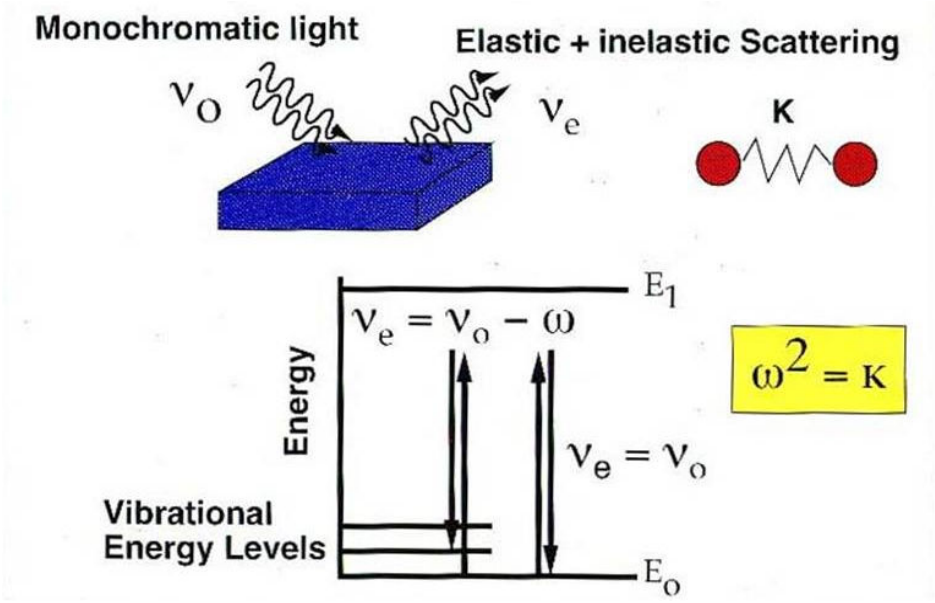

Figure 2.10. The working principle diagram of the Raman spectroscopy [70].

A Raman spectrum is a plot of the intensity of Raman scattered radiation as a function of its frequency shift from the incident radiation [71]. Usually given in units of wave-numbers, (cm^{-1}), the Raman shift is independent of the frequency of the incident radiation. Although different energy ranges are possible, the most common information is in the range of 3600-200 cm^{-1} for Raman spectroscopy. The structural characterization was carried out by Raman

spectroscopy measurements (Renishaw Raman microscope system 3000) using a 25 mW He–Ne laser with 532 nm excitation wavelength.

2.5.9. Electrochemical Impedance Spectroscopy (EIS)

Electrochemical impedance spectroscope is a technique to probe the electrical properties of a dielectric substance as a function of frequency of the applied voltage. Depending on the investigated property the frequency range can cover several orders of magnitude. When sinusoidal and low amplitude of voltage is applied to a solid electrolyte cell, EIS can be used to measure the AC current. Also for a linear system, the magnitude of the response is directly related to the electrical stimulus for any given frequency. Hence, in a linear system, the applied potential, E(t) is given by Equation (2.5):

$$E(t) = E_0 \exp(j\omega t) \qquad \text{Equation (2.5)}$$

E(t) is the potential at time t_r E_o is the amplitude of the signal, and ω is the radial frequency. The relationship between radial frequency ω (expressed in radians/second) and frequency f (expressed in Hertz (1/sec). The current output of the system is also sinusoidal and has the same angular frequency ω, but differences in amplitude and phase from the voltage signal may occur depending on resistivity and polarizabilities present in the system. These can be represented by an equivalent circuit containing inductive, capacitive, and resistive elements, and are related as shown in Equation (2.6):

$$I(t) = I_0 \exp(j\omega t + \varphi) \qquad \text{Equation (2.6)}$$

Where φ is the phase angle, E_0 is the amplitude of the voltage and I_0 is the amplitude of the current signal. For a pure resistor, the phase shift is zero. Since Ohm's law is valid in the time or frequency domain, the impedance of a circuit consisting of resistors, capacitors and/or inductors is the ratio of the voltage applied divided by the current flowing through the circuit [71]. The impedance of the circuit Z(ω) at any frequency ω, can be represented in both polar and Cartesian form and has both the magnitude Z and the phase angle (φ).

$$Z(\omega) = \frac{E(t)}{I(t)} = zexp(-j\omega) = Z\cos\varphi - jZ\sin\varphi \; = Z' \; - Z'' \qquad \text{Equation (2.7)}$$

where j is a complex number with value of $\sqrt{-1}$, z′ and z″ are real and imaginary parts of the impedance, respectively.

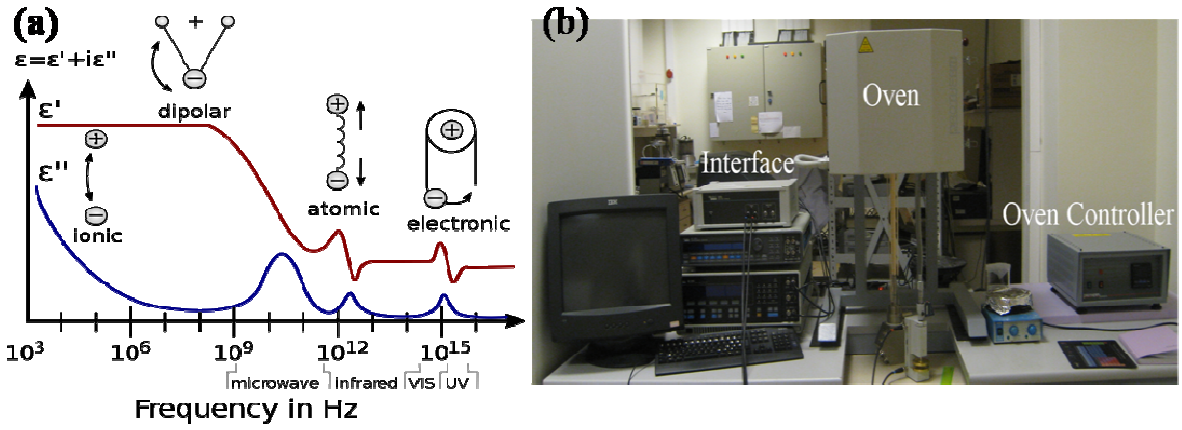

Figure 2.11. (a) A dielectric permittivity spectrum over a wide range of frequencies [71] and (b) The photo image of the electrochemical impedance analyzer.

The real and imaginary parts of permittivity are shown in Figure 2.11, and the various polarization mechanisms are summarized: ionic, dipolar relaxation, atomic and electronic resonances at higher energies.

The methods for studying diffusion of charge in solids can be subdivided into macroscopic methods and microscopic methods [71]. The macroscopic methods are sensitive to long-range diffusion. For instance, the dc conductivity measurements and mechanical relaxation spectroscopy can test this. Microscopic methods give access to microscopic diffusion parameters like hopping rates of atoms or ions and the barrier heights for the jump processes.

With the help of Cole-Cole plot, the behaviors of dielectrics where real and imaginary components of the dielectric constant of a material can be distinguished are measured over a range of frequencies. The Cole–Cole plots represent a loss dielectric in the form of a semicircle intercepting the real axis at two critical values. The dispersion of dielectric constant with frequency arises from a phase-difference between the dielectric displacement vector, **D**, and the field vector, **E**, causing the displacement of the electric polarization, **P**. The phase-difference may be initiated from three possible factors: (a) electric resistivity, leading to a response component in-phase with **E**; (b) relaxation effects in permanent dipole orientation in the dielectric medium associated with the dipole polarization component of **P**; and (c) high-frequency resonance effects arising from electronic and atomic polarization. Polarization at the electrode happens when potential of an electrode is forced away from it's value at open circuit. When an electrode is polarized, it can cause current to flow via electrochemical reactions that occur at the electrode surface [71].

A flash-dry silver paste (SPI Supplies, West Chester, USA) was used on both surfaces of the electrolyte pellet as contact electrodes covering the full top and bottom surfaces of the pellets. The complex resistivity of the pellets was measured by using a two-probe AC impedance

spectrometer with an electrochemical interface (Solartron 1260 and 1286, respectively, Farnborough, UK) with an applied bias (AC) voltage amplitude of 100 mV. Electrochemical Impedance spectra (EIS) were recorded in the frequency range of 0.01 Hz to 10 MHz from room temperature (RT) to 600 °C with a ProboStat™ cell (NorECs, Oslo, Norway) under an air atmosphere. Temperature dependence of the resistivity was evaluated by comparing Nyquist plots. The conductivity values reported in the Arrhenius plots were derived from the intercepts of the semicircle in the complex impedance-plane plots with the real axis. The following Equation (2.8) was used for the conductance calculations.

$$\sigma = \frac{L}{RA} \qquad \text{Equation (2.8)}$$

R is the electrical resistance of a uniform specimen of the material (measured in ohms, Ω), ℓ is the length of the piece of material (measured in meters, m*)*, A is the cross-sectional area of the specimen (measured in square meters, m^2). A parallel RC equivalent circuit was fitted to high frequency and low frequency data with the Z-View program [71]. The total area of the silver electrodes was used in the conductivity calculations. High frequency resistance and high frequency capacitance were obtained from the fitted first semicircle, as described in the relevant literature [71]. Similarly, the low frequency data were obtained by employing same procedure. The relaxation times (τ) were also calculated by using the relationship, $\tau = CR$, where C is the capacitance, R is the resistivity [71]. The Nyquist plot is shown as real part of the complex resistance (Z') versus imaginary resistance ($-Z''$). The semi-circular arcs of Nyquist plots are generally interpreted as dipole relaxations in the system analyzed. Thus, each distinct dipole relaxation would occur with a distinct frequency and the impedance responses of the bulk, the grain boundary and the electrode decrease with frequency. Usually, solid ionic conductors require higher frequencies to measure the time constant associated

with ionic motion (milli- to microseconds) [71]. The silver electrode polarization effect appears at the very low frequency end of the spectra. The typical electrode polarization was also reported in the literature.

2.5.10. Iso-Electric Point Measurement

Zeta potential is an indicative measure of the stability of the oxide dispersion. The surface chemistry of the solid particles influences the zeta potential of any dispersion. It is possible to modify surface chemistry by altering the pH of the oxide surface. Hence, it is important to determine the relationship between pH and the zeta potential of the oxide dispersion.

Oxide surface's iso-electric point is defined by the pH values, where the zeta potential is zero. In general colloid chemistry principles, an electro-statically stabilized dispersion system loses its stability when the zeta potential magnitude or absolute value decreases to less than approximately 30 mV. Consequently, there will be some region where the system is not stable. Obviously, meta-stability will occur near the condition of zero zeta potential. Within this unstable region the particles may agglomerate, thus increasing the apparent particle size.

Oxide surface acidity is one of the determining factors for surface anion adsorption in soggy sand model [35, 36]. The enhancement in composite conductivity is attributed to increased free Li^+ ion concentration resulting from anion adsorption on the oxides surfaces [35]. Hence, it is important to determine the iso-electric points of the various oxides which can be used for the composite electrolyte. Determining the pH conditions of the specimen where the zeta potential becomes zero is a common use for zeta potential analyzer. Iso-electric points of the different oxides are varying and it depends also on the purity of the oxides. As seen from the

Figure 3.20 the suspension at iso-electric point will have a phase separation and clear aqueous solution will be formed. We employed the Malvern zeta potential (zeta sizer Nano) to measure the iso-electric points by auto pH titration.

Oxides such as Al_2O_3, SiO_2, TiO_2, LSGM, and YSZ have been analyzed alongside SDC. All of those oxide powders were used as candidate alternatives to SDC in composite electrolytes. All oxide powders were separately dispersed in 50 ml DI-water. In this study, 2 experimental conditions were employed, such as, auto titration by Malvern and manual titration by reference pH solution. The manual titration experiment was performed by using a standard pH 4 solution and standard NH_3OH solutions of pH 10, and following the sequence:

1. Prepare the base sample to be titrated
    a. Added100 ml of DI-water into a beaker.
    b. Added 0.5 g of sample to the water.
    c. Agitated in sonicator for 5 minutes.
2. The titration was performed manually following this procedure:
    a. Extracted a 50mL of the base sample using a disposable pipette into a glass beaker.
    b. Added a few drops of acid to reduce the pH or base to raise the pH to reach the desired pH.
    c. Observe that at certain points the suspension will form small agglomeration and suspensions became clear.
    d. The pH was recorded by utilizing a pH-meter (EUTechDUAL model 550). A pH value measured three times and reported the average pH value.

CHAPTER 3: RESULTS

3.1. Composite Electrolyte Design

The effects of the each constituent phase on the electrical property and density of the composite, and key factors to tailor the optimum composite, were elucidated by investigating crystal structures and thermal and electrical properties by XRD, DTA, electrochemical impedance analysis (EIS) and SEM.

3.1.1. Na_2CO_3 Constituent Phase

Figure 3.1 displays the XRD spectra of as-received and heat treated (at 700 °C for 1 hour) Na_2CO_3 powders. There were 7 obvious peaks in the XRD spectrum of the Na_2CO_3 which were located at the 2θ equal to 30°, 33°, 34.2°, 34.7°, 35.42°, 38.22° and 40.12°. As-received powders revealed peaks belonging to the (hydrated) sodium carbonate monohydrate ($NaHCO_3.H_2O$) phase beside the diffraction peaks of Na_2CO_3. Powders heat-treated at 700 °C for 1 hour demonstrated only peaks belonging to sodium carbonate (Na_2CO_3). Sodium carbonate is known to be strongly hydroscopic. Unless special precautions are taken it absorbs water vapor readily and forms $NaHCO_3.H_2O$ phase. In Figure 3.1 the extra peaks belonging to monohydrate ($NaHCO_3.H_2O$) were detected at the 2 θ of 32°, 34° and 36°. The performed preliminary Ritveld analysis shows that the commercial carbonate powders consist of the following phases: 5.6 wt% Na_2CO_3, 58.9 wt% $Na_2CO_3.NaHCO_3.H_2O$ and 35.3 wt% $Na_2CO_3.H_2O$.

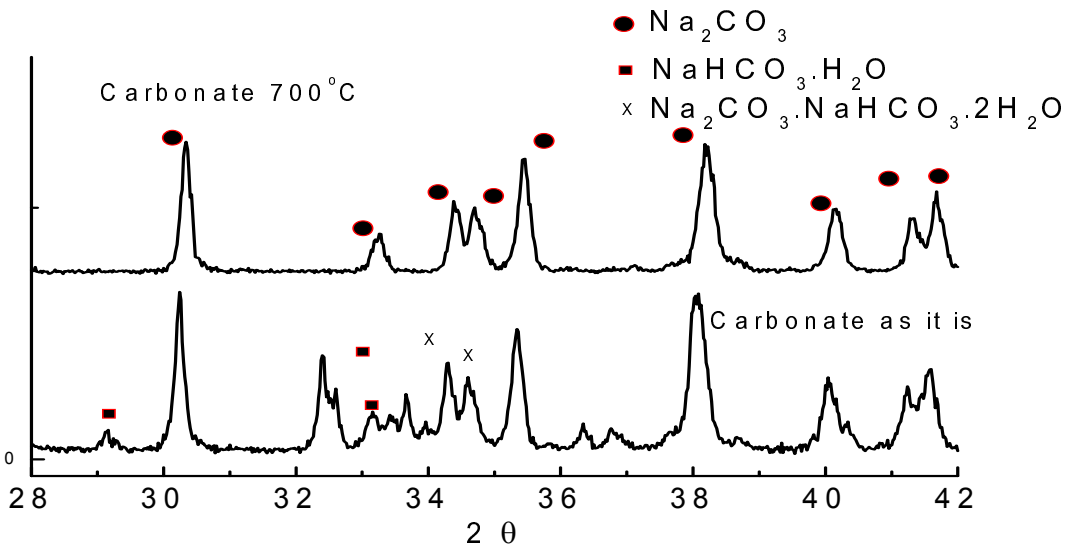

Figure 3.1. Room temperature XRD patterns of Na_2CO_3, as received and after heat-treated at 700 °C. (The $NaHCO_3.H_2O$ peaks were represented by solid squares; The $Na_2CO_3.NaHCO_3.H_2O$ peaks were represented by cross; Na_2CO_3 peaks were represented by stars.)

Surface morphology of as received Na_2CO_3 powder is presented in Figure 3.2 (a). The as-received Na_2CO_3 powders, which most likely reacted with the atmospheric moisture, revealed two phases with different morphologies with significantly different crystal sizes. The SEM image in Figure 3.2 (b) shows the surface morphology of Na_2CO_3 powder heat-treated at 700 °C. The heat-treated Na_2CO_3 morphology also revealed that heat-treated Na_2CO_3 was crystalline. Grain boundaries between large grains of the Na_2CO_3 were visible.

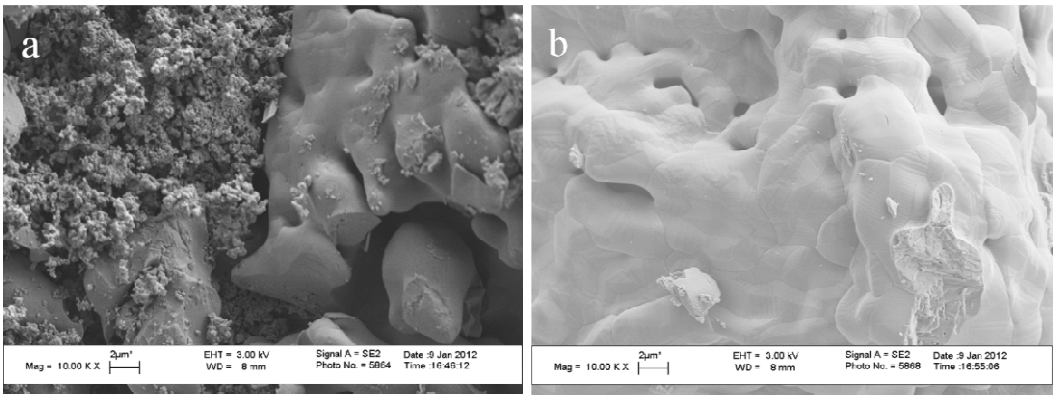

Figure 3.2. SEM images of the Na_2CO_3 as received powder (a) SEM images of the Na_2CO_3 powder after heat-treated at 700 °C (b).

The FTIR spectra of as-received or heat-treated Na_2CO_3 powders were obtained for determining the IR-signature of the Na_2CO_3 in Figure 3.3. The characteristic frequencies could be distinguished at 700, 705, 855, 878, 1440, 1755, 2500, 2620, and 3000 cm^{-1}. In addition, The CO_3^{2-} symmetric stretching bands were observed at the wave-numbers 1312, 1438, 1534, and 1585 cm^{-1}.

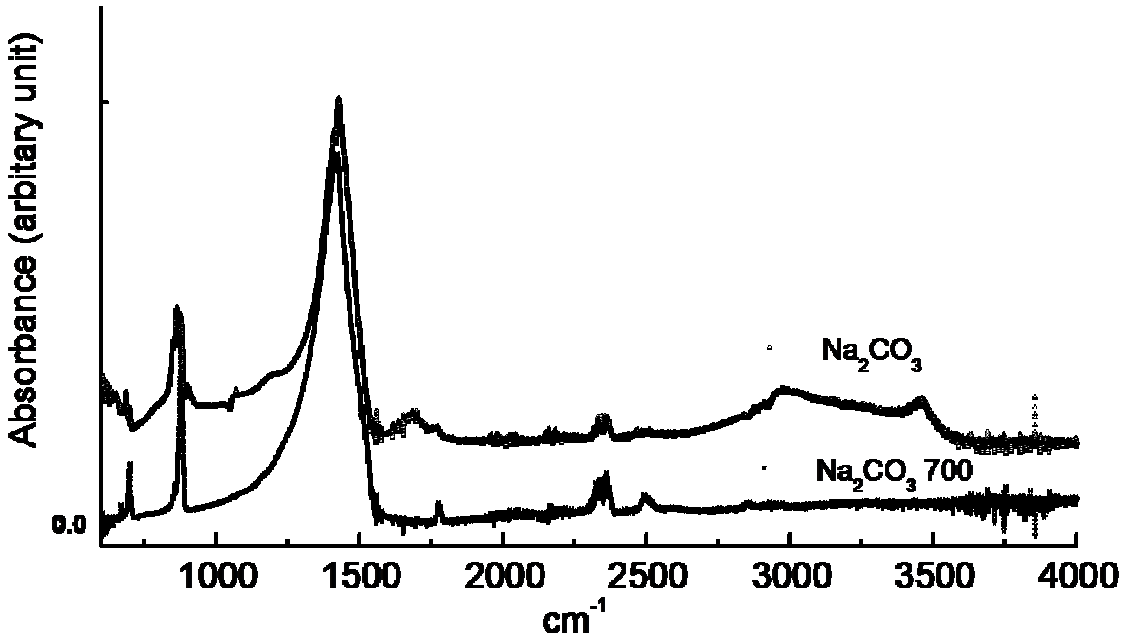

Figure 3.3. FTIR patterns of as-received and after heat-treated Na_2CO_3.

Surface morphology of dried powder of Na_2CO_3 after being dissolved in water is presented in Figure 3.4. The dried powder of Na_2CO_3 after the dissolution in water revealed two different morphologies with significantly different crystal sizes.

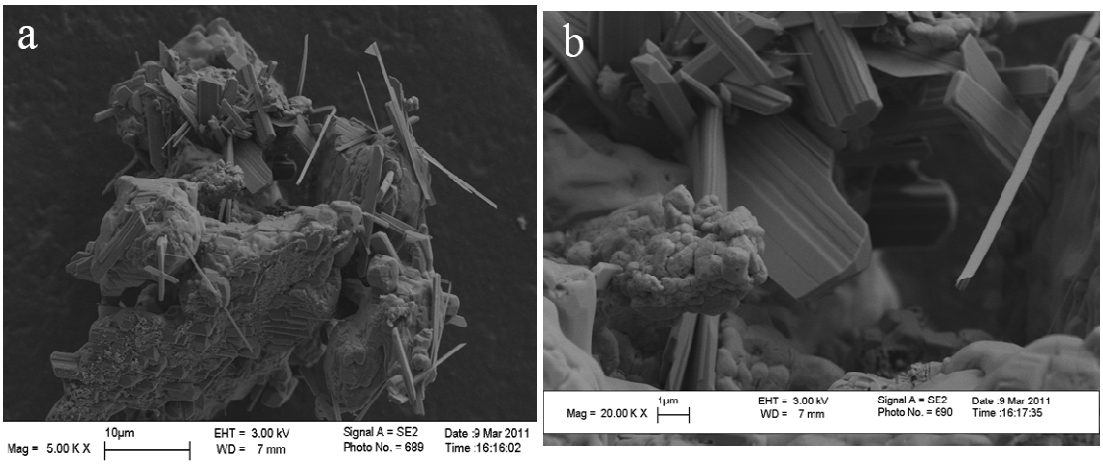

Figure 3.4. SEM images of the (a) dried powder of as received Na_2CO_3 dissolve in water and (b) at 20K magnification SEM image.

The SEM image in Figure 3.4 (b) shows the magnified surface morphology. The long stick like and more irregular rectangular shaped particles were observed. Both morphologies were sensitive electron irradiation and decomposed under long exposures to e-beam in the SEM

3.1.2. SDC Phase

The nano-meter-sized powder (referred to as SDC (N20)), had a particle size distribution from 5 to 10 nm in Figure 3.5 (a). The measured specific surface area (SSA) of SDC (N20) powder was of 203 $m^2.g^{-1}$. The micrometer-sized powder (referred to as SDC (HP)), had a particle size distribution from 60 nm to 150 nm in Figure 3.5 (b). SDC (HP) powders consisted of hard agglomerates made up of primary crystallites with 5 to 10 nm sizes. The measured specific surface area (SSA) of SDC HP powder was of 11 $m^2.g^{-1}$.

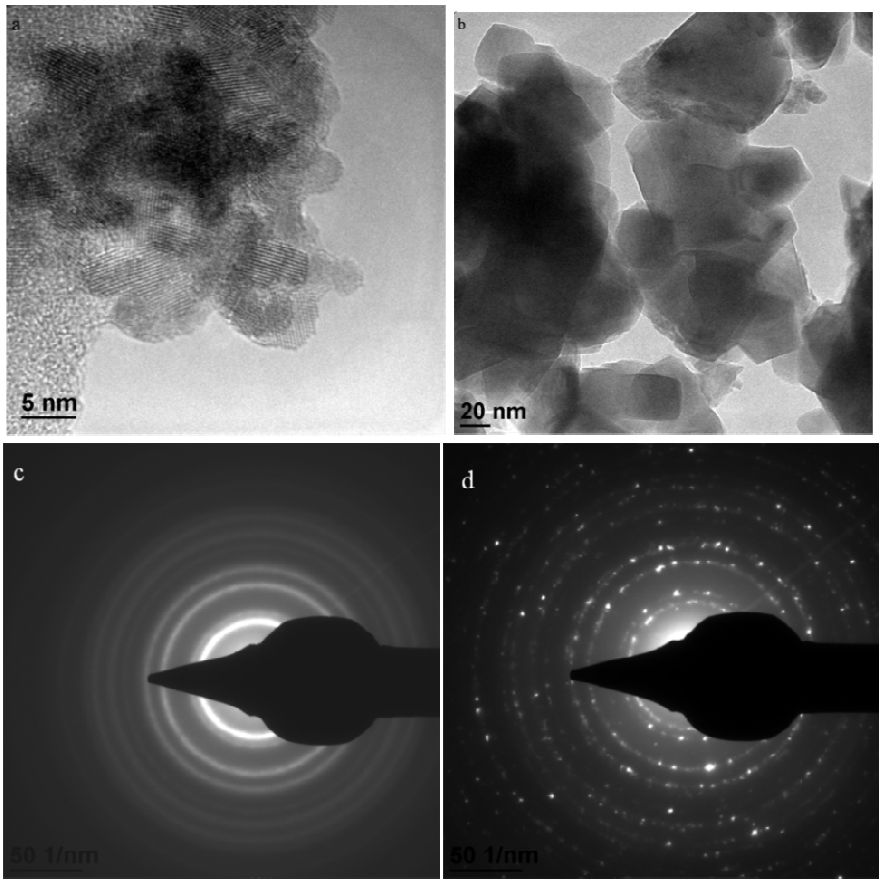

Figure 3.5. TEM patterns of (a) the SDC (N20) and (b) SDC (HP); Electron diffraction patterns of (c) SDC (N20) and (d) SDC (HP).

For comparative crystal structural studies, the XRD patterns were obtained from as-received nano-meter sized SDC (N20) powders and micrometer sized SDC (HP) powders. The XRD patterns of SDC (N20) and SDC (HP) are shown in Figure 3.6. Both sets of diffraction peaks appearing in XRD spectra were belonging to the same crystal phase. Each peak was labeled with the (*h,k,l*) index of the planes giving rise to the diffracted signals, i.e. (110), (200), (220), (311), (222), (400), (331) and (420). XRD spectra for the SDC (N20) revealed broad peaks, while SDC (HP) micrometer sized powder had sharp peaks. The crystallite sizes were calculated using the Scherer equation. The highest intensity peak was chosen to calculate the

crystallite size at 2θ of 29°. The calculated crystallite size of SDC (HP) and SDC (N20) are 20.7 nm and 3.6 nm, respectively.

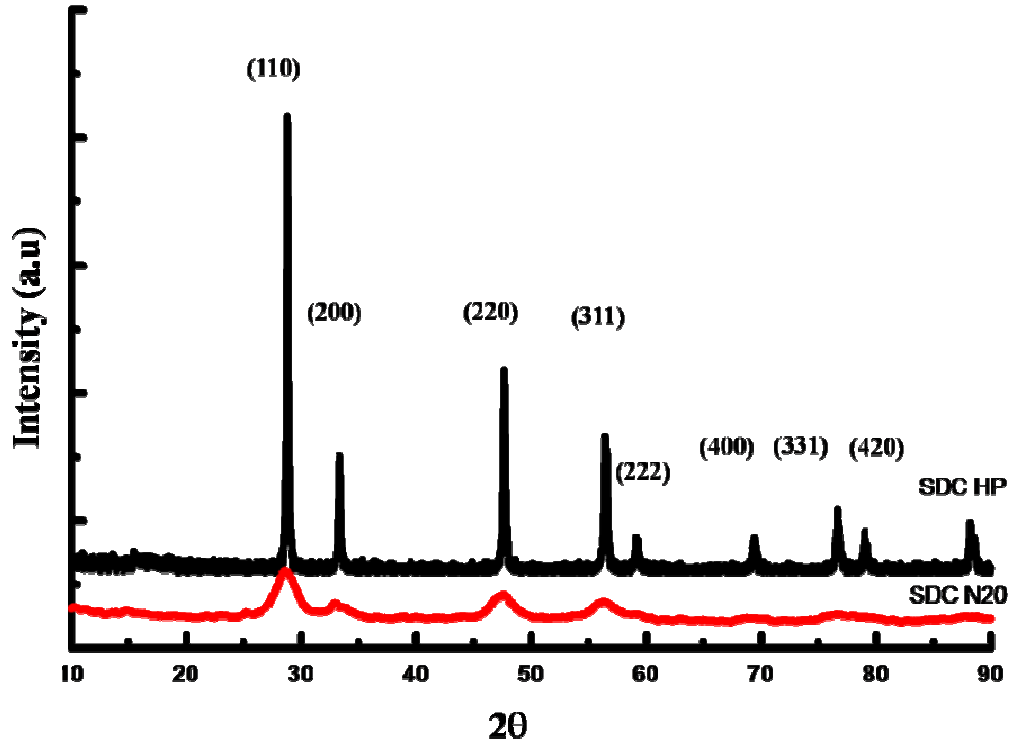

Figure 3.6. XRD patterns of the SDC (HP and N20) with labeled diffraction indexes.

Surface morphology of the SDC (N20) pellet heat-treated at 700 °C for 1 hour is presented in Figure 3.7 (a). From the observations of the SDC (N20) pellet surface, the presence of pores indicated that the pellet had not reached full density. The SEM micrograph in Figure 3.7 (b) illustrates the surface morphology of an SDC (N20) pellet heat-treated at 1100 °C for 8 hours. When compared to the microstructure shown in Figure 3.7 (a), the density of the pellet (b) was strongly improved. During the heat treatment the grain sizes reached about 100 nm.

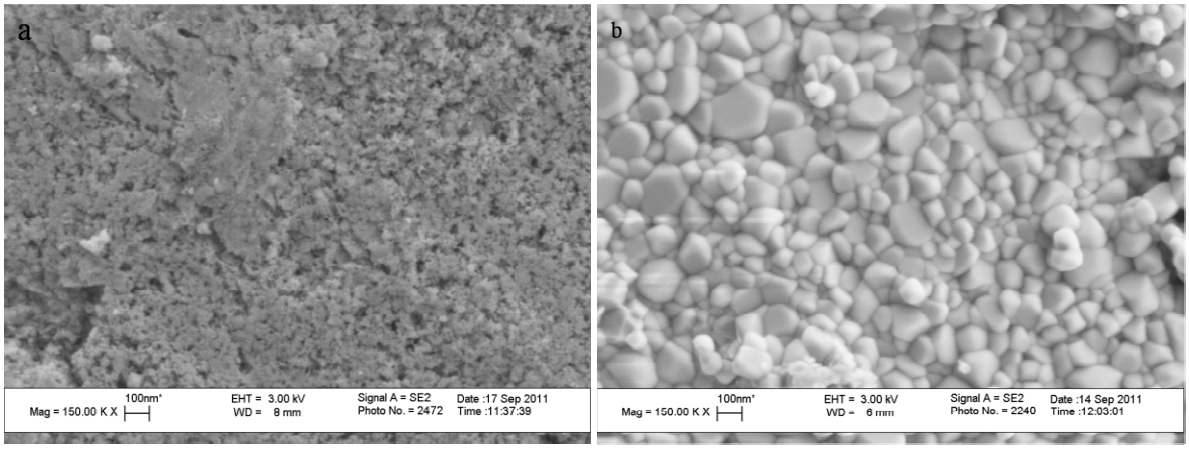

Figure 3.7. (a) SEM images of the SDC (N20) heat-treated at 700 °C for 1 hour (b) SEM images of the SDC (N20) after heat-treated at 1100 °C for 8 hours.

3.1.3. Electrical Properties of Components of the Electrolyte

The temperature dependent electrical conductivity plots of the pure SDC (N20), Na_2CO_3, and $NaHCO_3$ are illustrated in Figure 3.8 for comparison. The Na_2CO_3 and $NaHCO_3$ pellet were heat-treated at 700 °C for 1 hour. In order to obtain a comparable density, the SDC (N20) pellet was heat-treated at 1100 °C for 8 hours. The electrical conductivity was calculated from the impedance tests described in detail in the experimental part.

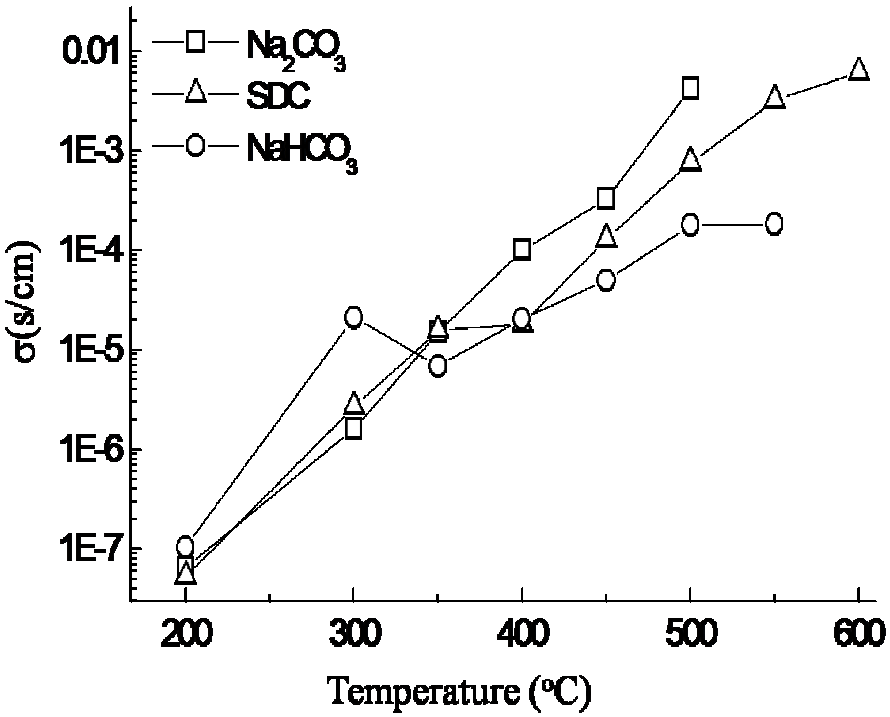

Figure 3.8. The conductivity plots of SDC, Na_2CO_3 and $NaHCO_3$ measured at the temperature between 200 °C and 600 °C. (Na_2CO_3 is presented by squares, SDC is presented by up-triangles, and $NaHCO_3$ is presented by circles).

The table 3.1 summarizes the calculated electrical conductivity of the SDC, Na_2CO_3 and $NaHCO_3$ at 3 different temperatures, such as 200 °C, 300 °C and 450 °C.

Table 3.1. Electrical conductivity of the SDC, Na_2CO_3 and $NaHCO_3$ at different temperatures.

Sample	Conductivity($S.cm^{-1}$) @ 200 °C	Conductivity($S.cm^{-1}$@ 300 °C	Conductivity($S.cm^{-1}$) @ 450 °C
Na_2CO_3	$6.4x10^{-8}$	$1.6x10^{-6}$	$3.3x10^{-4}$
$NaHCO_3$	$1.03x10^{-7}$	$2.1x10^{-5}$	$4.9x10^{-5}$
SDC	$2.4x10^{-7}$	$4.9x10^{-6}$	$6.3x10^{-4}$

At 200 °C, conductivity values of the SDC, Na_2CO_3, and $NaHCO_3$ were corresponding to $2.4x10^{-7}$ $S.cm^{-1}$, $6.4x10^{-8}$ $S.cm^{-1}$, and $1.03x10^{-7}$ $S.cm^{-1}$, respectively. When the temperature level was increased to 300 °C, conductivity values of the SDC and Na_2CO_3 increased to $4.9x10^{-6}$ $S.cm^{-1}$, $1.6x10^{-6}$ S.cm-^{1}, and $2.1x10^{-5}$ $S.cm^{-1}$ respectively. At 450 °C, conductivity values of the SDC, Na_2CO_3 and $NaHCO_3$ were $6.3x10^{-4}$ S.cm-^{1}, $3.3x10^{-4}$ $S.cm^{-1}$, and $4.9x10^{-5}$ $S.cm^{-1}$, respectively.

3.2. Thermal Properties

Properties of the composite electrolyte, in particular the density and morphology, depended on various parameters that could be divided into three groups: Na_2CO_3 properties, SDC oxide properties, and processing conditions (heat-treatment and milling). In the following part, processing conditions were the main parameter in order to systematically investigate the effect of each constituent phase. Thermal responses of powder compacts and heat-treated pellets were analyzed using a simultaneous differential thermal analysis (STA) system. DTA analysis was carried out on as-received SDC (HP) powders, SDC (N20) powders, Na_2CO_3 powders, and dried powder of as-received Na_2CO_3, after having dissolved it in water to determine the temperature dependent physical behavior. Figure 3.9 (a) shows that SDC (HP) and SDC (N20) powders have identical DTA thermograms. The exothermic up-swing in the curve at the temperature of 980 °C, was possibly due to the start of sintering in the powder compacts. Other than that, no other thermal event was observed in the DTA thermogram of SDC. Figure 3.9 (b) shows DTA and TGA thermograms of the as received Na_2CO_3. The endothermic reactions are shown downward in this thermogram. Water evaporation occurred just above

100 °C. Melting of the Na_2CO_3 occurred at 830 °C. This temperature was also the starting temperature of the decomposition of the carbonate.

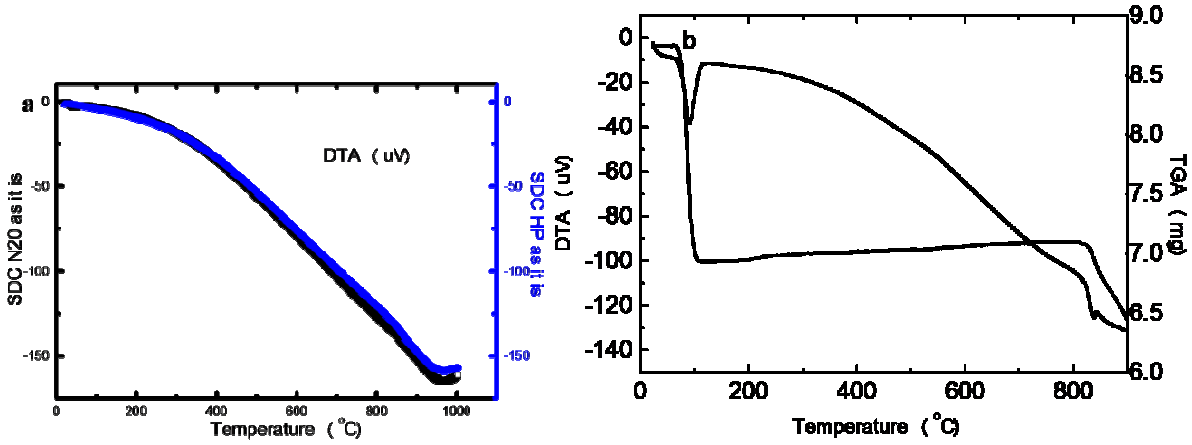

Figure 3.9. (a) DTA thermogram of SDC (HP) and SDC (N20). (SDC (N20) is represented by black line; the SDC (HP) is represented by blue line); (b) DTA/TGA thermogram of the as received Na_2CO_3.

Figure 3.10 (a) displays the DSC/DDSC analysis of the as-received Na_2CO_3 powder. The step change in the baseline of the DSC curve corresponding to a change in the heat capacity is typical of a glass transition type of event for an amorphous material. Therefore, it could be indicative of a glass transition-like softening process in the amorphous Na_2CO_3 matrix. The lighter color curve in the graph in Figure 3.10 is the derivative of the DSC signal. The thermal behavior of the Na_2CO_3 was further investigated by the dilatometer spectrum of a non-heat-treated Na_2CO_3 pressed pellet in Figure 3.10 (b). At 430 °C, the glass transition-like softening (and consequent deformation) of the Na_2CO_3 was occurred before the melting of the Na_2CO_3 (at 850 °C).

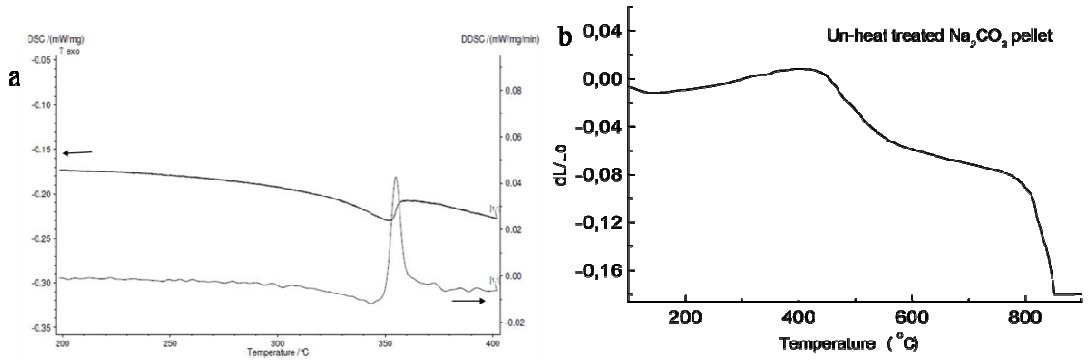

Figure 3.10. (a) DSC /DDSC analysis of the as-received Na_2CO_3 powder and (b) Dilatometer spectrum of non-heat-treated Na_2CO_3 pressed pellet.

Figure 3.11 (a) shows DTA/TGA thermograms of the dried powder of as-received Na_2CO_3 that was dissolved in water first. The evaporation of absorbed water occurred around 100 °C, an endothermic decomposition occurred at 140 °C and melting of the Na_2CO_3 started at 830 °C. The 830 °C was also the starting temperature of the decomposition of the carbonate. Very similarly, Figure 3.11 (b) shows DTA/TGA thermogram of the as-received $NaHCO_3$. An endothermic decomposition occurred at 140 °C and melting of the Na_2CO_3 occurred at 830 °C as part of the endothermic reactions.

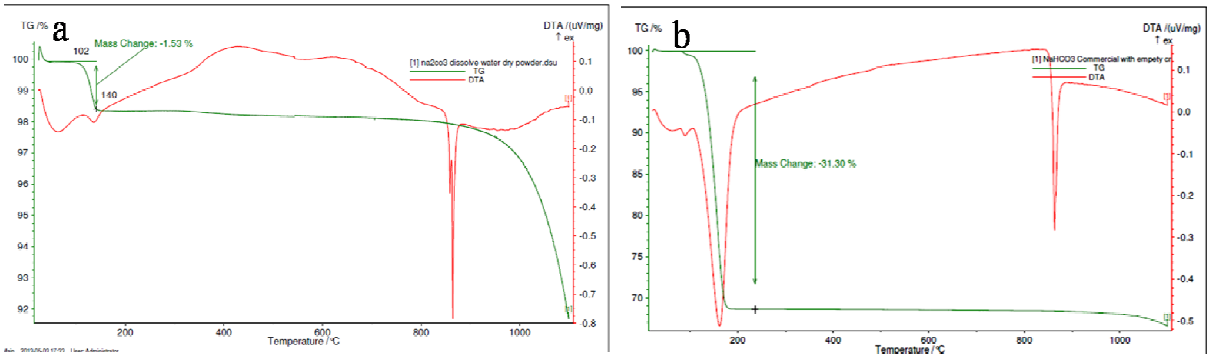

Figure 3.11: DTA/TGA thermogram of (a) the dried powder of Na_2CO_3 after dissolved in water and (b) as received $NaHCO_3$.

An SEM investigation was carried out before and after heat-treatment of Na_2CO_3 in the pellets form in order to study the effect of the heat-treatment on the sintering and morphology of the pellet. Figure 3.12 (a) shows the Na_2CO_3 pellet surface (before heat treatment) having visible pores. On the other hand, Figure 3.12 (b) reveals semi-glassy and semi-crystalline pellet surface, due to heat-treatment. Sample surface of the heat treated (sintered sample) showed strong effects of humidity on the phase formation in the carbonate pellet. The x-ray analysis was performed on this sample (after heat treatment). It does not reveal any monosodium carbonate peaks. It may signify monosodium carbonate so localized to the surface, therefore that their intensity was very low.

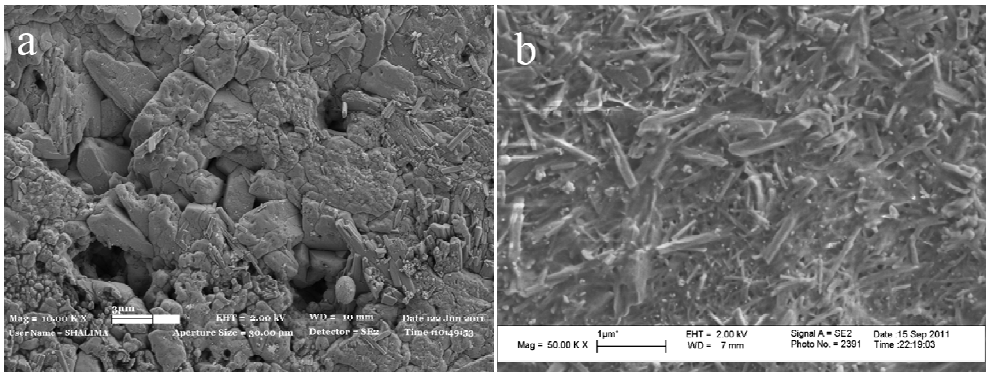

Figure 3.12. SEM images of the Na_2CO_3 pellet (a) before and after (b) heat-treated at 700 °C.

3.3 The Effect of Sintering Temperature on Composite Electrolyte's Electrical Property

In order to find out at which temperature the composite can reach highest possible density (above 95%), 4 different heat-treatment temperatures were investigated. The upper heat-treatment temperature was selected with the melting temperature of the Na_2CO_3 in mind to avoid melting of the samples in the furnace or in the testing apparatus. The temperature dependent electrical conductivity plots of the SDC (HP) Na_2CO_3 10 wt% composite as a function of sintering temperature were demonstrated in Figure 3.13 for comparison. In order to keep the comparability of the experiments, all pellets were heat-treated at respective temperatures for 1 hour. The electrical conductivity was calculated from the impedance tests described in detail in the experimental part.

The Figure 3.13 shows that electrical conductivity of the SDC (HP) composite at constant 10 wt% Na_2CO_3 that were sintered at different temperatures. As the temperature of the testing increased the differences between samples sintered at different temperatures decreased. For example at 200 °C, the composite sintered at 850 °C had the highest conductivity value of 1.54×10^{-7} $S.cm^{-1}$. At the same temperature, the composite sintered at 700 °C had the lowest conductivity value of 2.74×10^{-8} $S.cm^{-1}$. For instance, at 200 °C, conductivity of the composite sintered at 850 °C was 2.2 times higher than that of the composite sintered at 700 °C. However in the temperature range from 300-600 °C the conductivity difference gradually decreased. For example, at the 400 °C, conductivity of the 850 °C composite was only 1.4 times higher than that of composite sintered at 700 °C. The slopes of all four log conductivity

curves were very close to each other signifying a single underlying mechanism of conduction in all four samples.

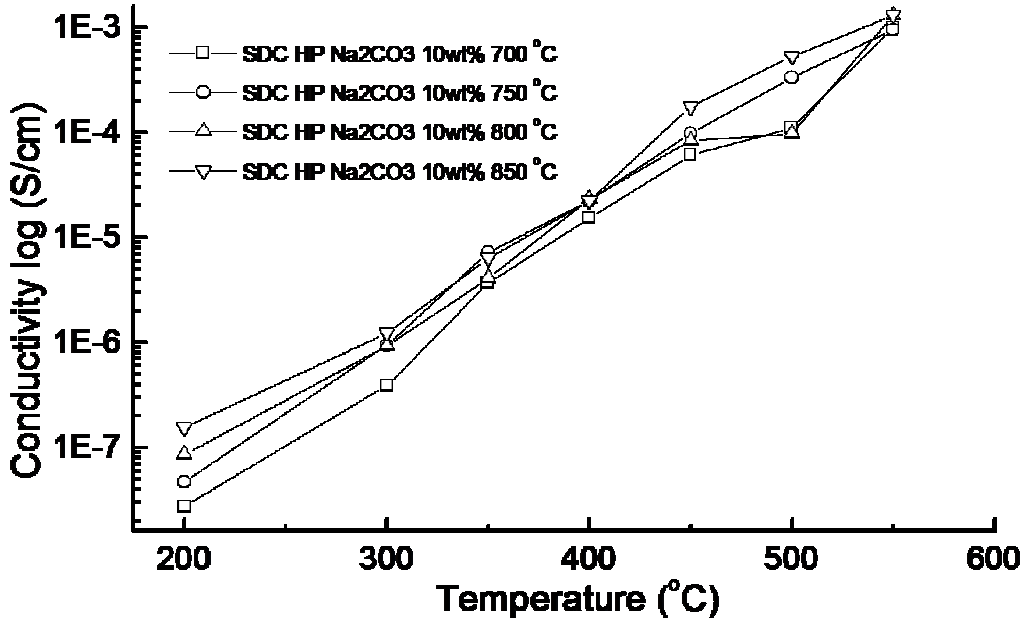

Figure 3.13 The calculated electrical conductivity of the SDC (HP) composite at constant 10 wt% Na_2CO_3 amount. All the composites were sintered at varied temperatures for 1 hour. (squares are 700 °C, circles are 750 °C, up-triangles are 800 °C, and down-triangles are 850 °C heat-treatment condition. All measurements were taken in air at temperatures between 200 °C and 600 °C.

There are two main reasons that will account for the variation in the conductivity of the composite which have the same carbonate amount. The first reason is the particle size and the second reason is the pellet density. Therefore, the particle size and the microstructure of the SDC (HP) Na_2CO_3 10 wt% pellets after the impedance analysis were imaged to monitor a possible grain growth during sintering at different temperatures and the high temperature electrical measurements. The initial pellet was heat-treated at 700 °C for 1 hour. The composite cross sectional microstructure as imaged at 3 keV and 10 K magnification is illustrated in Figure 3.14 (a). The Figure 3.14 (b) and (c) are present cross sectional

morphology under the electron voltage of 15 keV imaged at 10 K and 50 K magnification. The particle size was in the range of 0.5 μm and they are inter-connected in the composite. In addition, the Figure 3.14 (d) showed the EDX mapping from the region (c). Micrograph taken at 3.0 keV shows the carbonate phase as the darker grey contrast matrix (Figure 3.14 a). The images taken from the same pellet cross section shows mostly the SDC particles which have a high atomic number (atomic number Sm=62 and Ce=58) in comparison to the lower atomic numbered carbonate matrix (atomic number Na=11, C=6, and O=8).

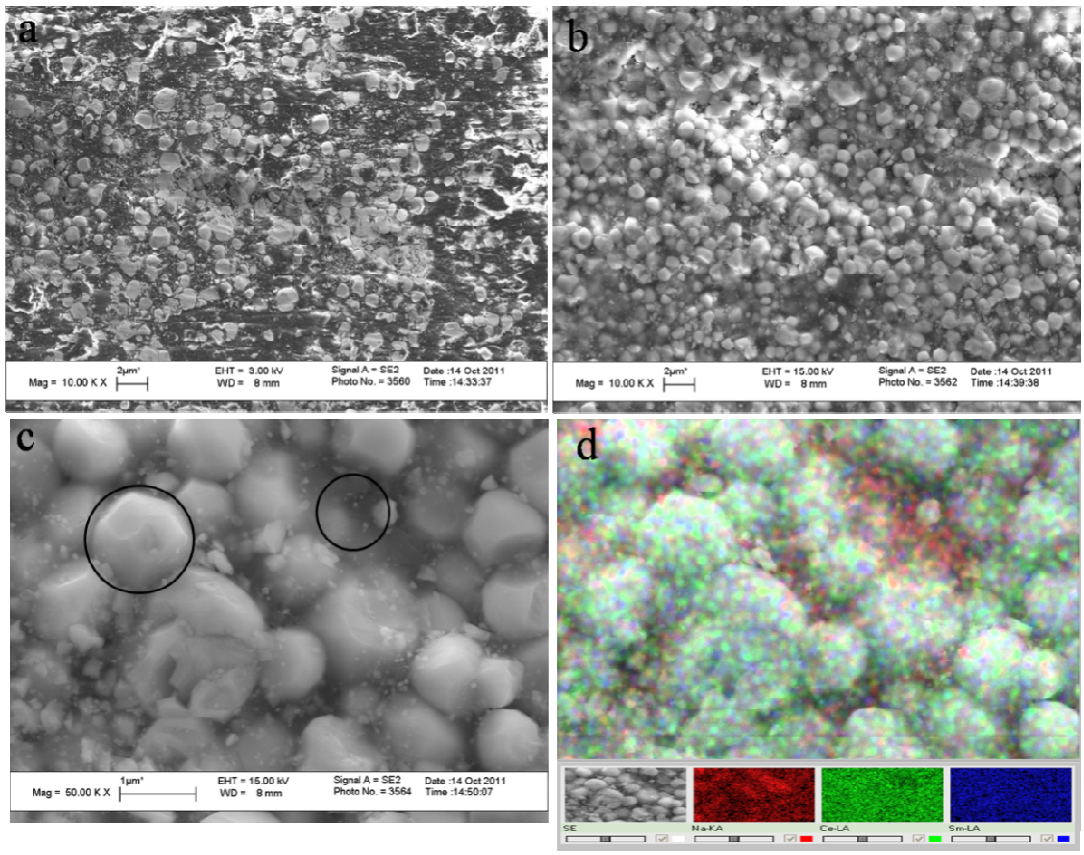

Figure 3.14 Cross Sectional-SEM images of the composites after EIS analysis. Initial composite (SDC HP) contained 10 wt% Na_2CO_3 matrix phase and sintered at 700 ^oC for 1 hour. (a) at 10 K magnification under the 3 keV; (b) at 10K magnification under the 15 keV; (c) at 50 K magnification under the 15 keV; (d) EDX mapping of the image (c)

Secondly, the pellet densities were also measured with a helium- pychnometer. The measured densities of the all composites are presented in Figure 3.15. The composite which was sintered at 700 °C have the highest density and have around 98% density. The densities of all samples sintered between 600 °C and 800 °C were within the experimental measurement errors.

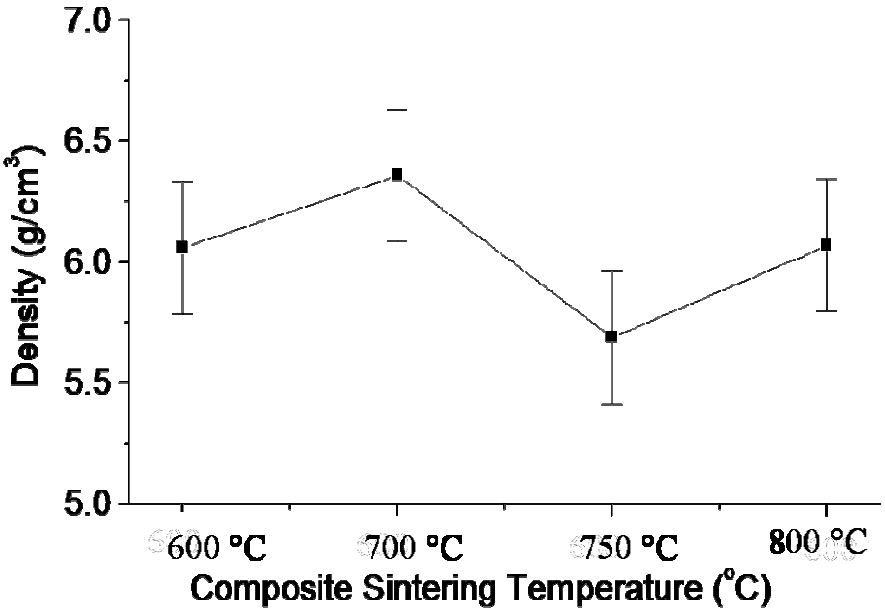

Figure 3.15. Calculated density of the composites. All composites (SDC HP) contained 10 wt% Na_2CO_3 matrix phase and sintered at varied temperatures for 1 hour. The pellets were sintered at 600 °C, 700 °C 750 °C, and 800 °C.

3.4. The Effect of Processing on the Properties of the Composite Electrolyte

Figure 3.16 shows SEM images of the composites containing 5 wt% Na_2CO_3 prepared with nano-sized SDC (N20) oxide particles, as imaged by secondary electrons (SE-SEM) in cross-section. The Figure 3.16 (a) and (c) are images of the composite where the powder mix was ball milled in water. On the other hand, the Figure 3.16 (b) and (d) illustrates the composite

for which the powder mixes were dry ball milled. All four images are very similar in terms of composite morphology such as, particle/phase distribution and particle sizes. The high average atomic number of the samarium doped ceria (SDC) particles facilitated identification of individual oxide particles embedded into the carbonate matrix in the composite. For instance, the lower atomic number Na_2CO_3 matrix phase (transparent dark contrast) and the higher atomic number SDC particles (bright particles) are delineated with circles in Figure 3.16 (a). The image reveals that Na_2CO_3 covered the SDC particle surfaces and constituted the matrix phase in the composite microstructure. The cross-section SEM image also showed that the average grain size of SDC (N20) in the composite is smaller than 200 nm and the relative pellet density is ≥98%. Na_2CO_3 appears to have served as the glue for the oxide particles. In the microstructure revealed by high (15) keV imaging, both component phases appeared to be interconnected in 3 dimensions (D). The edges of the prismatic shapes of the oxide particles could be recognized.

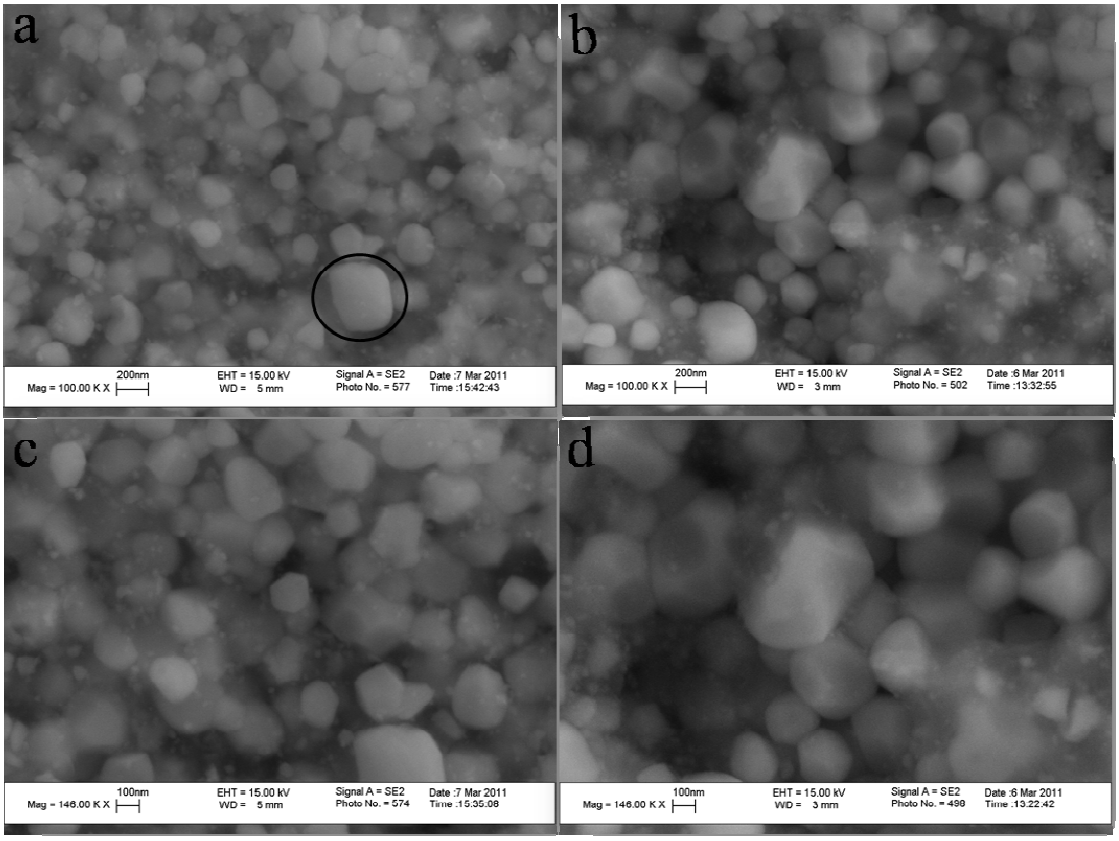

Figure 3.16. SEM images of the SDC (N20) 5 wt% Na_2CO_3 composite (a) with solution processing at 100 K and (c) 146 K magnification; with dry ball milling (b) at 100 K and (d) 146 K magnification.

Figure 3.17 shows images of the composite containing 5 wt% Na_2CO_3 prepared with nano-sized SDC (N20) oxide particles, as viewed in cross-section SEM images. The composite was prepared by dry ball milling process. The Figure 3.17 (a) and (b) are images taken with an in-lens detector at 5 keV and inverted in-lens image. The inverse image was obtained by an image processing program. The micrographs taken with the in-lens detector made it possible to image the low atomic number carbonate matrix. In Figure 3.17 (a) the SDC particles imbedded in Na_2CO_3 matrix phase in the composite microstructure are visible. Na_2CO_3 phase appeared to have served as the glue for the oxide particles. The imaged morphology illustrated a core-shell structure with SDC particles cores and carbonate shell. The thickness

of the Na_2CO_3 shell imaged with SEM appeared to be around 20 nm. Figure 3.17 (c) was obtained at 15 keV with an SE detector. The EDX elemental mapping of the same region is presented in Figure 3.17 (d). In the EDX mapping, both component phases appeared to be interconnected in 3D and Na_2CO_3 seemed to cover all the SDC particle surfaces.

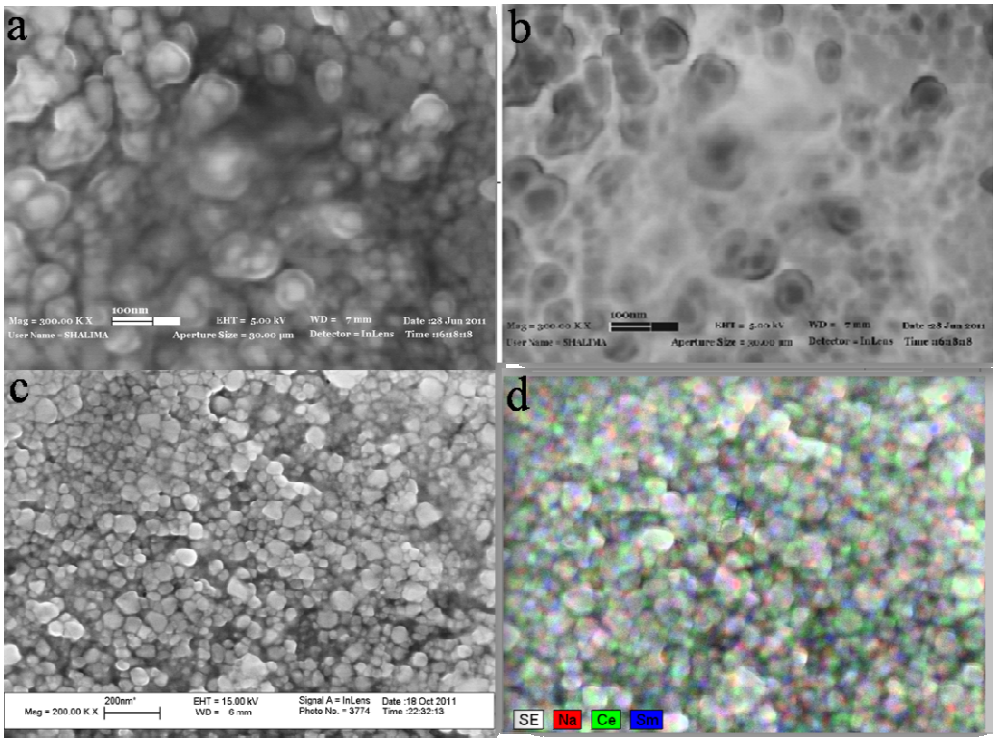

Figure 3.17. SEM images of the SDC (N20) 5 wt% Na_2CO_3 composite by dry ball milling process (a) surface (b) inverse SE-image, (c) cross section, and (d) EDX of the (c).

The thermal responses of the prepared composite powders were analyzed using a simultaneous thermal analysis (STA). In Figure 3.18 the TGA thermograph curves of the solution processed composite powder (SDC (N20) with 5 wt% Na_2CO_3) and that of dry ball milled composite powder were compared to each other. For these two composite powders, the weight losses up to 700 °C were compared to each other. The TGA spectrum of the ball milled composite powder revealed ~ 14% weight loss, which corresponds to the losing water

of Na_2CO_3 ($Na_2CO_3.H_2O$ would decomposed to Na_2CO_3 and H_2O (gas), in this reaction, the total weight change from 124 atomic mass unit (amu) to106 (amu)).

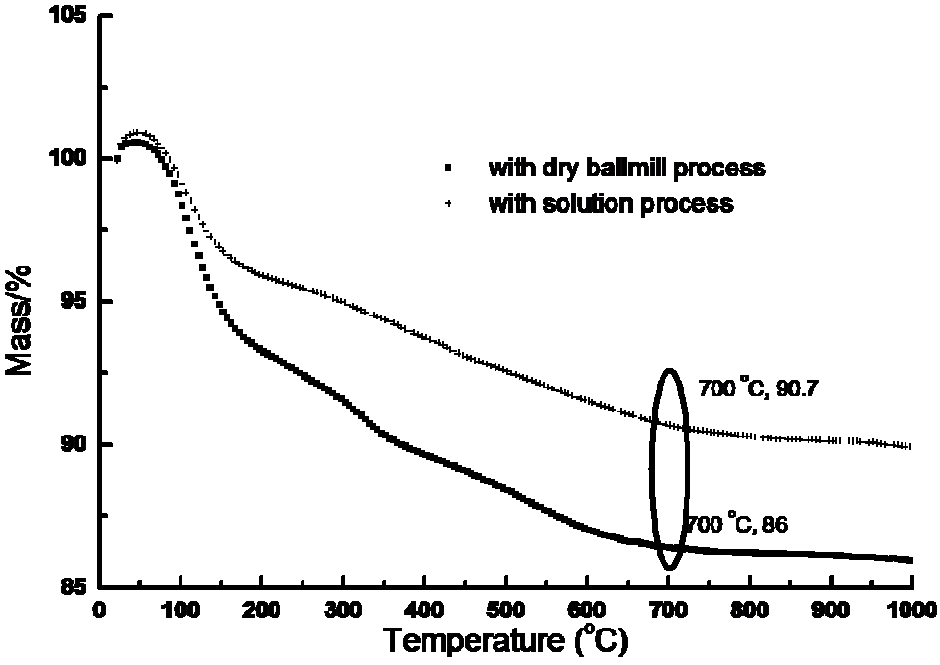

Figure 3.18. TGA thermograms of SDC (N20) 5 wt% Na_2CO_3 composite powders. Dry ball milled powder was represented by solid squares; the solution process was represented by crosses.)

Raman spectra of composites and SDC powders were obtained using a blue laser (532 nm wavelength) for comparing the significance of the processing conditions (shown in Figure 3.19). Both dry ball-milled and solution processed powders' Raman spectra were very similar (Figure 3.19 (a)). At around the Raman shift around 3000 cm^{-1}, some weak wiggles could be observed for the powders that were prepared by the water based solution process. From the comparison of characteristic peaks in Figure 3.19 (b), only one peak could be distinguished at 2000 cm^{-1} which is belonging to CO_2. The solution processed powder (Figure 3.19 b (2)) has more tendencies to absorb the CO_2.

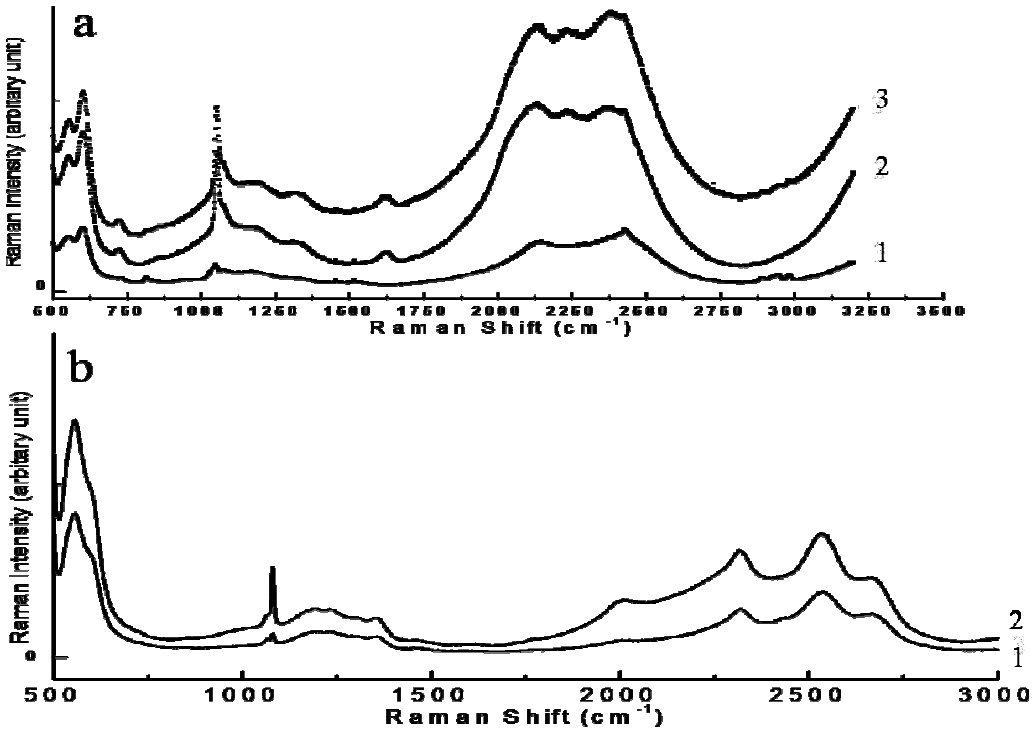

Figure 3.19 **(a)** Raman patterns of the (1) as received SDC (N20); (2) dry milled; and (3) solution processed composite SDC (N20) Na_2CO_3 5 wt%. **(b)** Raman patterns of the SDC (HP) Na_2CO_3 10 wt% composite calcined at 700 °C for 1 hour. By (1) dry and (2) solution process.

Figure 3.20 presents a Nyquist plot of imaginary impedance (-Z″) versus real impedance (Z′) which are belong to SDC (N20) 5 wt% Na_2CO_3. For all measured temperatures, *i.e.,* between 200 and 600 °C, the impedance of the composites with different processing procedure showed a similar trend but different resistivity values. For instance, at 200 °C, dry ball milled composite's impedance conductivity value is $5.23x10^{-6}$ $S.cm^{-1}$, while solution processed composite impedance conductivity value is $1.47x10^{-5}$ $S.cm^{-1}$. At 200 °C, composites that went through water based processing route were the ones with the lowest impedance resistivity values, *i.e.,* with the highest conductivities.

At 300 °C, composite's impedance spectrum consists of two overlapping semi-circle arcs at high frequencies and a portion due to electrode polarization at low frequencies. At temperatures above 450 °C, the complex impedance response (Nyquist plots) of all composite revealed only one dominant semi-circular arc. At 600 °C, both pellet produced nearly identical spectra.

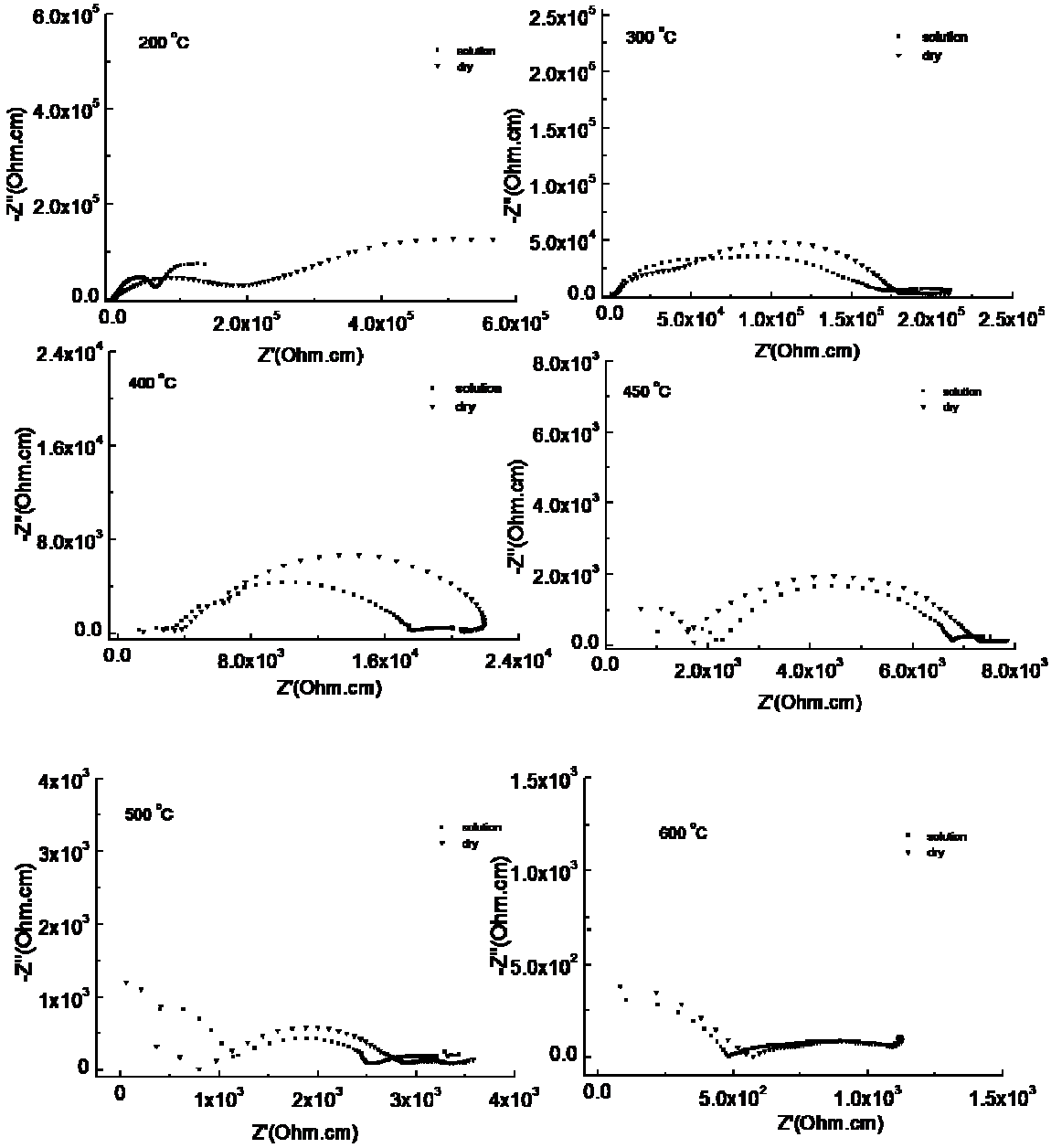

Figure 3.20. The impedance spectra and spectroscopic spectra of the SDC (N20) composite with varied process at constant 5 wt% Na_2CO_3 amount. Solid squares are solution and down-triangles are dry ball milled composites. All measurements were taken in air at temperatures between 200 ^oC and 600 ^oC. Both composite pellets were sintered at 700 ^oC for 1 hour.

3.5. The Effect of Milling on Composite Electrolyte Production

The milling parameter was another concern of the processing condition of the composite as one of the key factors for obtaining the ideal composite. Table 3.2 summarizes the experimental design and characterization method of this section. The milling parameters were initially studied by the DTA tests so that the associated changes in the thermal behavior can be detected.

Table 3.2. Design of the Characterization.

	SDC (HP) Na_2CO_3 wt%10 milled	SDC (HP) Na_2CO_3 wt%10 mixed
DTA	850 ^oC peak	850 ^oC peak
XRD	SDC peaks	SDC peaks and 2θ of 31^o
Raman	SDC Intensity and peaks at 1050 ^{o}	SDC Intensity

Figure 3.21 (a) presents the DTA analysis of the SDC with 10 wt% Na_2CO_3 composites of. Both DTA thermogram (in Figure 3.21 (a)) showed the melting of the Na_2CO_3 at 850 ^oC.

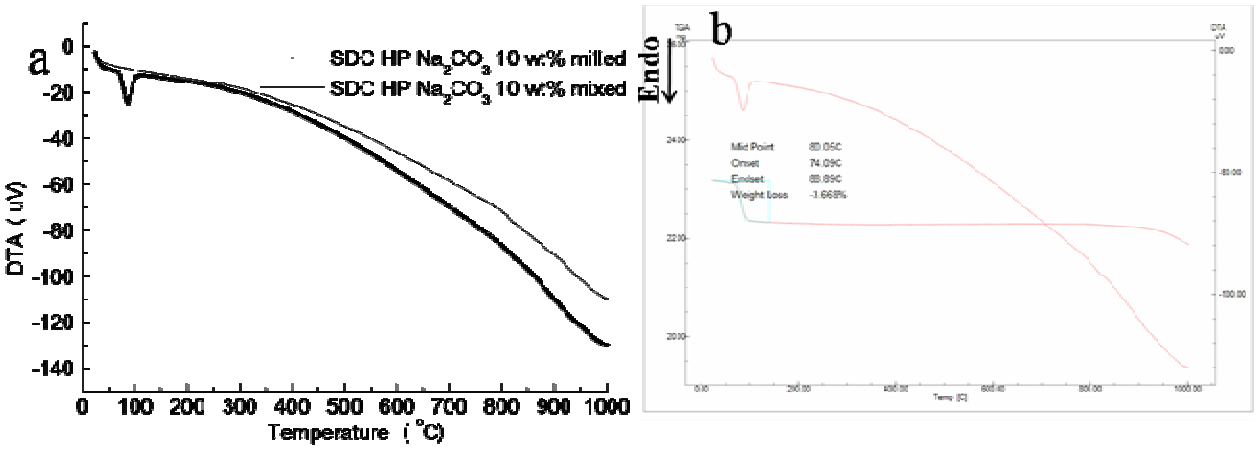

Figure 3.21. (a) DTA thermogram of milled and physically mixed composites of SDC (HP) Na_2CO_3 10 wt% (DTA thermogram of milled composites was represented by light line; and physically mixed composites was represented by dark line). (b) TGA and DTA thermogram of milled composites of SDC (HP) Na_2CO_3 10 wt%.

Both thermograms have a water evaporation peak around 100 ^{o}C. However, water evaporation peak for the mixed sample is pronounced. TGA of the milled composite powder (in Figure 3.21 (b)) showed weight loss after melting temperature of carbonate.s

In the following part, Na_2CO_3 concentration conditions were held constant, in order to systematically investigate the effect of milling on the structural properties. To see the effect of the milling process on the structural properties of the composite powders, XRD was performed (in Figure 3.22). The SDC (HP) Na_2CO_3 10 wt% powders were prepared by 2 different processing conditions. First, the powders were ball milled for 6 hours and next the collected powders were characterized by XRD. The second set of powder was prepared by simply combining Na_2CO_3 and SDC powders in a physical mixture without further treatment. In all XRD spectra, major peaks are belonging to samarium doped ceria (SDC).

Distinguishable Na_2CO_3 peaks at the 2θ of 34°, 35° and 42° were observed for the physically combined powder.

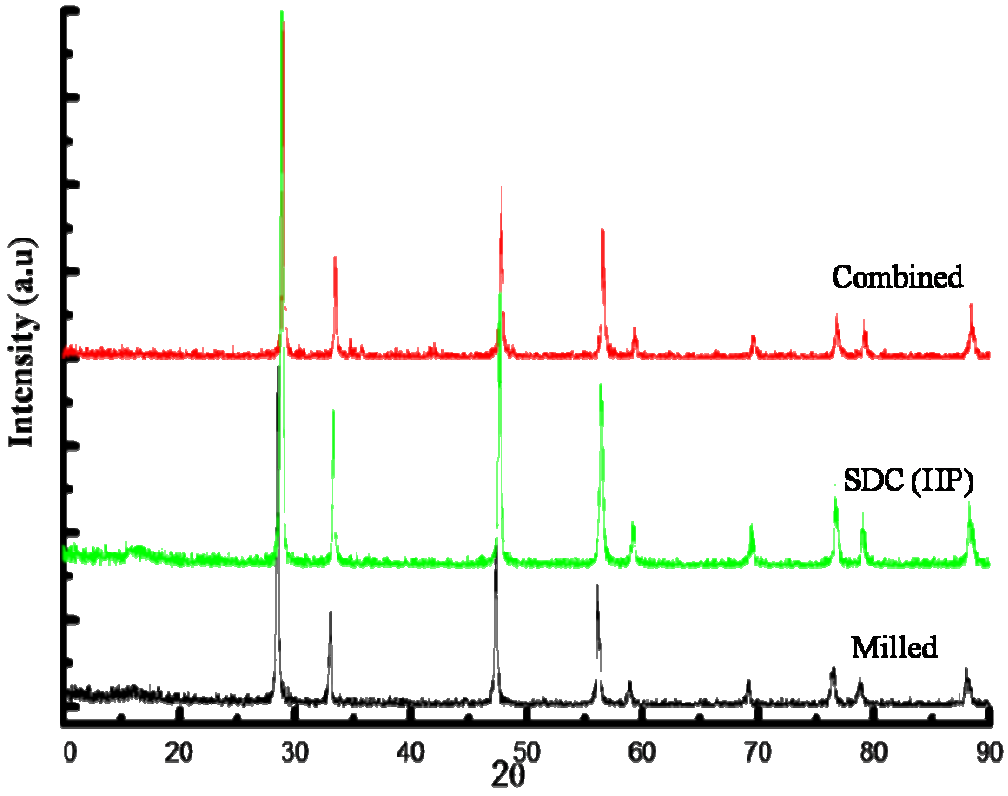

Figure 3.22. Room temperature XRD patterns of composites of SDC (HP) Na_2CO_3 10 wt% milled and physically mixed the each component. SDC (HP) XRD patterns were presented for relatively comparison of the structural changes.

Raman spectra of the composites and the pure SDC powders were obtained using a blue laser for detecting the signature signal of the Na_2CO_3 (in Figure 3.23). From the characteristic peaks of Na_2CO_3 detectable by Raman spectroscopy using He-Ne laser an excitation of λ= 663 nm, only two peaks could be distinguished at 1067 cm^{-1} and 3258 cm^{-1}, which can be attributed to absorbed water molecules. In addition, perturbations to the peaks were more distinctive for the milled composite's Raman spectra, as the milling lead to an increased

intensity of the peaks at around 1067 cm^{-1} and 2000 cm^{-1}. Measurements from the surface of composites demonstrated that it is possible to detect Na_2CO_3 even if it existed in such small amounts. The Raman spectrum from crystalline and amorphous carbonate was listed in the appendix 2. The changes in the intensity of the peaks located at 1100 cm^{-1} is significant.

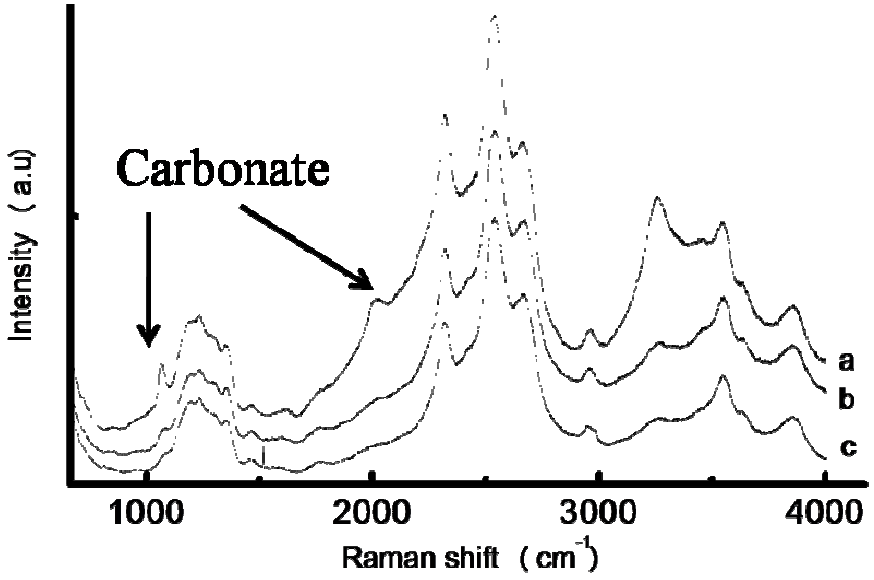

Figure 3.23. (a) Raman patterns of the milled composite SDC (HP) Na_2CO_3 10 wt% (b) Raman patterns of the composite of the physically combined SDC (HP) Na_2CO_3 10 wt%. (c) Raman patterns of the SDC (SDC HP).

3.6. The Detection of Na_2CO_3

As mentioned in the previous section, properties of the composite electrolyte, in particular the density, morphology and electrical properties, depend on various parameters. Designing an optimum composite is a complicated process that could be dominated by various parameters acting in tandem, such as Na_2CO_3 matrix amount and processing conditions (heat treatment and milling). The table 3.3 summarizes the experimental design and characterization method

of this section. In the following section, the milling parameter was held constant, in order to systematically investigate the effect of milling and heat treatment on the crystal structure of the composites.

Table 3.3. Design of the Experiments and Characterizations

	SDC (HP) Na_2CO_3 10 wt% milled	SDC (HP) Na_2CO_3 50 wt% milled	SDC (HP) Na_2CO_3 50 wt% mixed	SDC (HP) Na_2CO_3 50 wt% 700 °C	SDC	Na_2CO_3
XRD	✓	✓	✓	✓	✓	
Raman			✓		✓	✓
DSC		✓				

In Figure 3.24 the XRD spectra of the two composites, SDC (HP) Na_2CO_3 10 wt% and 50 wt% are presented. Despite the fact that both composites are having vastly different composition ratios, both of them have almost identical XRD spectra. Only differences in the two spectra could be identified at 2θ of 28-42°. In Figure 3.24 inset, one could see the monohydrate diffraction peaks at 2θ of 33°, 36°, and 37°. At 2θ of 34°, 35° and 40°, Na_2CO_3 diffraction peaks were seen in Figure 3.14.

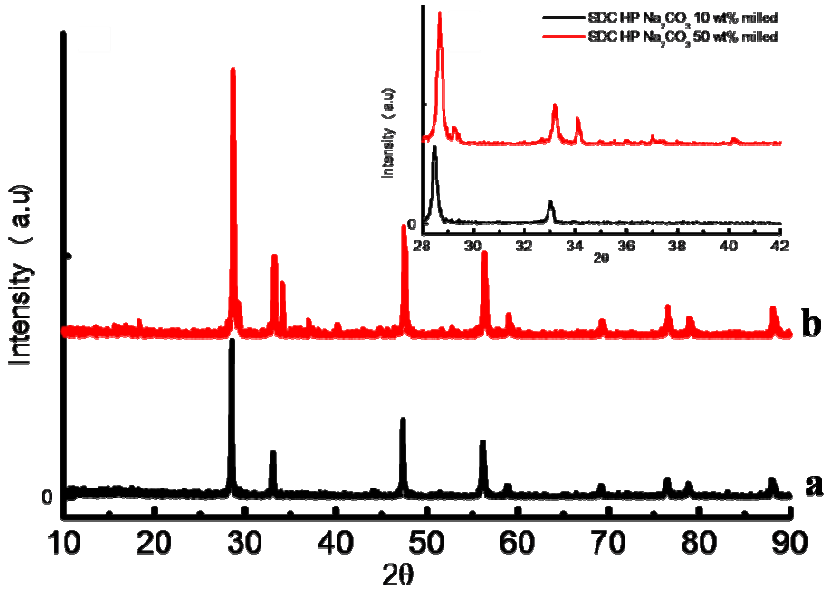

Figure 3.24. Room temperature XRD patterns of the milled composite of SDC (HP) Na_2CO_3 10 wt% and 50 wt%. The inset: magnified portion of the XRD spectra in the 2θ range from 28-42°. (SDC (HP) Na_2CO_3 10 wt% was represented by(b)and SDC (HP) Na_2CO_3 50 wt% was represented by (a).)

Secondly, in this part, Na_2CO_3 to SDC ratio was the kept constant to follow the effect of milling process parameter and heat treatment process on the crystal structure of the composites. The XRD patterns were recorded for combined, milled and heat-treated (at 700 °C for 1 hour) composite powders. Like the results in Figure 3.25, most of the strong diffraction peaks mainly belonged to the SDC powder. As seen in Figure 3.25, weak intensity peaks belonging to carbonate phase persisted also in the heat-treated powders. The peaks belonging to the monohydrate phase (like the one at 2θ of 33°) did not exist in the heat-treated powders.

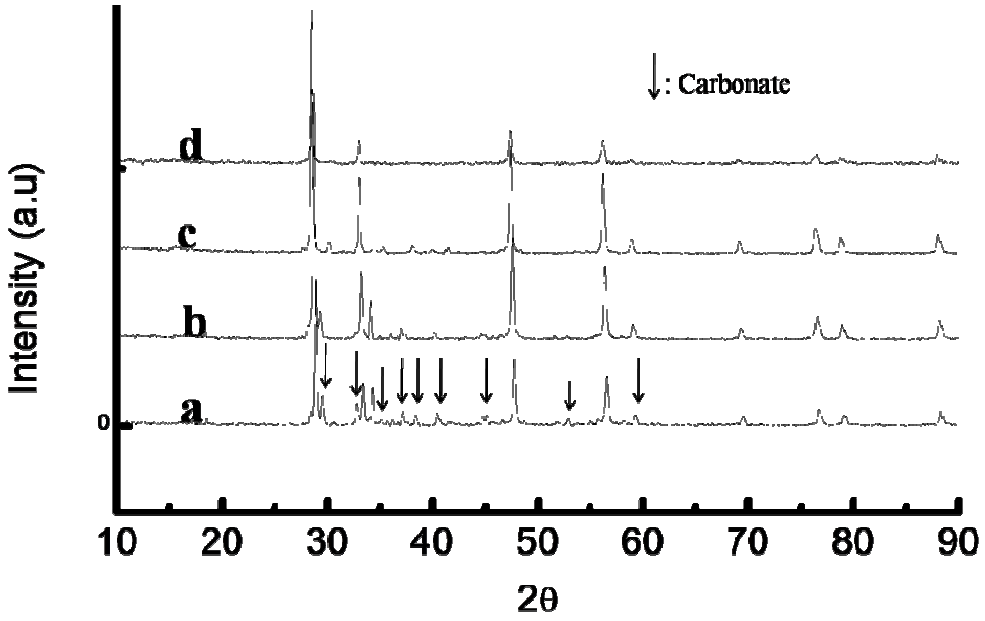

Figure 3.25. Room temperature XRD patterns. (a) mixture of SDC (HP) and 50 wt% Na_2CO_3 (b) milled SDC (HP) 50 wt% Na_2CO_3 (c) after the heat-treated (at 700 °C for 1 hour) (d) as received SDC (HP).

The presence of Na_2CO_3 in the composites was confirmed by Raman analysis in Figure 3.26. Raman spectra compare the Raman shifts in the composite, pure SDC and Na_2CO_3. The peaks at wave-numbers of 1050 cm^{-1}, 1430 cm^{-1}, 1538 cm^{-1}, and 3450 cm^{-1}, are attributed to Na_2CO_3. The highest intensity peak of Na_2CO_3 was present in the composite's Raman spectra. The band at wave-number of 1085 cm^{-1} is due to the internal vibrational modes of the carbonate ion.

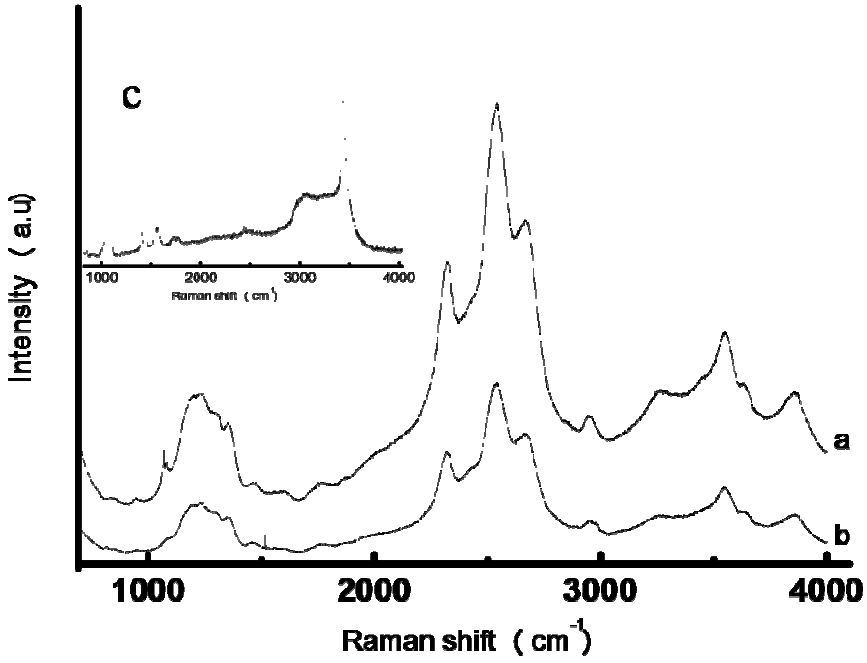

Figure 3.26. (a) Raman patterns of composite of micrometer sized SDC (HP) Na_2CO_3 50 wt% after mixed. (b) Raman patterns of micrometer sized SDC (SDC HP). (c) Inset: Raman patterns of the Na_2CO_3 powder.

In order to confirm whether Na_2CO_3 was amorphous, crystalline or in partially amorphous form in the composite, DSC was performed on the milled SDC (N20) composite with 50 wt% concentration of Na_2CO_3. Figure 3.27 shows the DSC analysis of the SDC (N20) composite powder with 50 wt% Na_2CO_3 concentrations. In the temperature range between 300 and 335 °C, a broad exothermic peak was observed. This *step change in the baseline of the DSC* is very similar to the thermal phenomena *of the as-received Na_2CO_3 powder* (shown in Figure 3.9 (a)). Therefore, it could be a glass transition-like softening process of the amorphous Na_2CO_3 matrix in the composite.

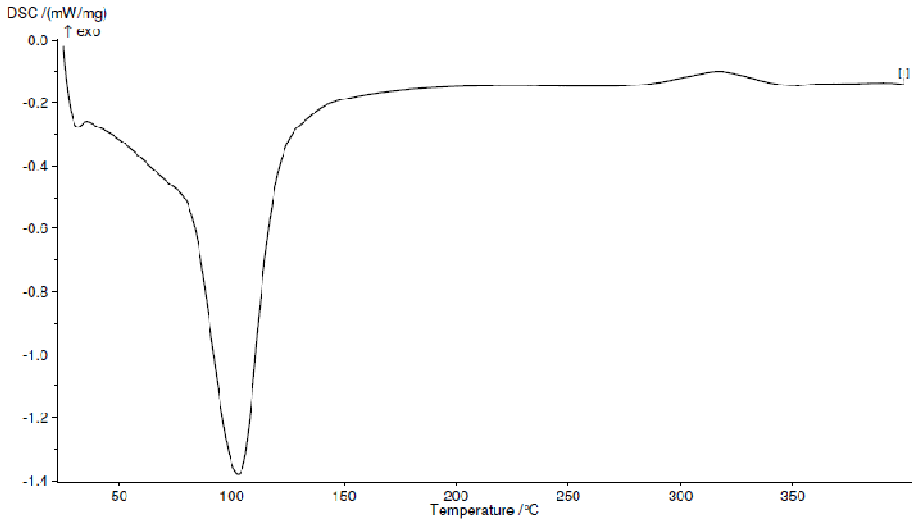

Figure 3.27. The DSC thermogram of the milled composite SDC (N20) Na_2CO_3 50 wt%. The DSC was performed on the powder.

3.7. Effect of $NaHCO_3$ and Na_2CO_3 on SDC (N20 or HP) Composites

As mentioned in the previous section, designing an optimum composite is a complicated process that could be depended on various parameters, one of which is the processing conditions. One of the possible factors that could emerge during processing was the formation of $NaHCO_3$. Therefore, effect of having a $NaHCO_3$ and Na_2CO_3 mixed carbonate phase on SDC (N20 or HP) composites was studied. The results are presented in this following section.

3.7.1 Effect of $NaHCO_3$ and Na_2CO_3 on SDC (N20) Composite

First, the SDC (N20) carbonate composite system was investigated. In this experimental design the SDC (N20) amount was held constant in the composite, in order to systematically investigate the effect of $NaHCO_3$ and Na_2CO_3 on the electrical properties of the composites.

Figure 3.28 presents a typical Nyquist plot of imaginary impedance ($-Z''$) versus real impedance (Z'). The Nyquist plots in Figure 3.28 are results from room temperature measurements. The composite's impedance spectrum (in Figure 3.28 (a)) includes semi-circle arcs at high frequencies and a non-circular portion due to electrode polarization at low frequencies. The impedance response of the pure Na_2CO_3 (Figure 3.28 (c)) and $NaHCO_3$ (Figure 3.28 (d)) are also included for a comparison. The reported resistivity (Ω.cm) values were calculated from the real axis intercept of the semi-circular arcs in the Nyquist plots.

Figure 3.28 compared the room temperature Nyquist plots of the SDC (N20) composites with varied carbonate type. The SDC (N20) composites with Na_2CO_3 phase were the ones with the lowest impedance values, *i.e.,* with the highest conductivities (Figure 3.28 (a)). Further analysis of the individual Na_2CO_3 and $NaHCO_3$ impedance curves revealed that at room temperature Na_2CO_3 resistivity (Ω.cm) is higher than the resistivity (Ω.cm) of the $NaHCO_3$. However, the composite made from these two carbonate phases did not show the same trend in their impedance as their pure carbonate counterparts, *i.e.,* Na_2CO_3 and $NaHCO_3$.

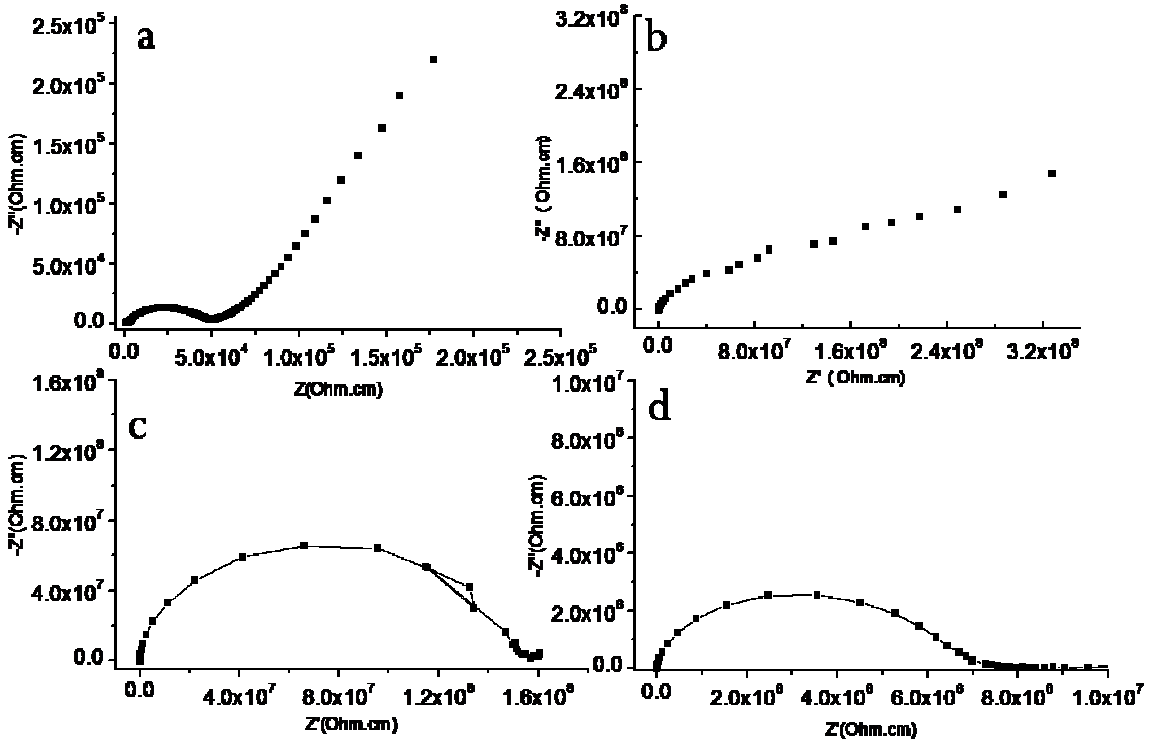

Figure 3.28. RT Nyquist plots of (a) SDC (N20) Na_2CO_3 and (b) SDC (N20) $NaHCO_3$ composites with 20 wt% carbonate content; Nyquist plots of (c) Na_2CO_3 and (d) $NaHCO_3$.The measurements were taken in air atmosphere at room temperature. All composite pellets were heat-treated at 700 ^oC for 1 hour.

Figure 3.29 illustrates Nyquist plots of the SDC (N20) composite with 20 wt% of Na_2CO_3 and $NaHCO_3$. At temperature range between 200 °C to 400 °C, the composite's impedance spectrum included two overlapping semi-circle arcs at high frequencies. However, at 300 °C, the composite's impedance spectrum showed very clearly overlapped semi-circle arcs. For all measured temperatures, *i.e.*, between 200 °C to 500 °C, the impedance of the composites with same amount of Na_2CO_3 and $NaHCO_3$ produced very similar impedance spectra. At 500 °C, composite with Na_2CO_3 had an impedance value of $1.3x10^6$ (Ω.cm) while the composite with $NaHCO_3$ revealed an impedance value around $1.4x10^6$ (Ω.cm).

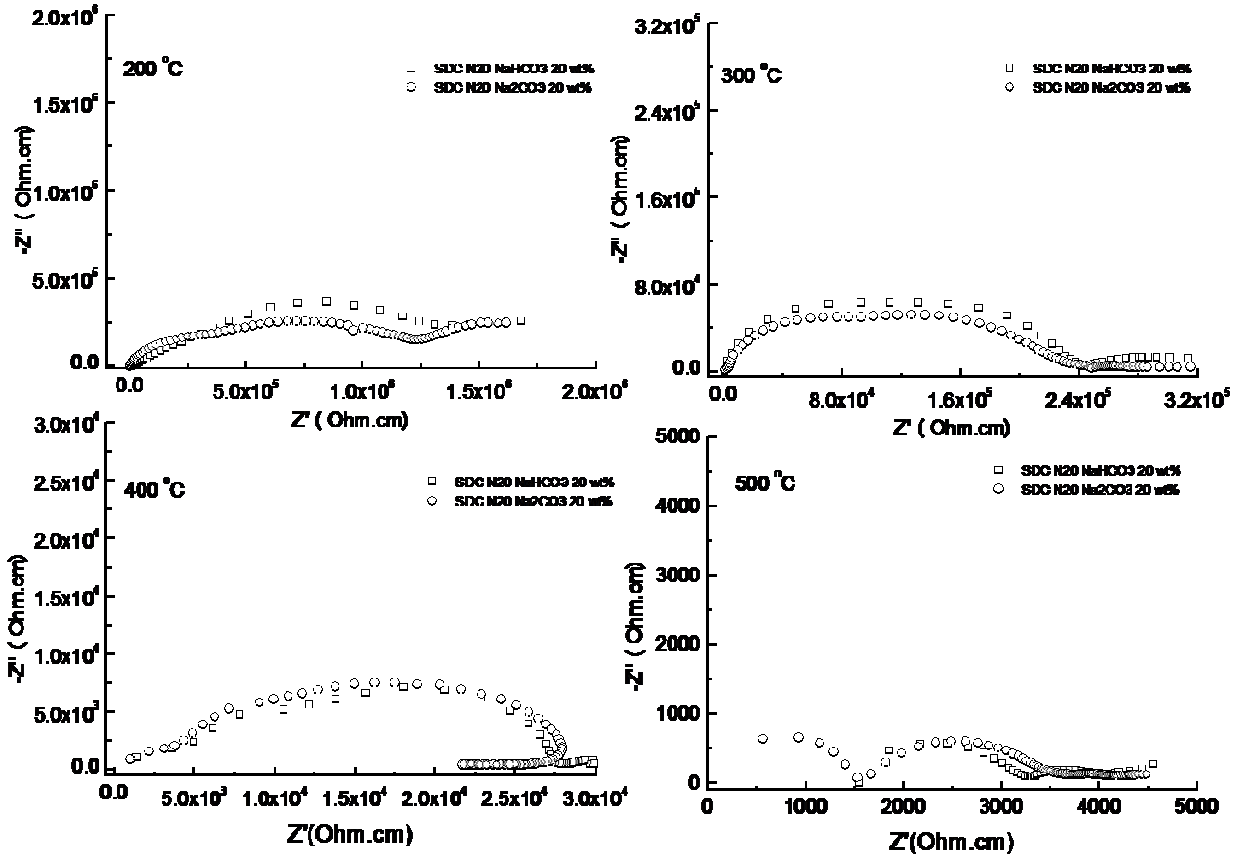

Figure 3.29. Nyquist plots of SDC (N20) Na_2CO_3 (circles) and SDC (N20) $NaHCO_3$ (squares) composites with 20 wt%. The measurements were taken in air atmosphere at temperatures from 200-500 ^oC. All composite pellets were heat-treated at 700 ^oC for 1 hour.

3.7.2 Effect of Na_2CO_3 and $NaHCO_3$ on SDC (HP) Composites

After investigating the nanometer-sized SDC (N20) composite system, effect of Na_2CO_3 and $NaHCO_3$ on the micrometer-sized SDC (HP) composite system was investigated. In this experimental design the carbonate to SDC (HP) amount was held constant at 20 wt%, in order to systematically compare the effect of Na_2CO_3 and $NaHCO_3$ on the electrical properties of the resulting composites.

Figure 3.30 showed again Nyquist plots of imaginary impedance (-Z″) versus real impedance (Z′). The Nyquist plots in Figure 3.30 (a) and (b) are results from room temperature measurements of the SDC (HP) composites with Na_2CO_3 and $NaHCO_3$, respectively. The composite's impedance spectrum (Figure 3.30 (a)) includes semi-circle arcs at high frequencies and a portion due to electrode polarization at low frequencies. The impedance response of the pure Na_2CO_3 (Figure 3.30 (c)) and $NaHCO_3$ (Figure 3.30 (d)) are also included for comparison. Figure 3.30 illustrated that at room temperature, composites with Na_2CO_3 phase were the ones with the lowest impedance values, i.e. with the highest conductivities. Similar to the observations on the SDC (N20) composite system, the composite impedance response did not follow the exact trend with the impedance response of the Na_2CO_3 or $NaHCO_3$.

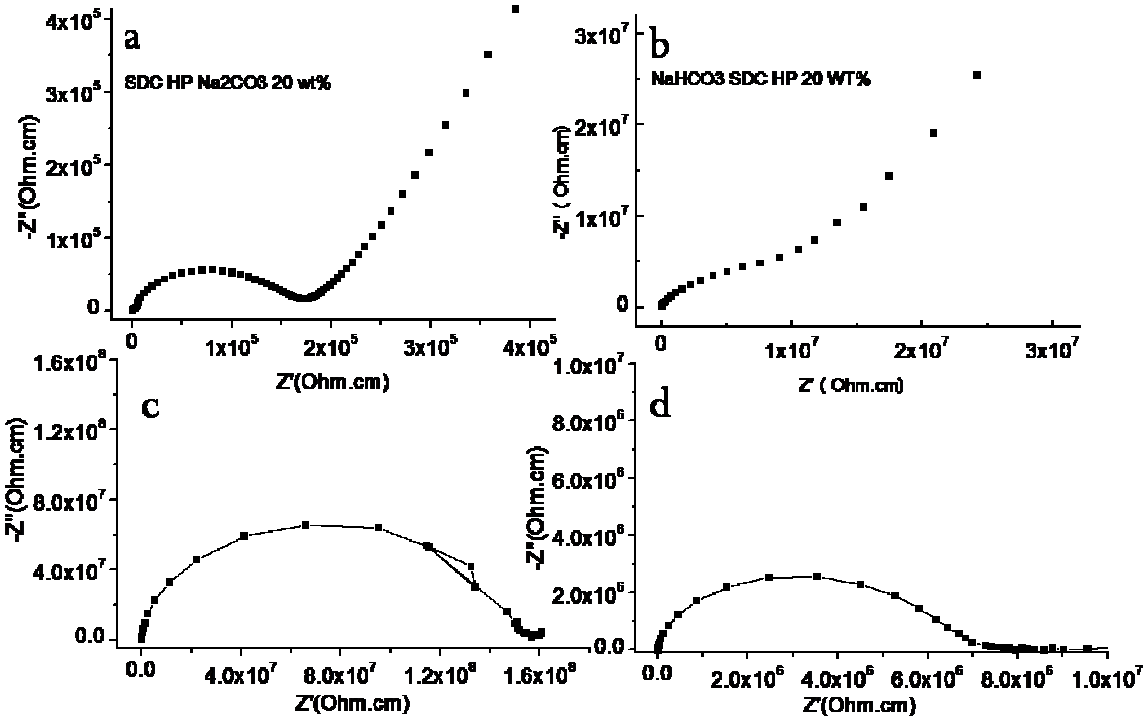

Figure 3.30. RT Nyquist plots of SDC (HP) Na_2CO_3 (a) and SDC (HP) $NaHCO_3$ (b) composites at 20 wt% concentration; Nyquist plots of Na_2CO_3 (c) and $NaHCO_3$ (d). The measurements were taken in air atmosphere at room temperature. All composite pellets were heat-treated at 700 ^oC for 1 hour.

Figure 3.31 illustrates a Nyquist plot of the SDC (HP) composite with 20 wt% of Na_2CO_3 or $NaHCO_3$. At the temperature range from 200 °C to 500 °C, the composite's impedance spectrum included two overlapping semi-circle arcs at high frequencies. For all measured temperatures, i.e. between 200 °C and 500 °C, the impedance of the composites with same amount of either Na_2CO_3 or $NaHCO_3$ produced very different impedance response, *i.e.,* resistivity (Ω.cm) values. For instance, at 200 °C, composites with Na_2CO_3 resulted in an impedance value of $1.8x10^7$ (Ω.cm) while the composite with $NaHCO_3$ gave an impedance value around $4.1x10^7$ (Ω.cm). Similarly, at 300 °C, composites with Na_2CO_3 had an impedance of $1.1x10^6$ (Ω.cm) while the composite with $NaHCO_3$ produced an impedance value around $2.1x10^6$ (Ω.cm). When the temperature was further increased to 400 °C, composites made with Na_2CO_3 resulted in an impedance value of $4.1x10^4$ (Ω.cm) while the composite with $NaHCO_3$ had an impedance value around $9x10^4$ (Ω.cm).

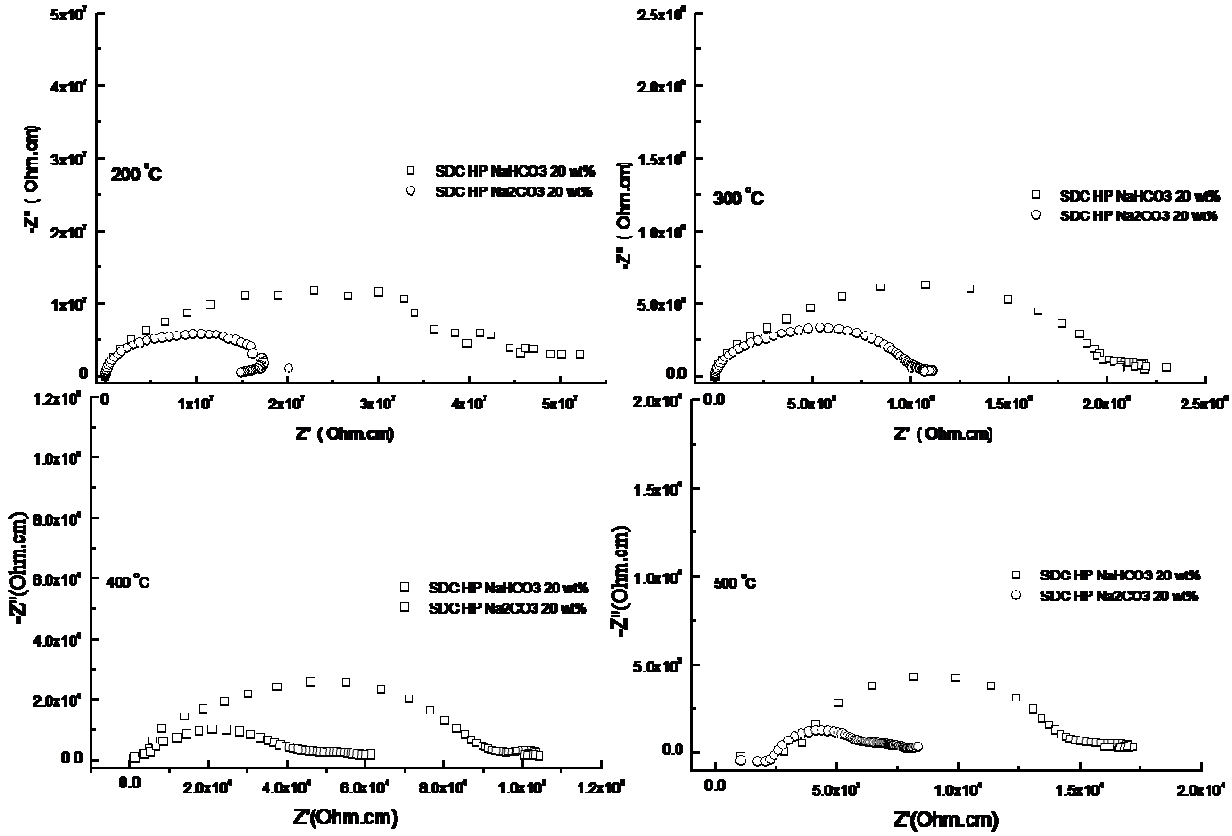

Figure 3.31. Nyquist plots of SDC (HP) Na_2CO_3 (squares) and SDC (HP) $NaHCO_3$ (circles) composites at 20 wt% concentration. The measurements were taken in air atmosphere at temperatures from 200-500 °C. The pellets were heat-treated at 700 °C.

3.8 Effect of (Na_2CO_3/Li_2CO_3) on SDC Composite

The effect of using a different carbonate salt composition was also investigated as the part of carbonate effect. In this part, Li_2CO_3/Na_2CO_3 (50:50 by wt%) mixture was used as the carbonate salt to from $LiNaCO_3$ salt. Cross sectional-SEM images of (SDC N20) $LiNaCO_3$ 20 wt% pellet were presented in Figure 3.32 (a) and (b) at 150 K and 200 K magnification, respectively. The Figure 3.32 (a) was measured under the 15 kev and Figure 3.32 (b) was measured under the 5 keV. When the electron beam energy was increased, the featureless region begins to show underneath SDC particles. Cross sectional-SEM images of the (SDC

HP) $LiNaCO_3$ 20 wt% pellet were presented in Figure 3.32 (c) and (d) at 70 K and 200 K magnification, respectively. Both composite morphologies reveal that the two phases homogeneously distributed.

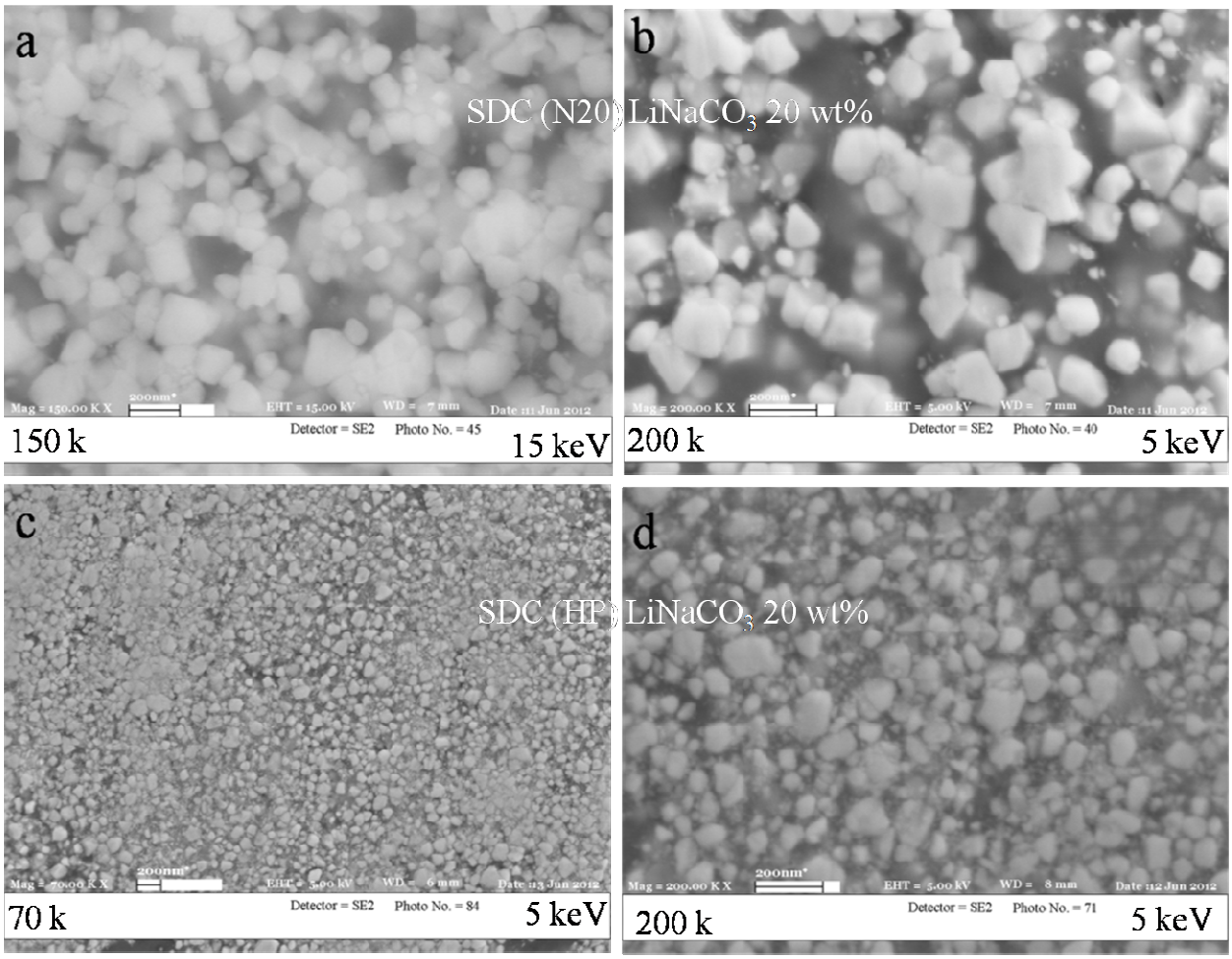

Figure 3.32. Cross sectional-SEM images of the (SDC N20) $LiNaCO_3$ 20 wt% pellet (a) at 150 K magnification and (b) at 200 K magnification; Cross sectional-SEM images of the (SDC HP) $LiNaCO_3$ 20 wt% pellet (c) at 70 K magnification and (d) at 200 K magnification. The pellets were heat-treated at 700 °C.

The thermal response of the sintered pellet composite prepared with $LiNaCO_3$ as its matrix was analyzed using differential thermal analysis (DTA/TGA) system. In Figure 3.33, the STA thermograph of the SDC (HP) $LiNaCO_3$ 20 wt% composite pellet showed a melting

transition at 492 °C which corresponded to the melting temperature of Li_2CO_3. In addition, the STA spectrum revealed a small endothermic peak at the temperature ~840 °C, which corresponded to the temperature where the decomposition of Na_2CO_3 started.

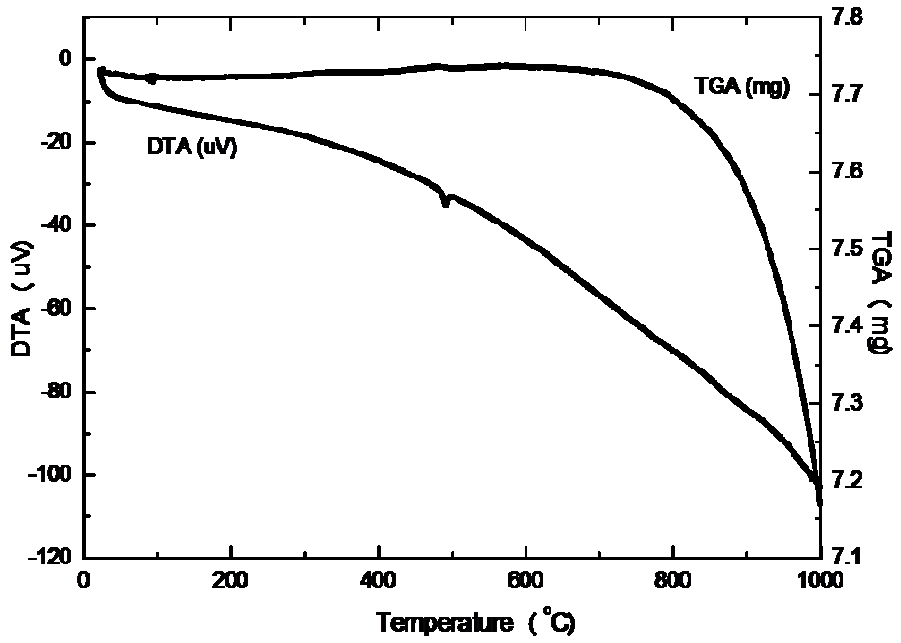

Figure 3.33 DTA/TGA spectra of the SDC (HP) $LiNaCO_3$ 20 wt% pellet. The pellet was sintered at 700 °C for 1 hour.

Figure 3.34 presents a room temperature Nyquist plot of the SDC (HP) composite with 20 wt% of Na_2CO_3 and $LiNaCO_3$. Impedances of the composites with same amount but different types of carbonate matrix phase (Na_2CO_3 versus $LiNaCO_3$) produced very different impedance spectra in terms of resistivity values. For instance, at room temperature, composites with Na_2CO_3 resulted one semi-circle with the resistivity values of 1.8×10^5 (Ω.cm) and one spike. On the other hand, the composite with $LiNaCO_3$ produced a much higher impedance resistivity value around 2.1×10^7.

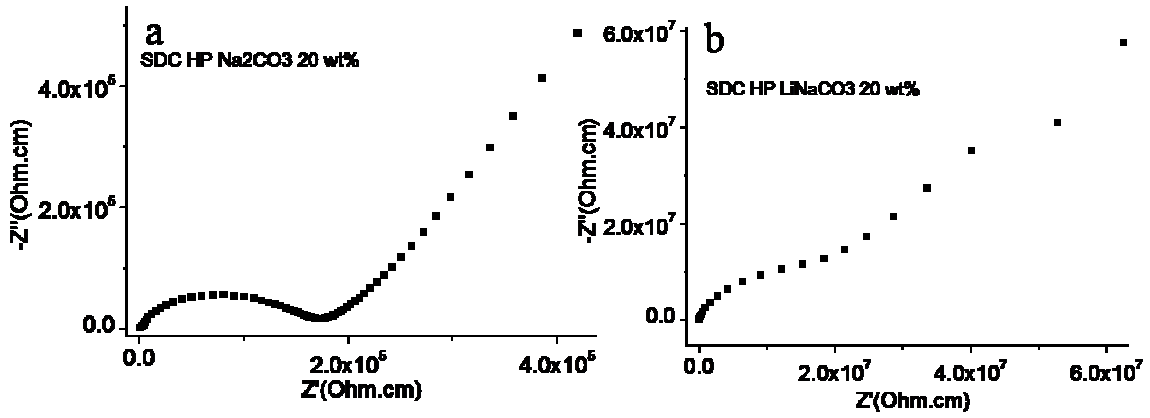

Figure 3.34. Nyquist plots of SDC (HP) Na_2CO_3 (a) and SDC (HP) $LiNaCO_3$ (b) composites with 20 wt% concentration. The measurements were taken in air atmosphere at room temperatures. All composite pellets were heat-treated at 700 ^oC for 1 hour.

Figure 3.34 further shows a Nyquist plot of SDC (HP) composite with 20 wt% of Na_2CO_3 and $LiNaCO_3$. For all measured temperatures, i.e. between 200 °C and 500 °C, the impedance measurements of the composites with same amount of either Na_2CO_3 or Li-Na-carbonate gave very different values in terms of resistivity (Ω.cm). For instance, at 200 °C, composites with Na_2CO_3 resulted in an impedance value around $2.3x10^7$ while the composite with mixed carbonate salts produced an impedance resistivity value (Ω.cm) around $1.6x10^8$ (Ω.cm). Similarly, at 300 °C, composites with Na_2CO_3 resulted in an impedance resistivity (Ω.cm) value of $1.1x10^6$ (Ω.cm) while the composite with mixed-CO_3 produce impedance resistivity (Ω.cm) values is around $4.3x10^6$ (Ω.cm). When the temperature was further increased to 400 °C, composites with Na_2CO_3 resulted in impedance values is $4.8x10^4$ (Ω.cm) while the composite with $LiNaCO_3$ produce impedance values is around $2.1x10^5$ (Ω.cm). At 500 °C, the composite with Na_2CO_3 had half the resistance value of the composite with the mixed carbonate salts.

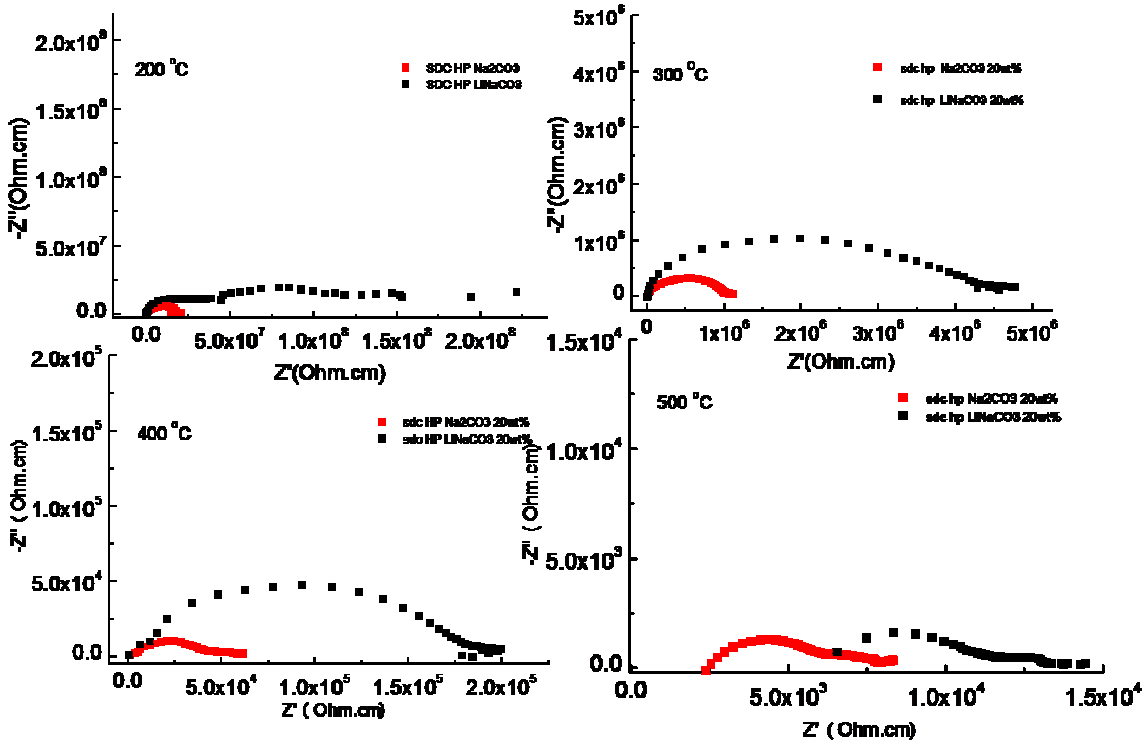

Figure 3.35. Nyquist plots of SDC (HP) Na_2CO_3 (red) and SDC (HP) $LiNaCO_3$ (black) composites at 20 wt% concentration. The measurements were taken in air atmosphere at temperatures from 200 °C -500 °C. All composite pellets were heat-treated at 700 °C for 1 hour.

3.9. Percolation of the Oxide-Matrix Interface: Phase distribution and Phase Connectivity

A design of experiments was performed to determine optimal set of parameters for Na_2CO_3 concentration for an effective nano-composite of the ceria based Na_2CO_3 nano-composite. The aim of the design of experiment was to determine the optimum carbonate to oxide particle concentration to obtain reproducibly the highest ionic conductivity.

Possible reactions mechanism and phase distribution of composite samples were monitored by X-ray diffraction (XRD) techniques. The composites of SDC (HP) with varied Na_2CO_3 matrix concentration of 5 wt% (weight percentage), 10 wt%, 15 wt%, 20 wt%, and 50 wt% were corresponding to the 12 vol% (volume percentage), 23 vol%, 32 vol%, 40 vo%, and 73 vol% Na_2CO_3 composites, respectively. Figure 3.36 shows XRD patterns of the composite powder heat-treated at 700 °C) with varying Na_2CO_3 content. All composite powders but 50 wt% composite revealed similar the diffraction patterns to the one from a crystalline SDC powder. However, when the Na_2CO_3 concentration was 50 wt% in SDC (HP) composite, weak diffraction peaks for carbonate was observed. When compared to the diffraction peaks of heat-treated Na_2CO_3 (in Figure 3.1), the heat-treated composite powder with Na_2CO_3 50 wt% showed distinctly narrow peaks of SDC (HP) alongside the ones belonging to the carbonate phase(s). Those extra carbonate peaks appeared at 31°, 37°, and 40° belonging to Na_2CO_3 and at 30°, 33°, and 38° belonging to $NaHCO_3$. The XRD pattern of the SDC (HP) Na_2CO_3 composite with low Na_2CO_3 concentration (below 20 wt%) showed only SDC peaks. It appeared that a major part of the Na_2CO_3 phase in the composite sample was in an X-ray amorphous form.

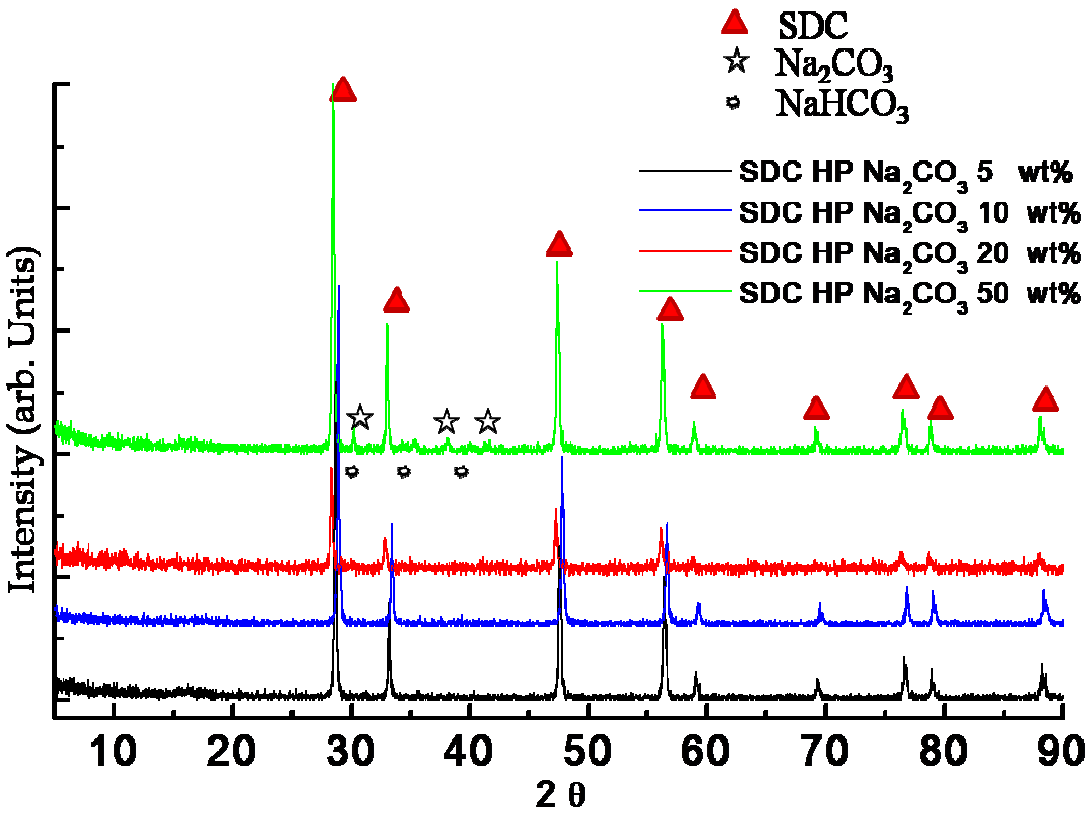

Figure 3.36. The room temperature XRD patterns of the composite with varied SDC (HP) to Na_2CO_3 concentration, such as 5 wt%, 10 wt%, 20 wt%, and 50 wt%. The XRD were performed on heat-treated powders (at 700 °C for 1 hour).

3.10. Percolation of the Oxide-Matrix Interface: Electrical Characterization of Composites with Different Carbonate Amounts

Figure 3.37 presents a typical Nyquist plot of imaginary impedance (-Z″) versus real impedance (Z′) taken from the nano-composite electrolytes. The composite's impedance spectrum includes two overlapping semi-circle arcs at high frequencies and a portion due to electrode polarization at low frequencies. The reported resistivity (Ω.cm) values were again calculated from the real axis intercepts of the semi-circular arcs in the Nyquist plots. A typical plot taken at the temperature of 300 °C was shown in Figure 3.37. It illustrated that the impedance of the composites with carbonate salts ratios up to 10 wt% decreased

monotonically. Composites with higher carbonate amount resulted in impedances that were higher than the one of the 10 wt% carbonate containing composite. For all measured temperatures, *i.e.,* between RT and 600 °C, the impedance of the composites with different carbonate to SDC ratios showed a similar behavior. Composites with 10 wt% Na_2CO_3 phase amount were the ones with the lowest impedance values, i.e. with the highest conductivities. Further analysis of the individual arcs in the impedance curves revealed that with increasing Na_2CO_3 concentration in the composite, the ratio of sizes of low frequency arc to high frequency arc changed randomly without showing any distinct trend.

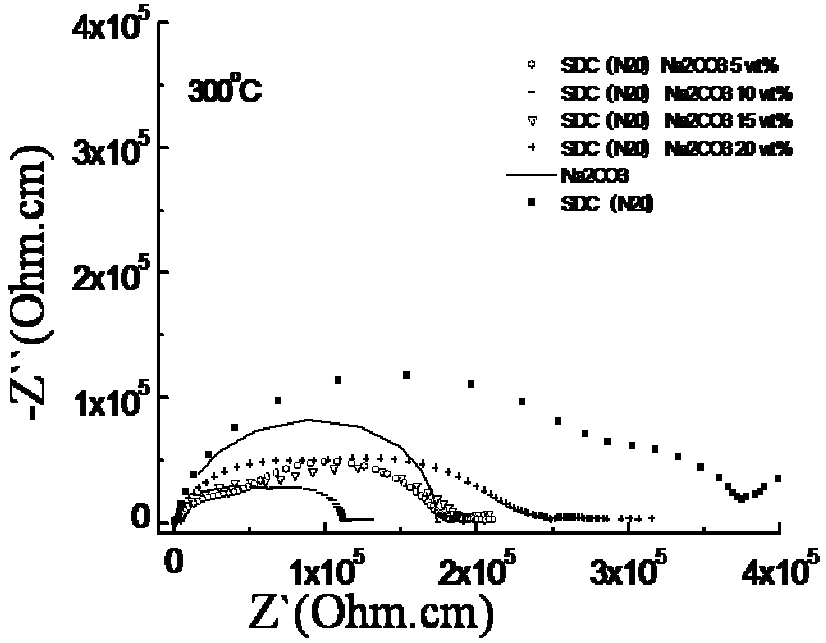

Figure 3.37. Nyquist plots of SDC (N20) Na_2CO_3 composites as a function of Na_2CO_3 concentration. The measurements were taken in air atmosphere at temperatures of 300 °C. (squares are SDC, circles are 5 wt%, dashes are10 wt%, down-triangles are 15 wt%, and crosses are 20 wt% composite, line is Na_2CO_3. All composite pellets were heat-treated at 700 ^oC for 1 hour. The SDC (N20) pellet was sintered at 1200 °C for 2 hours).

The trend in the resulted impedance values did not exactly follow the increasing carbonate amount which affected the homogeneity and relative density of the composite. Instead, it was closely linked to the connectivity of the interface and how the matrix (carbonate) and filler (oxide particles) were distributed and interconnected. The Nyquist plot of the pure SDC, Na_2CO_3, and SDC (N20)-Na_2CO_3 10 wt% composites were again plotted in Figure 3.38 for better comparison. The presented impedance data was taken at 300 °C.

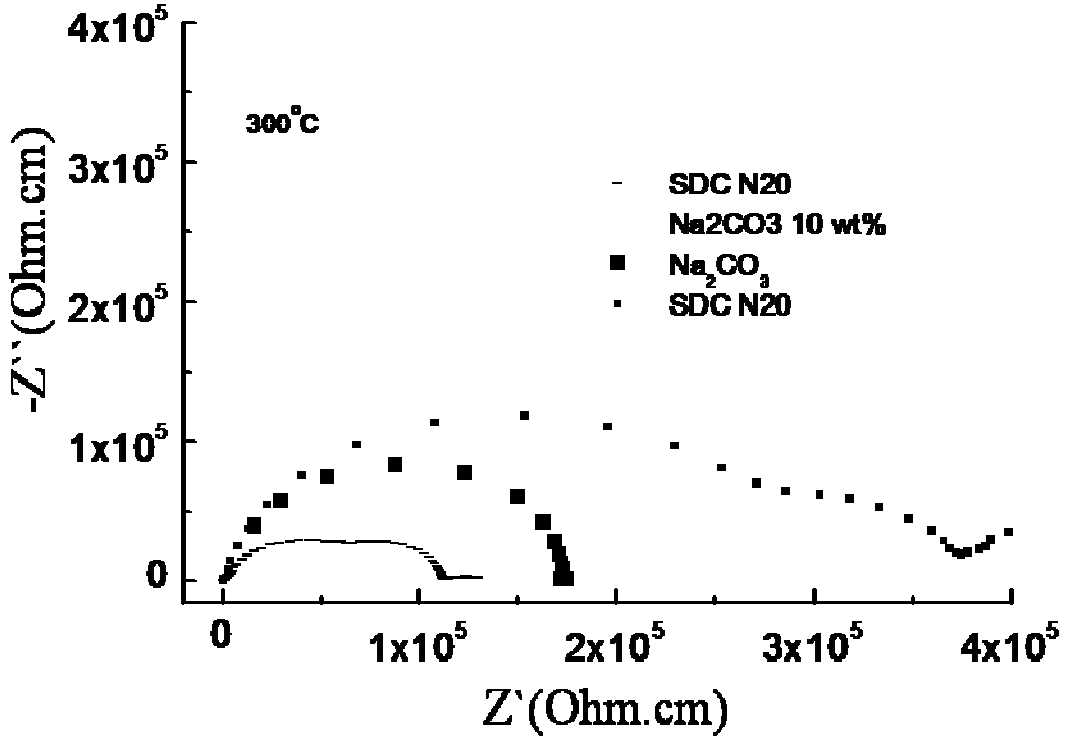

Figure 3.38. The Nyquist plot of the SDC (N20) - Na_2CO_3 10 wt% composites. The Nyquist plot of the pure SDC (N20) and Na_2CO_3 were also plotted for comparison (SDC (N20) composite was represented by bar; The Na_2CO_3 was presented by large-squares; The SDC (N20) was represented by small-square). The measurements were taken in air atmosphere at temperatures 300 °C.

The percolation behavior in the ionic conductivity is closely related how the phases are distributed in the composite microstructure. Therefore in order to correlate the percolation

behavior in electrical conductivity of the composite to their microstructures, SEM investigation of samples with varied carbonate concentrations were performed.

The SEM morphology of the composite with 1 wt%, 5 wt%, 10 wt%, 15 wt%, 20 wt%, and 50 wt% carbonates are presented in Figure 3.39. In the SEM image of the composite with 1 wt% carbonate shows only the SDC nano-particles no carbonate phase was obvious. In the micro-structure of 5 wt% composite two phases were imaged as separated and agglomerated regions. The two phases could be differentiated in the image by the difference in their contrast. The low average atomic number carbonate phase appeared as the darker, amorphous looking, and featureless regions. A homogeneous and dense morphology were observed in the composite microstructure when 10 wt% and 15 wt% carbonate concentration were used. When carbonate amount in the composite composition was further increased to 20 wt% or 50 wt% the microstructure revealed yet another problem (Figure 3.39). The SEM image of the composite containing 50 wt% Na_2CO_3 showed separated SDC particles in the Na_2CO_3 matrix. The higher average atomic number SDC particles appeared as isolated agglomerates in the lower average atomic number Na_2CO_3 matrix phase which appeared as the lower contrast regions. In this micro-structure, the amorphous carbonate regions were dominating.

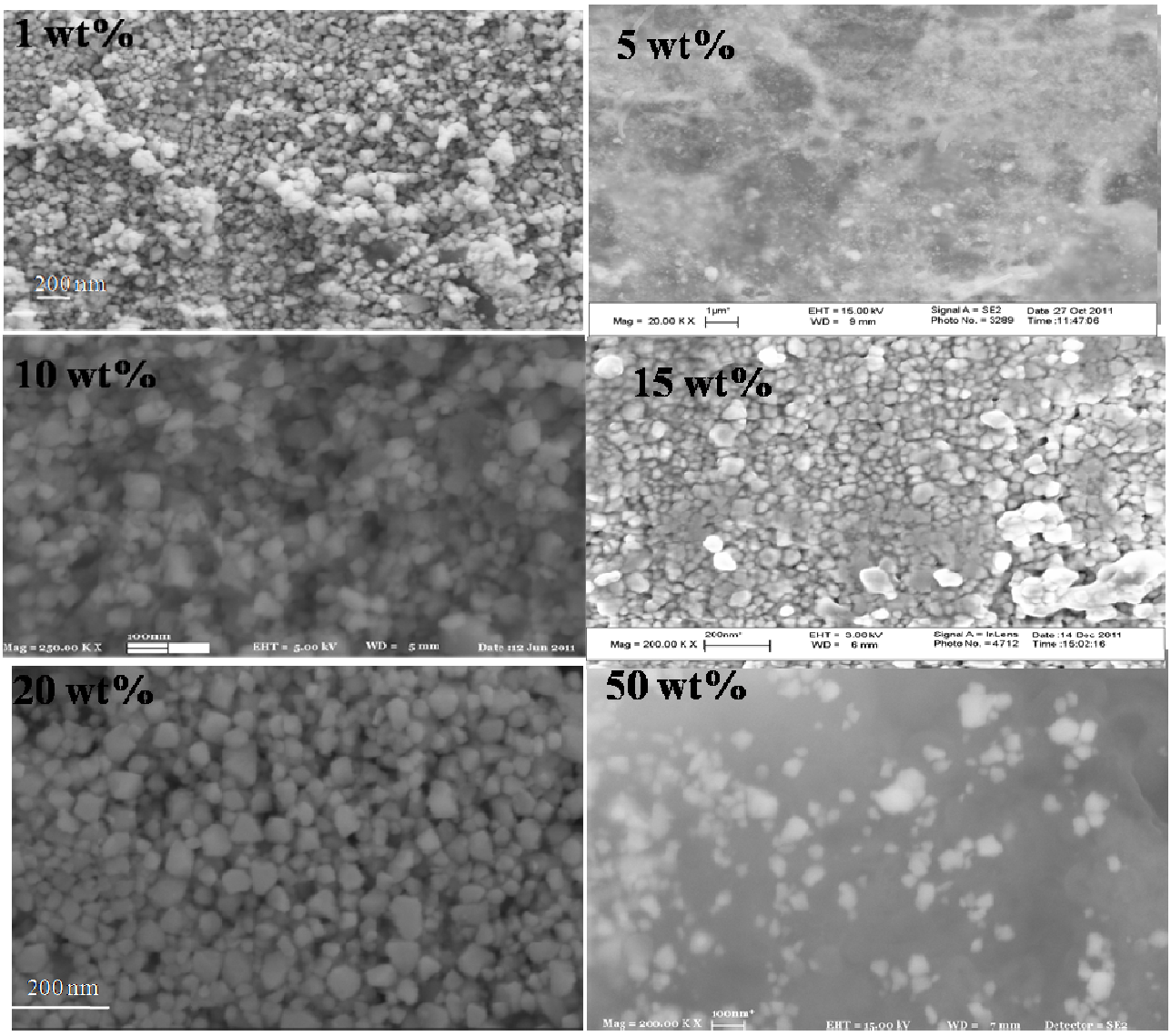

Figure 3.39. Cross Sectional SEM image of the composites that was made of SDC (N20)-Na_2CO_3 1 wt%, 5 wt%, 10 wt%, 15 wt%, 20 wt%, and 50 wt% matrix phase. The pellet was sintered at 700 ^oC for 1 hour.

EDX mapping analysis was performed in the samples as well to confirm the phase distribution in the microstructures. As an example Figure 3.40 (a) and (b) shows the SEM micro-structure and the EDX mapping of the composite with 5 wt% carbonate. The regions where sodium ions are concentrated are illustrated in red color (also circled in Figure 3.40

(a)). Regions with SDC oxide particles appeared as the white colored areas in the EDX map (Figure 3.40 (b)).

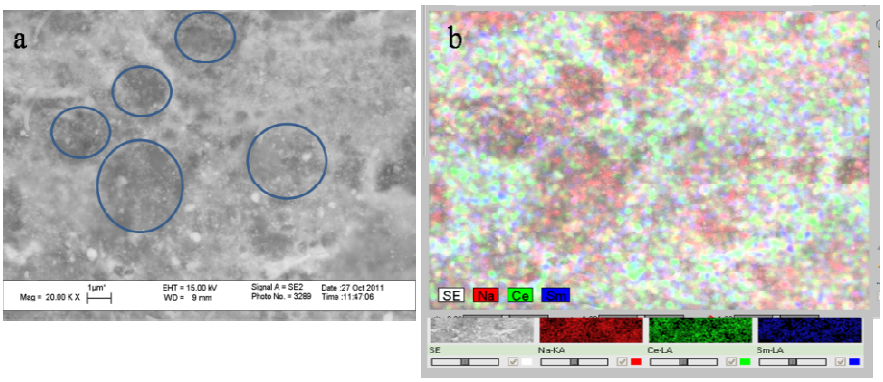

Figure 3.40. (a) Cross Sectional SEM image and (b) EDX mapping image of the composites that was made of SDC (N20) -Na_2CO_3 5 wt% matrix phase. The pellet was sintered at 700 ^oC for 1 hour.

The micro-structure imaged with SE-SEM and EDX Na-map of the composite with 20 wt% carbonate was presented in Figure 3.41. The Figure 3.41 (c) and (d) show a low-magnification image of the micro-structure of the composite under 5 keV and 15 keV, respectively. The SEM image of the composite containing 20 wt% Na_2CO_3 showed separated SDC particles in the Na_2CO_3 matrix. The SDC particles appeared as isolated agglomerates in the featureless and glassy Na_2CO_3 matrix regions. In this micro-structure, the amorphous carbonate regions were dominating. Although the microstructure of the composite imaged with SE-SEM image at high accelerating voltages did not show any carbonate phase, the EDX Na-mapping of composites with 20 wt% concentration of carbonates showed that Na element homogeneously covered SDC particles (Figure 3.41 (b)).

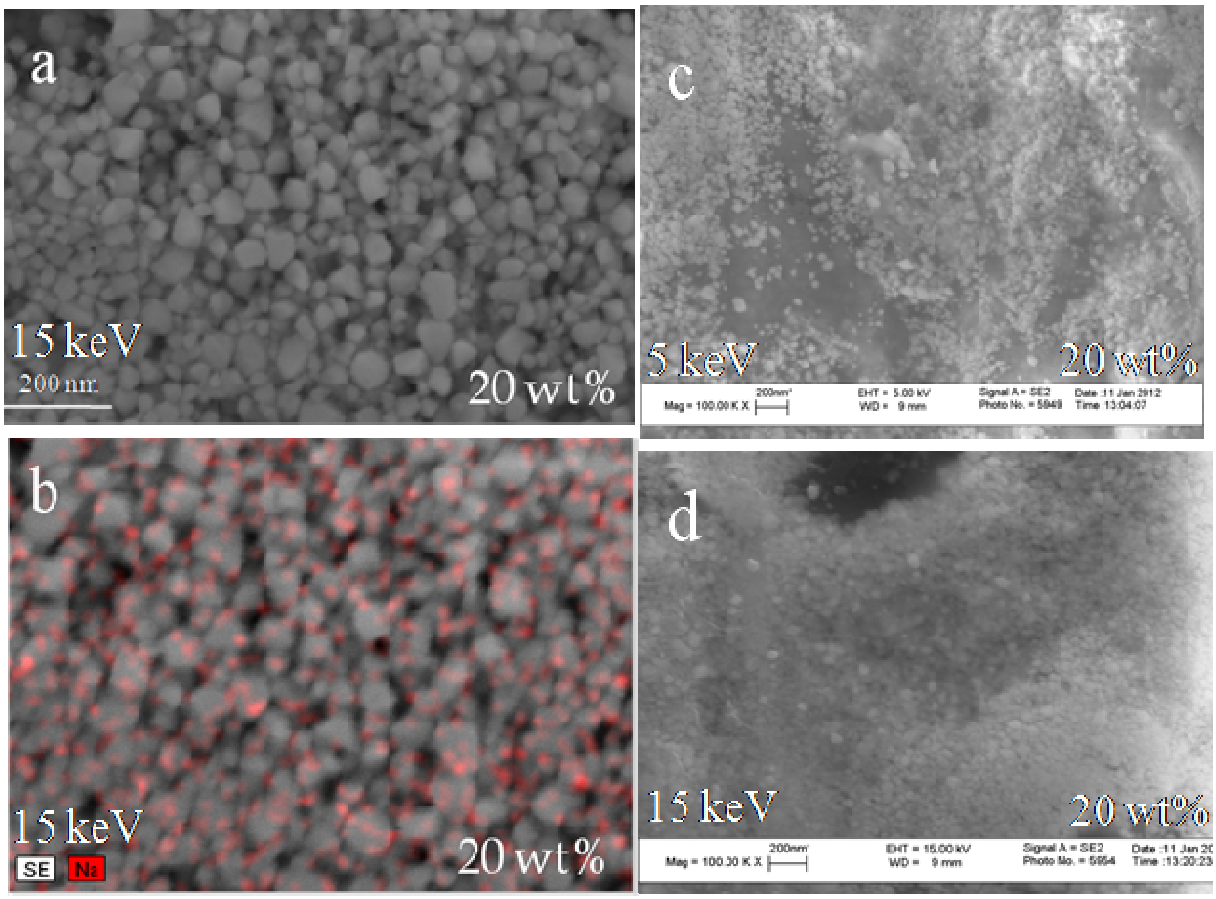

Figure 3.41. (a) SEM images and (b) EDX Na mapping image of the composites that was made of SDC (N20) -Na_2CO_3 20 wt% and SE-SEM image under (c) 5 keV and (d) 15 keV of the composites that was made of SDC (N20) -Na_2CO_3 20 wt% matrix phase. The pellet was sintered at 700 ^oC for 1 hour.

Figure 3.42 (a) and (b) illustrate the micro-structure of the composite with 50 wt% carbonate taken with SE or in-lens detector. In both images, the high average atomic (Z) number ceria particles could easily be identified as the bright particles in the composite electrolyte samples. The surrounding matrix was made up of the amorphous carbonate phase.

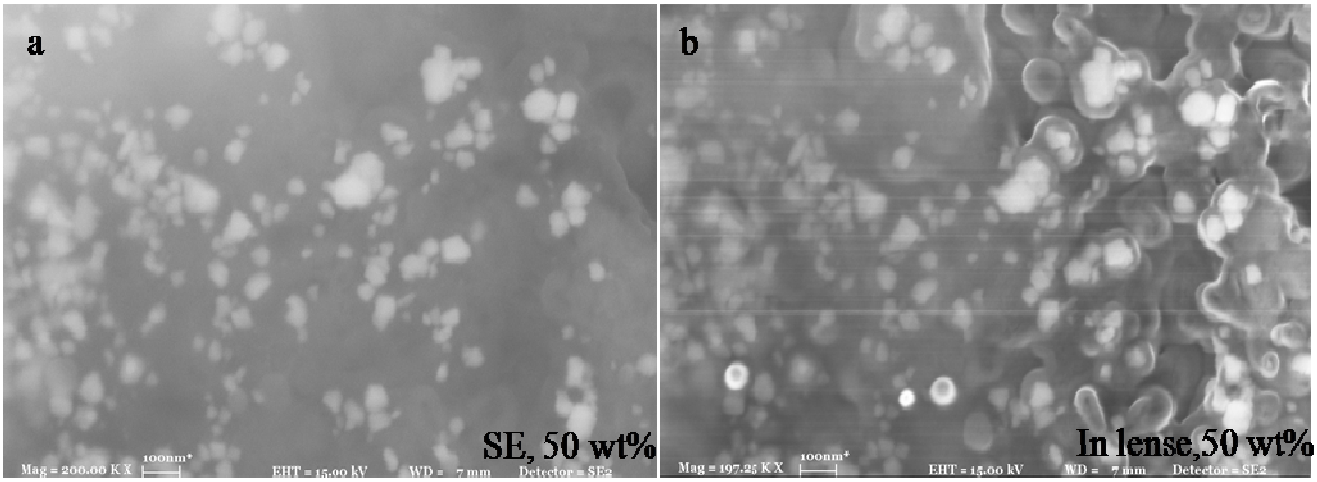

Figure 3.42. (a) SE-SEM image and (b) Inlens-SEM image of the composites that was made of SDC (N20) -Na_2CO_3 50 wt% matrix phase. The pellet was sintered at 700 ^oC for 1 hour.

Figure 3.43 presents the relationship between composite conductivity and the amount of the carbonate in the composite at 400 °C. The composite conductivity increased with increasing Na_2CO_3 amount until 10 wt%. However, a further increase of the Na_2CO_3 concentration beyond 10 wt% leads to a drop in the conductivity.

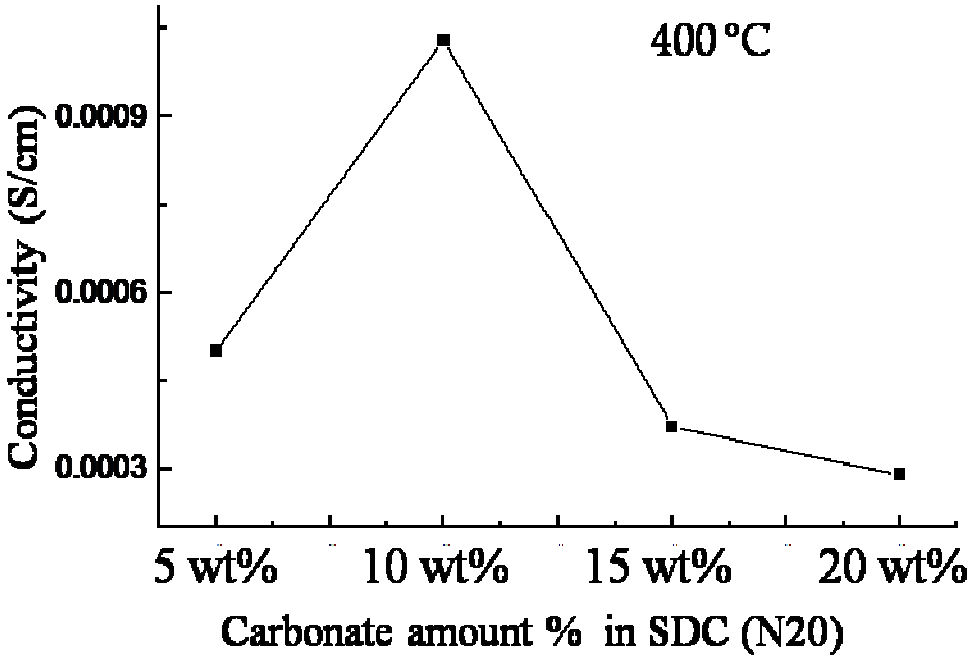

Figure 3.43. The composite conductivity versus carbonate amount graph. The composites have varied ratios of SDC (N20) to Na_2CO_3. The plots were measured at the temperature 400 °C. Composite pellets were heat-treated at 700 ^oC for 1 hour.

3.11. The Design of Interface Amount by Controlling Particle Specific Surface Area

The aim of designing the composite microstructure is to control the amount of interfaces and their connectivity in three dimensions. The important parameter in the design is the fact that specific interface area (SSA) can easily be manipulated by the fineness of the particles*, i.e.*, particle sizes. In this design of experiment, the inverse relationship between the average particle size and average SSA for ceria particles of varied size distributions was used. Thus, the amount of interfaces between the carbonate matrix and the SDC oxide particles were manipulated.

In this part of the study, the sodium carbonate to SDC ratio was fixed at 10wt%. The amounts of SSA in the composite samples were varied by mixing calculated amounts of nanometer sized SDC (N20) powders and micrometer sized SDC (HP) powders. Figure 3.44 shows the microstructures of composites containing 10 wt% Na_2CO_3 with different SSA amounts, as viewed in cross-section in the SEM. The image revealed that amorphous Na_2CO_3 covered SDC particle surfaces uniformly and constituted the matrix phase in the composite micro-structure. The lower average atomic number Na_2CO_3 matrix phase (transparent dark contrast regions) and the higher average atomic numbered SDC particles (bright particles) can be seen in Figure 3.44 (140 SSA). Na_2CO_3 also appeared to have served as the glue for the oxide particles. In the microstructure, both component phases appeared to be interconnected in 3D.

The cross-section SEM images also showed that the average grain sizes in SDC composite pellets were smaller than 200 nm and the relative density was ~98%. The 203 SSA composite micro-structures illustrated a homogeneously distributed particle size as expected since it contained only SDC (N20) powders. On the other hand, the composite micro-structures with mixed SDC (N20) and SDC (HP) powders showed bimodal particle size distribution.

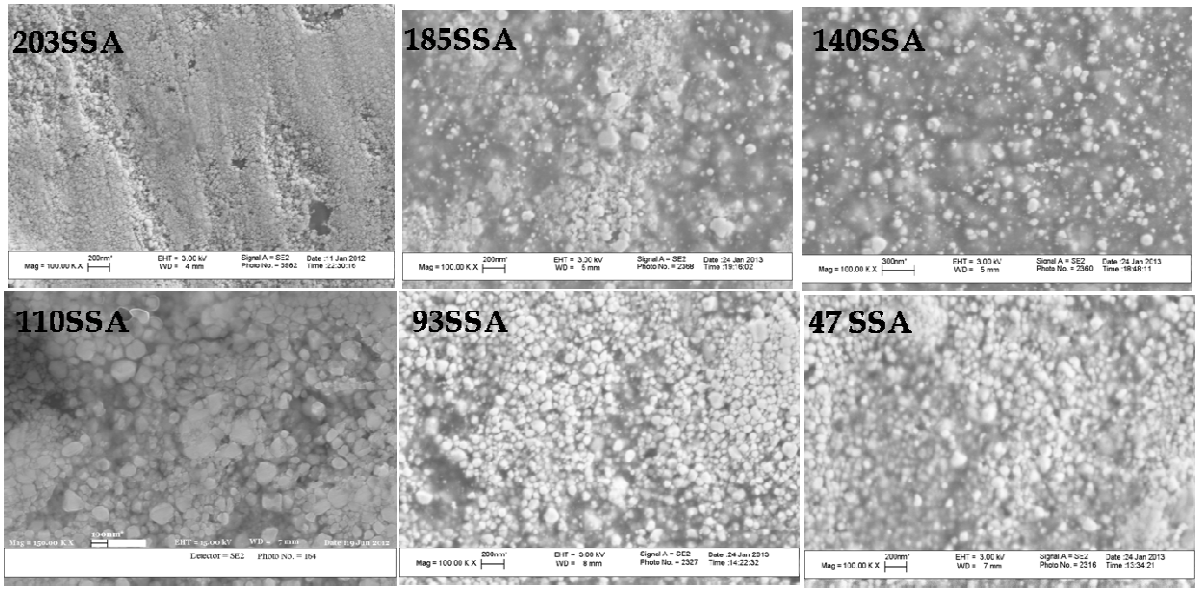

Figure 3.44. Cross Sectional-SEM images of the composites that were made of SDC (HP and N20). Composite contained 10 wt% Na_2CO_3 matrix phase and sintered at 700 ^oC for 1 hour.

Figure 3.45 illustrates two sets of representative Nyquist-type plots and imaginary impedance versus frequency plots measured at 350 °C and 450 °C, respectively. The plots illustrate nicely how the electrical properties of the composites changed for different SSA amount. Al samples had exactly the same phase amounts. In the Nyquist plots obtained from the nano-composite electrolytes there were usually two distinct semicircular impedance arcs. The observed arcs were referred to simply as low frequency or high frequency arcs without

assigning them to any specific micro-structural feature. In the nano-composite, it should be noted that there are at least two chemically distinct components with different electrical properties, even without assuming any impedance features stemming from interfaces or grain boundaries within or in between them. The values reported for the conductivity ($S.cm^{-1}$) were derived from the low frequency and high frequency intercepts of both semi-circular arcs in the Nyquist-type plots. At relatively higher temperatures, such as 350 °C, the electrode polarization effect dominated the very low frequency (<10 Hz) part of the spectra [23] as seen in Figure 3.45. In the plots, low amplitude broad arcs at frequencies below 10 Hz confirm the existence of the electrode polarization in this frequency region [23] (Figure 3.45 (b) and (d)). At all measured temperature ranges, impedance curves shrunk in amplitude with the increasing SSA of the composites indicating higher conductivity values for composite with higher interface areas.

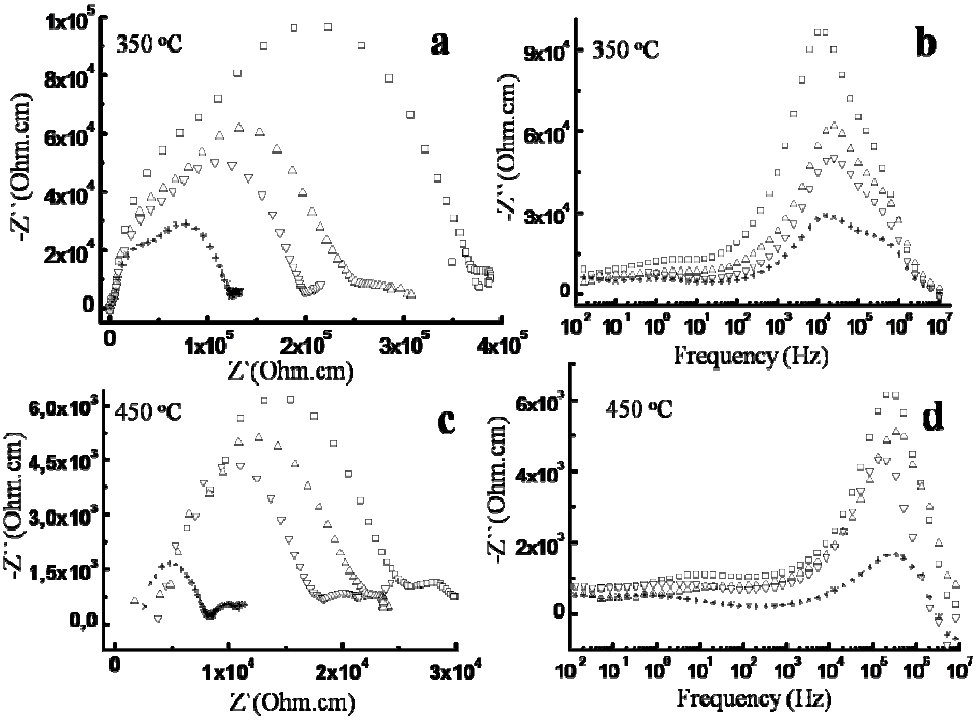

Figure 3.45. Nyquist spectra and imaginary impedance (-Z′) versus frequency plot of the 10 wt% of Na_2CO_3 composites with different SSA of SDC powders. All measurements were taken in air atmosphere at temperatures between 350 °C and 450 °C. Composite pellets were sintered at 700 ^oC for 1hour. (square 47 $m^2.g^{-1}$, up-triangle 110 $m^2.g^{-1}$, down-triangle 140 $m^2.g^{-1}$, star 203 $m^2.g^{-1}$).

Figure 3.46 summarizes the variation in total ionic conductivity in the nano-composites prepared from SDC particles with varied SSA as a function of temperature. At elevated temperatures, the ionic conductivities of the composites with smallest SSA were lower than that of the composites with largest SSA. Conductivities increased monotonically with increasing SSA of SDC particles in the composite at all measured temperature ranges. At lower temperatures (up to 400 °C), the amount of interface area (SSA of SDC particles) had a stronger influence on the ionic conductivity than at temperatures above 400 °C. The composite with the highest SSA SDC powders had persistently the highest total ionic conductivity.

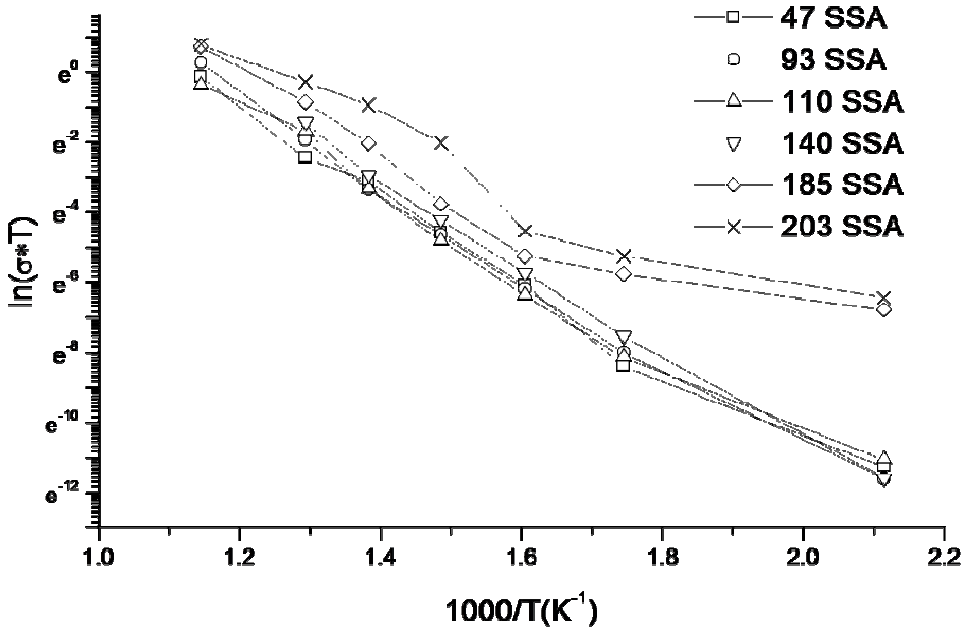

Figure 3.46. Temperature dependent conductivity of the composite SDC-Na_2CO_3 10 wt% as a function of SSA at the temperature range between 200 °C and 550 °C. (square 47 $m^2.g^{-1}$,

circle 93 $m^2.g^{-1}$, up-triangle 110 $m^2.g^{-1}$, down-triangle 140 $m^2.g^{-1}$, diamond 185 $m^2.g^{-1}$, cross is composite with SDC N20).

The thermal response of the commercial Na_2CO_3 matrix phase and the sintered composite pellet were analyzed using a simultaneous thermal analysis (STA) system. As shown in Figure 3.47, the DTA thermograph of the SDC (N20) Na_2CO_3 10 wt% composite pellet was compared with that of a heat-treated pure Na_2CO_3 pellet. The DTA spectrum of the SDC (N20)-Na_2CO_3 10 wt% composite pellet revealed a small endothermic peak at the temperature ~840 °C, which corresponded to the melting temperature of Na_2CO_3. The DTA curve of the heat-treated Na_2CO_3 pellet revealed the melting of the Na_2CO_3 over the same temperature range (shown in Figure 3.47 for better comparison).

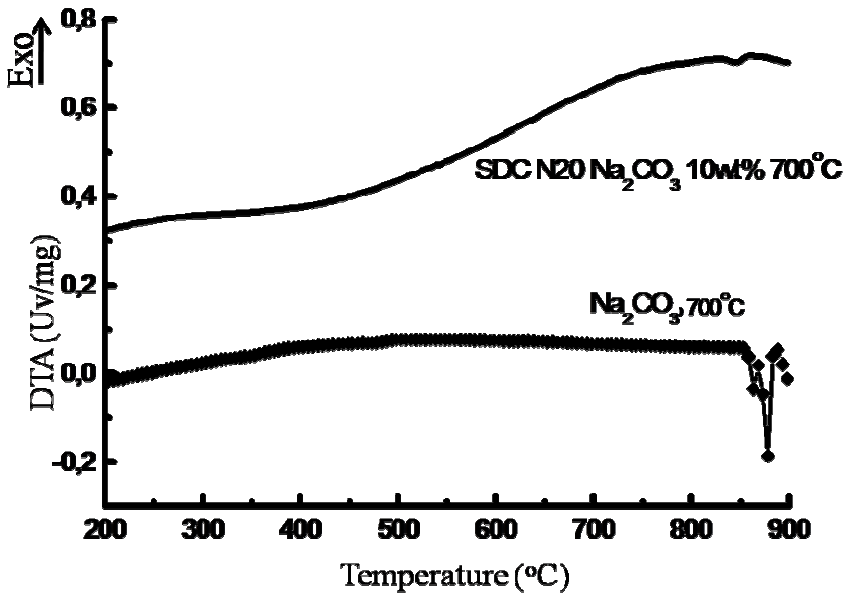

Figure 3.47. DTA spectra of the SDC (N20) Na_2CO_3 10 wt% composite and Na_2CO_3. Pellets heat-treated at 700 °C for 1 hour.

3.12. HR-TEM Studies of Composite Electrolytes

The first TEM specimen was prepared as a pin-form structure with the help of a FIB. In order to collect micro-structural information from the nano-composite, a thin TEM specimen was prepared from a heat treated pellet. Pin-formed sample milled by a FIB had certain advantages. TEM tomography could be performed on such pin-shaped composites to gain knowledge of 3-dimensional (3D) connectivity of both phases. This extremely thin needle helped us avoid projection problems during tilt series [67]. The uniformity of pin-form geometry provides detailed morphological and chemical information in 3D while it is possible to acquire 3D data for distribution of porosity and composition at the nano-scale. In this study, we used the pin-formed sample to reveal the alterations in the morphology and phase distribution of the specimen that was exposed to atmospheric moisture. In addition, the stability of the carbonate layer under the electron radiation was studied. Figure 3.48 illustrates images taken from the SDC (HP) composite pin containing originally 15 wt% Na_2CO_3 in the matrix phase. Figure 3.48 (c) shows the same specimen after being exposed to e-beam in the TEM during imaging.

The SEM image in Figure 3.48 a shows the pillar cut out from the pellet shaped specimen by FIB milling. As seen in the bright field (BF) TEM image in Figure 3.48 (b) and (c), the pin-form structure consists of two layers, the amorphous looking, brighter region (carbonate phase that formed due to reactions with humidity in air) and the crystalline darker region (SDC (HP) -Na_2CO_3 composite). According to the TEM observations, it was found out that the former amorphous-looking region was very sensitive to electron beam radiation, while the dark region was quite stable against e-beam.

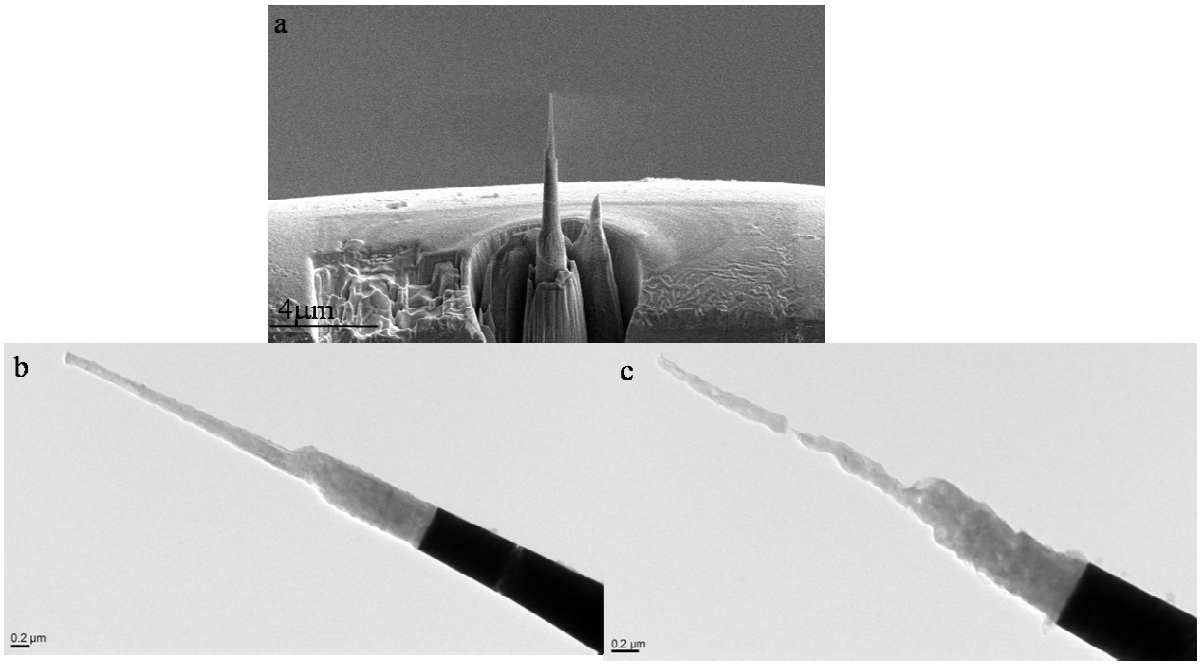

Figure 3.48. (a) The SE-SEM image of the pin-form TEM sample prepared by FIB (FEI Helios NanoLab 650 at JSI, Slovenia) and The TEM-BF images of the composites with SDC (HP) contained 15 wt% Na_2CO_3 matrix phase (JEOL JEM 2010F at JSI, Slovenia). The composite was heat-treated at 700 ^oC for 1 hour. (b) Initial pin structured and (c) after exposure to 200 KeV electron beam.

Since the carbonate layer of the pillar degraded during TEM analysis, it was hard to acquire HR-TEM images and perform further analysis on the corresponding part of the samples. Therefore, for the detailed investigation, a lamella specimen was prepared, which consisted of both layers that existed in the specimen. The TEM image in Figure 3.49 (a) showed the lamella from the same composite pellets, SDC (HP) with 15 wt% Na_2CO_3, again having a thick carbonate layer on the surface. Na_2CO_3 phase was also observed within the composite region, around the SDC (HP) crystals which were uniformly distributed. The carbonate phase could be identified as the brighter contrast regions between the particles. TEM images in Figure 3.49 (a) showed that Na_2CO_3 that reacted with atmospheric moisture was accumulated (re-precipitated) at the surface of the cross- section. The micrograph of the SDC (HP)

composite pellet showed an average thickness of this re-precipitated Na_2CO_3 layer as less than 0.5μm. In order to confirm the amorphous nature of Na_2CO_3 in TEM bright field image in Figure 3.49 (a), the diffraction patterns of two distinct layers were acquired. In addition, the STEM-HAADF micro-graph of the same region was shown in Figure 3.49 (b). In this type of imaging the dark colored region indicated the low atomic number carbonate phase and the bright colored parts were the high atomic number SDC phase. The layers above the re-precipitated carbonate layer are the protective Pt and Au layer deposited in FIB.

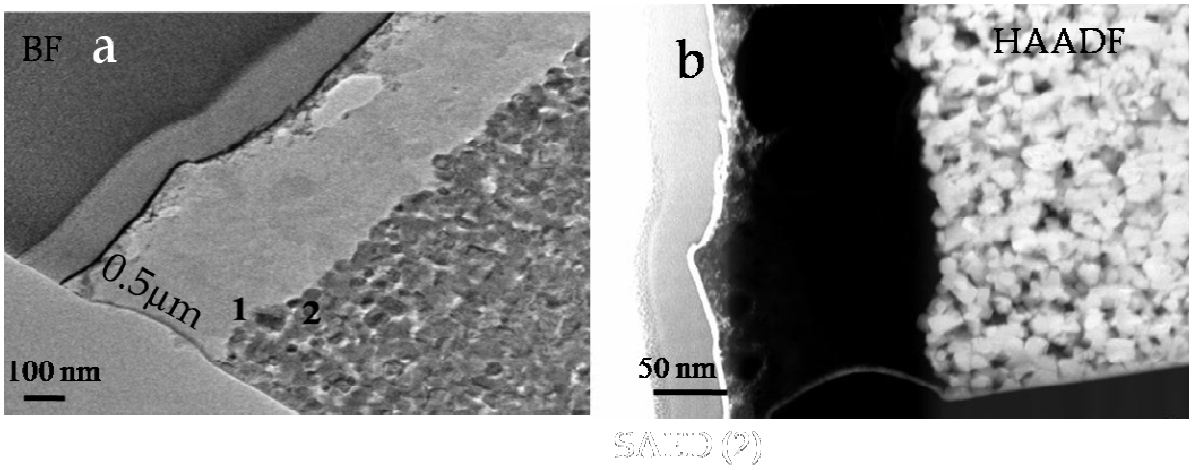

Figure 3.49 The TEM-BF (a) and STEM-HAADF (b) micrographs (JEOL JEM 2010F at JSI, Slovenia) of the composites with SDC contained 15 wt% Na_2CO_3 matrix phase prepared by FIB (FEI Helios NanoLab 650 at JSI, Slovenia). The composite was heat-treated at 700 ^oC for 1 hour.

The diffraction patterns of the upper layer (region 1, carbonate) and lower region (region 2, composite) are shown in Figure 3.50 (a) and Figure 3.50 (b) respectively. Since there were no diffraction spots visible for the region 1, *i.e.,* the carbonate layer (Figure 3.50 (a)), this region was interpreted to be in an amorphous form. Figure 3.50 (b) showed a typical spotted diffraction rings of a polycrystalline material, *i.e.,* SDC (HP) crystals. Each of the diffraction rings could be identified according to the SDC planes of (110), (200), (220), (311), (222),

(400), (331) and (420). All the peaks very well matched with the diffraction peaks of the SDC (HP) fluorite structure.

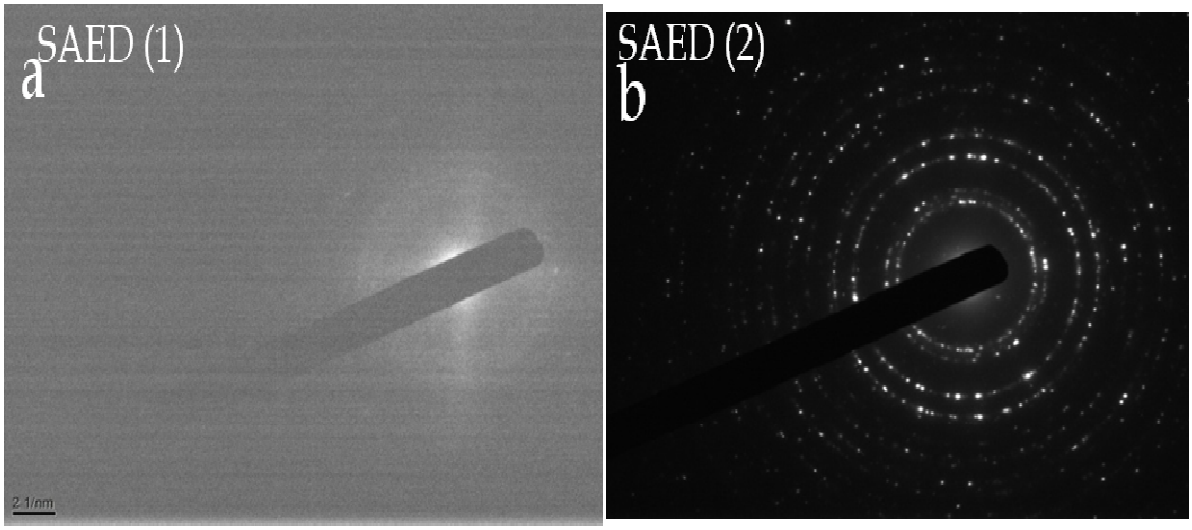

Figure 3.50. The diffraction patterns taken from region 1 (a) and region 2 (b) in the specimen prepared from) of the composites with SDC (HP) contained 15 wt% Na_2CO_3 matrix phase prepared by FIB (FEI Helios NanoLab 650 at JSI, Slovenia). The composite was heat-treated at 700 ^oC for 1 hour. Images were taken with a JEOL JEM 2010F at JSI, Slovenia.

The STA thermograms of the composites consisting of SDC (HP) and 10 wt% Na_2CO_3 and a commercial $NaHCO_3$ powder are shown in Figure 3.51. The evaporation of water around 100 ^oC and the melting of the Na_2CO_3 at 850 ^oC were observed (in Figure 3.51) which are from the composite. Figure 3.51 (b) shows STA thermograms of the commercial $NaHCO_3$. The absorbed water evaporated around 100 °C; while the monosodium carbonate decomposed right after the evaporation of water at around 150 °C. The endothermic peak at 830 °C was related to the melting of the sodium carbonate phase which was also observed in the nano-composite. The decomposition of sodium carbonate derived from commercial monosodium carbonate was delayed to above 1000 °C which was not expected.

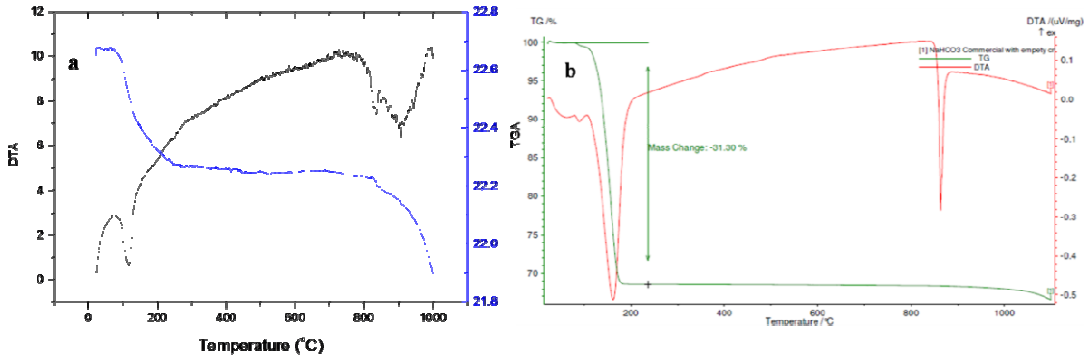

Figure 3.51. a) STA of the composites with SDC contained 15 wt% Na_2CO_3 matrix phase. The composite was heat-treated at 700 ^oC for 1 hour and b) STA of the commercial $NaHCO_3$ powder.

All micrographs in Figure 3.52 shows the micro-structure of the composite prepared as a thin TEM lamella and imaged right after FIB-preparation to avoid the artifacts that were due to reactions of the thin sample with the atmospheric moisture. The FIB-lamella had a thickness below 100 nm. The TEM-BF images were taken from the sintered composite pellets having SDC (HP) particles with 10 wt% Na_2CO_3 content. The TEM-BF images showed that the average grain size of the SDC (HP) particles was in the order of 100 nm (Figure 3.52 (d)). The images showed SDC (HP) particles (circled in Figure 3.52 (a)) embedded into the carbonate matrix surrounding them. Na_2CO_3 phase (the lighter contrast matrix) appeared to have served as the glue for the oxide particles. The characteristic lattice fringes and Moire fringes from crystalline SDC (HP) particles could also be seen. However, no lattice fringes could be observed for the Na_2CO_3 matrix. In the TEM micrographs, both component phases appeared to be interconnected in 3D. The beam damaged introduced to the matrix carbonate phase under the e-beam radiation can be observed in Figure 3.52 (a), (c), and (d).

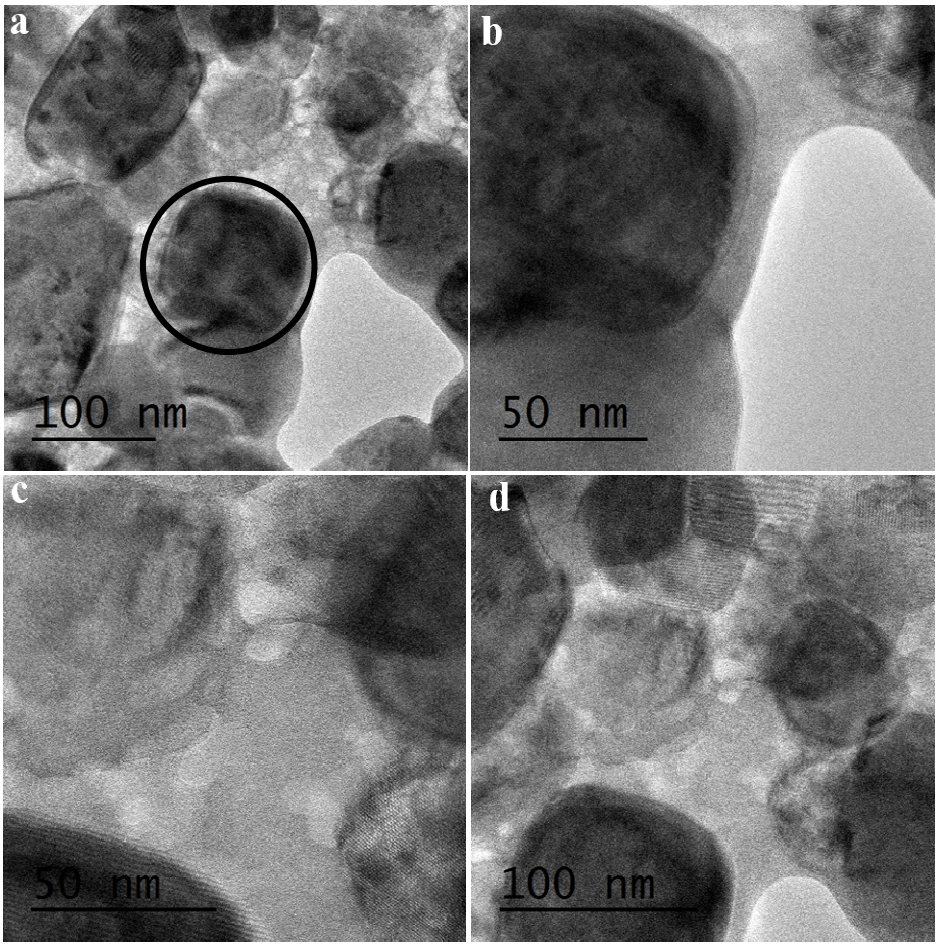

Figure 3.52. The TEM-BF images of the composite with SDC (HP) containing 10 wt% Na_2CO_3 matrix phase. The composite was heat-treated at 700 ^oC for 1 hour. (b) Higher magnification of (a). (c) Higher magnification of (b).

To image the distribution of elements in the SDC (HP) containing 10 wt% Na_2CO_3 composite, spectral elemental mapping was performed in TEM-EELS mode (in Figure 3.53). The TEM-BF image in Figure 3.53 (d) (from a similar but different region) revealed that the average grain sizes in the SDC (HP) composite pellet were in the order of 24 nm to 200 nm. We need to describe what the reader should pay attention to in these figures.

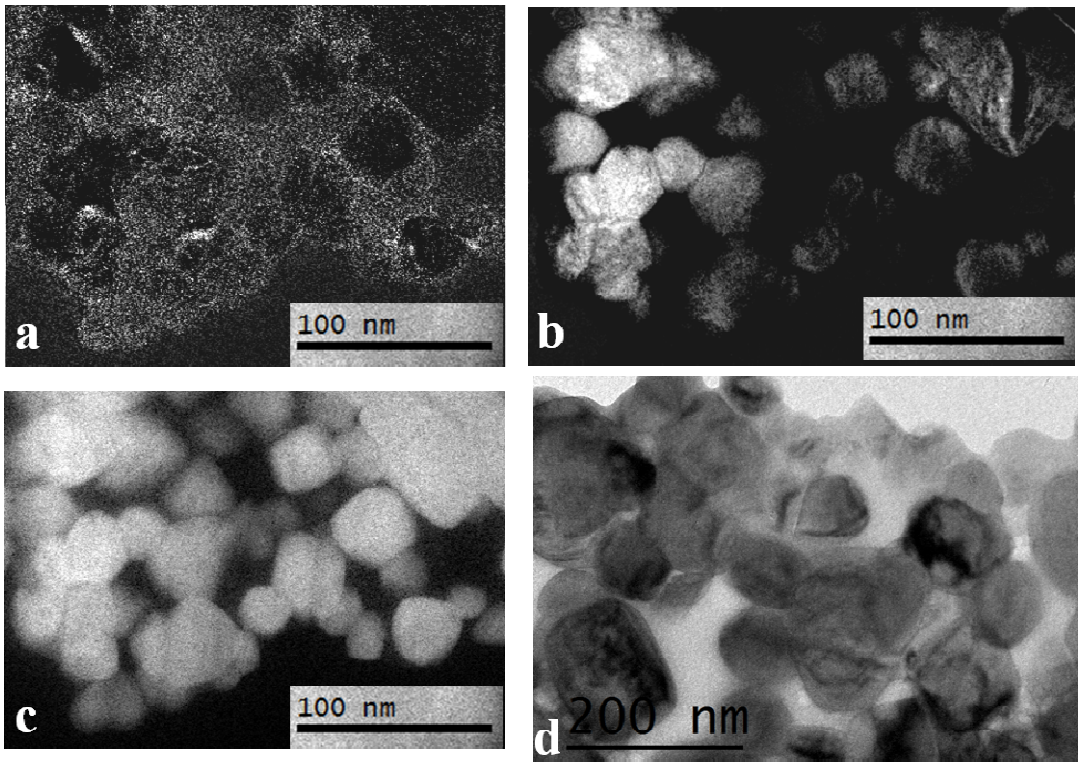

Figure 3.53. The TEM elemental maps of the composites with SDC (HP) containing 10 wt% Na_2CO_3 matrix phase. The composite was heat-treated at 700 ^oC for 1 hour. The examined elements are a) Carbon-K_α edge mapping, b) Na-L edge mapping; (c) Ce-M edge mapping, d) TEM image of the sample which is not exactly the same region as the mapped area.

In order to eliminate the possibility of incorporation (dissolution of Na in the cerium oxide bulk) of Na element in the SDC particle, both EDX and EELS analysis were performed. Those analyses were performed on the washed composite powder which was made of SDC (HP) composite with 10 wt% Na_2CO_3. The composite powder was heat-treated at 700 ^oC for 1 hour. The composite powders were intentionally washed with deionized-water to remove the possible surface adsorbed sodium and carbonate phases. Sodium carbonate is highly soluble in cold water. The measured EDX in Figure 5.54 shows that no detectable amount of Na was incorporated in the SDC particles.

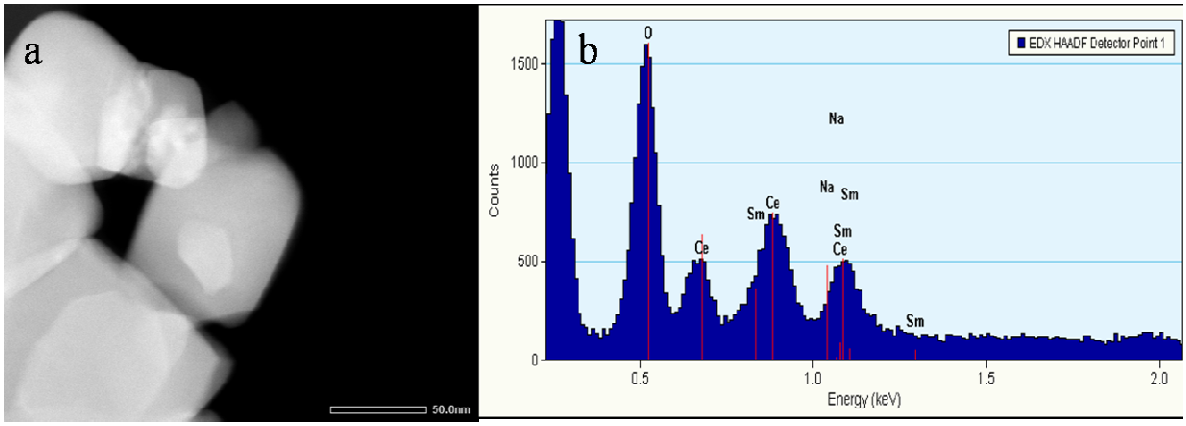

Figure 3.54. The TEM (a) and EDX elemental maps (b) of the composites (after washed) with SDC (HP) contained 10 wt% Na_2CO_3 matrix phase. The composite powder was heat-treated at 700 ^oC for 1 hour. The composite powder was washed with water. The examined elements are Carbon-K_α edge mapping, Na-L edge mapping and Ce-M edge mapping.

3.13. Oxide Types in the Composite Electrolytes

In this part of the study, we have investigated the electrical properties of composites with different oxide particle fillings instead of samarium doped cerium oxide. Different oxide particles with corresponding surface charges were embedded into at constant 20 wt% Na_2CO_3 matrix to fabricate the composite electrolytes.

3.13.1. Effect of the Surface Charge on the Conductivity

The surface charges of the different oxide powders were determined by measuring the iso-electric points of the suspensions with these oxide powders. Titration process of the oxide particle- water suspension was illustrated in Figure 3.55. At iso-electric point, phase separation occurred and subsequently the particle suspension formed a clear aqueous solution with the oxide particles sedimented at the bottom of the container. For example, at pH value

of 13, the color of the TiO_2 (rutile) suspension was opaque white. However, when the pH value was adjusted to 5.3, the opaque-white oxide suspension turned to a transparent-clear solution. Following similar procedure above, the iso-electric points of various oxides-water suspensions were precisely recorded by a Malvern zeta potential-auto titration instrument (Zetasizer NanoZS).

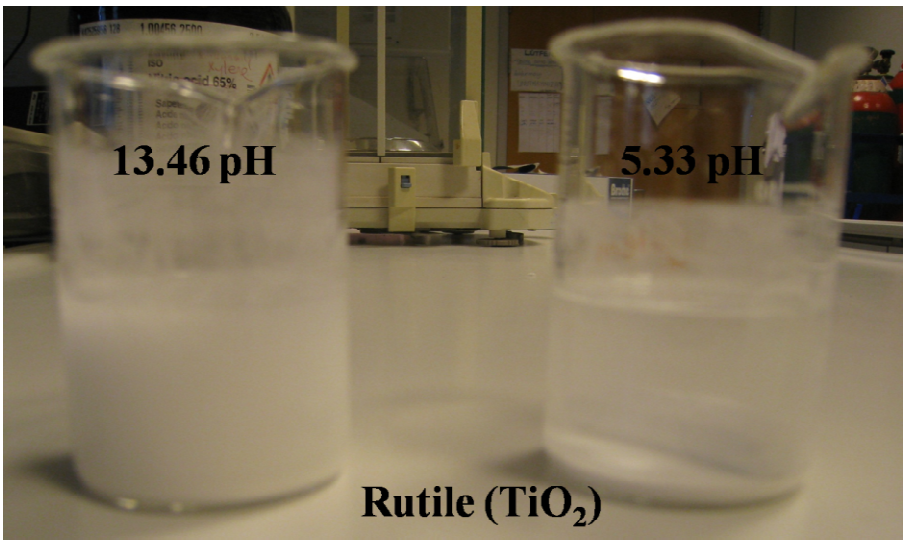

Figure 3.55. The experimental set up for illustration of auto-titration experiment.

The typical zeta potential plots of the SDC (N20) and SDC (HP) determined by auto-titration of pH were presented in Figure 3.56. The iso-electric points (zero zeta potential values) of the SDC (N20) and SDC (HP) were observed approximately at the pH values of 5.8 and 6.2, respectively.

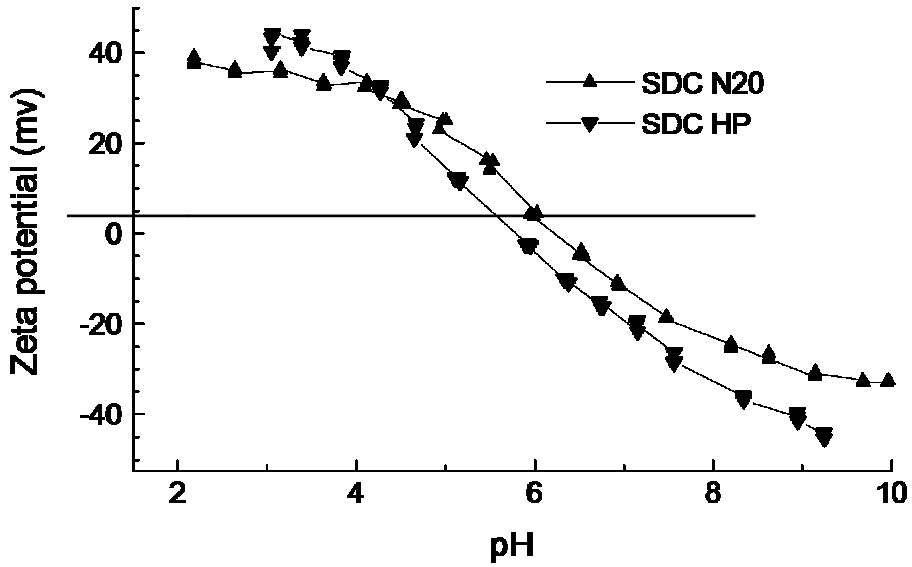

Figure 3.56. The zeta potential plots of SDC (N20 and HP) as a function of pH. The up-triangles represent SDC (N20) and down-triangles represent SDC (HP).

The iso-electrical points of the other potential candidate oxides for the composite were also measured. The Figure 3.57 shows the zeta potential plots of Al_2O_3, TiO_2, and SiO_2 as a function of pH. In the zeta potential versus pH graph, the iso-electric point of the Al_2O_3 and TiO_2 are approximately in the pH values of 8.3 and 7.1, respectively. However, for SiO_2 oxide zero iso-electric point could not observed in the experimental set up range due to the minimum pH limitation of the instruments. Thus, the literature reported iso-electric point (2.3pH) was used in our comparative study [64].

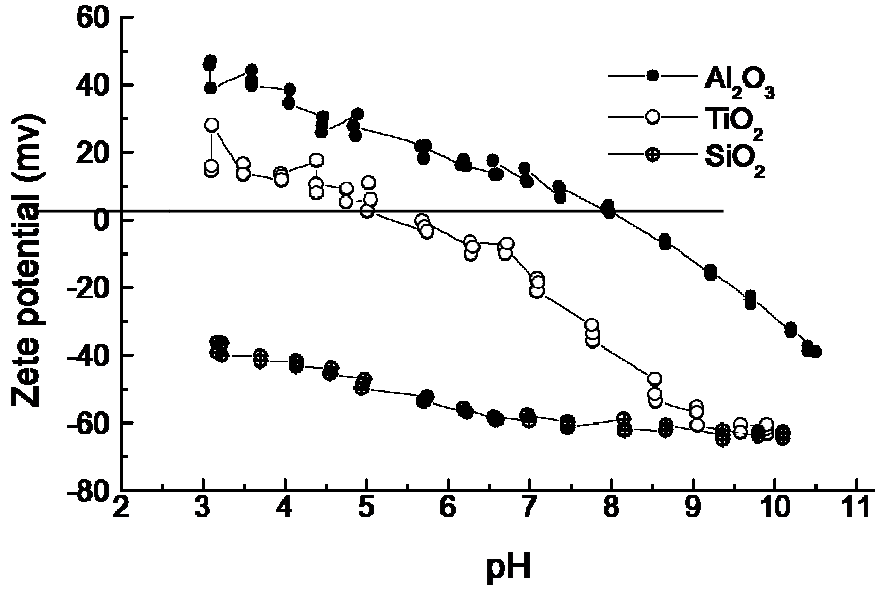

Figure 3.57. Plots of the zeta potential of Al_2O_3, TiO_2, and SiO_2 measured as a function of pH.

3.13.2. Physical Properties of Alternative Oxide Powders

All oxide powders were ball milled for 6 hours to reduce the particle sizes. SEM images of the ball milled oxide powders are presented in Figure 3.58. The SEM micro-structure revealed that all oxide powders have comparable particle sizes. For instance, SDC (HP) oxide powders showed an average grain size between 50 nm to 150 nm; whereas SDC (N20) oxide powders average grain sizes were in the region of 84 nm - 200 nm. The YSZ oxide powders average grain sizes were in the range of 66 nm - 130 nm; whereas Al_2O_3 oxide powders average grain sizes were in the region of 84 nm - 200 nm. For TiO_2 oxide powder, the average grain size was in the range of 150 nm - 300 nm; whereas LSGM oxide powders average grain sizes were in the region of 120 nm - 200 nm. The YSZ, LSGM, and SDC (N20) powders were hard agglomerates.

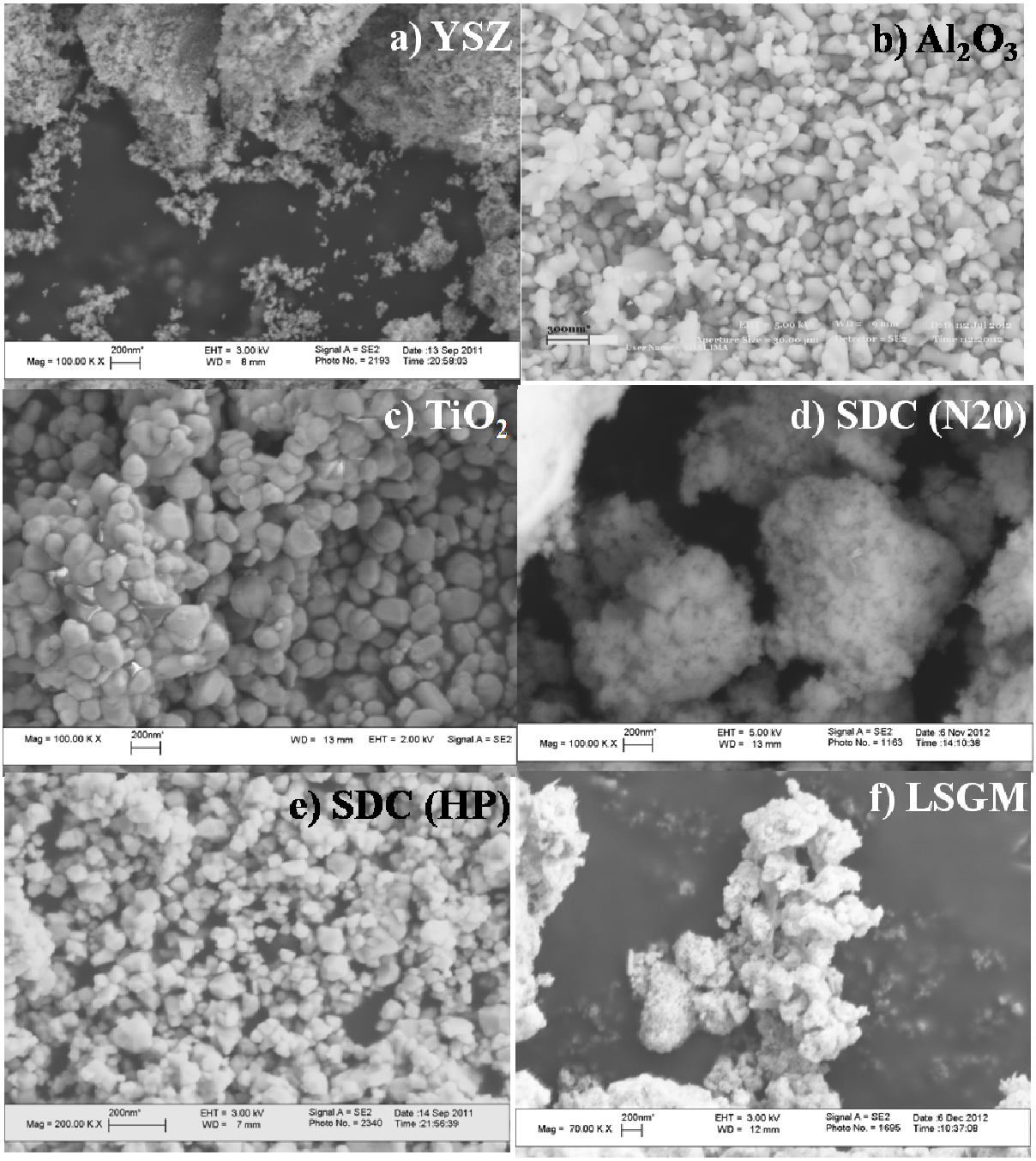

Figure 3.58. SEM images of ball-milled oxide powders (a) YSZ powder, (b) Al_2O_3 powder, (c) TiO_2 (rutile) powder, (d) SDC (N20) powder, (e) SDC (HP) powder, and (f) LSGM powder.

3.13.3. Electrical Characterization of composites with Alternative Oxide Fillers

The concentration of Na_2CO_3 in the alternative composites was fixed at 20 wt% to determine the effects of the oxide surface charge. The electrical conductivity of all the composites was evaluated with the electrochemical impedance analysis (EIS) at temperatures ranges from RT to 600 °C. The Figure 3.59 shows four representative Nyquist plots of the different oxide composites at measured temperatures between 200 °C and 500 °C in air atmosphere. The graphs illustrates imaginary impedance (-Z″) versus real impedance (Z′) spectra's of composites' impedance spectra included two overlapping semi-circle arcs at high frequencies and a portion due to electrode polarization at low frequencies (below 10 Hz). Spectra taken at 200 ^{o}C and 300 ^{o}C from different composites revealed some common features, such as similar shapes and trends for all the v different oxides. Depressed high frequency semi-circles were detected in the temperatures ranges from 400 ^{o}C to 500 ^{o}C. Furthermore, at 500 °C, the silver electrode polarization effect appears at the very low frequency end of the spectra. The single semi-circle with a negligible depression was observed in the high frequency region of the spectra at this temperature.

The electrical resistivity of the different oxide composites were listed in the Table 3.4. At 200 ^{o}C, the resistivity values (Ω.cm) of both YSZ and Al_2O_3 composites were in the order of $1x10^7$ (Ω.cm), while SDC (N20) and rutile composites resistivity values were in the order of $1x10^6$ (Ω.cm) and $1x10^8$ (Ω.cm). At 300 ^{o}C, SDC composite had the resistivity values in the order of $1x10^5$, while other composites had a resistance values in the order of $1x10^6$ (Ω.cm). At 400 ^{o}C, TiO_2 and Al_2O_3 composites had the larger resistivity values compared to resistivity of other composites. For example, composites of SDC and YSZ composites had the

resistivity values in the order of $1x10^4$ (Ω.cm), while other composite had resistivity values an order of magnitude larger at $1x10^5$ (Ω.cm).

Table 3.4. Measured electrical resistivity of composites with different oxides

Sample Temperature	Resistivity (Ω.cm)	Resistivity (Ω.cm)	Resistivity (Ω.cm)	Resistivity (Ω.cm)	Resistivity (Ω.cm)
Temperature	YSZ	Al_2O_3	SDC	TiO_2	LSGM
200 °C	$1x10^7$	$1x10^7$	$1x10^6$	$4x10^8$	$7x10^8$
300 °C	$1.8x10^6$	$1x10^6$	$1x10^5$	$8.0x10^6$	$1.5x10^7$
400 °C	$2.5x10^4$	$2x10^5$	$1x10^4$	$2.5x10^5$	$8x10^4$
500 °C	$3x10^4$	$4x10^4$	$5x10^3$	$1x10^5$	$1x10^5$

To summarize, the most-striking difference in ionic conductivities of the series of the composites was observed at 500 ^oC. For instance, the resistivity (Ω.cm) of SDC (N20) composite was about one order of magnitude smaller than the resistivity (Ω.cm) of YSZ and Al_2O_3 composites. In addition, in the measure region from 300 – 500 ^oC, SDC composite had consistently a lower resistivity value (Ω.cm) than other composites. At low frequency region of the complex curve, spikes were observed for the TiO_2 composite, which were attributed to electrode polarization.

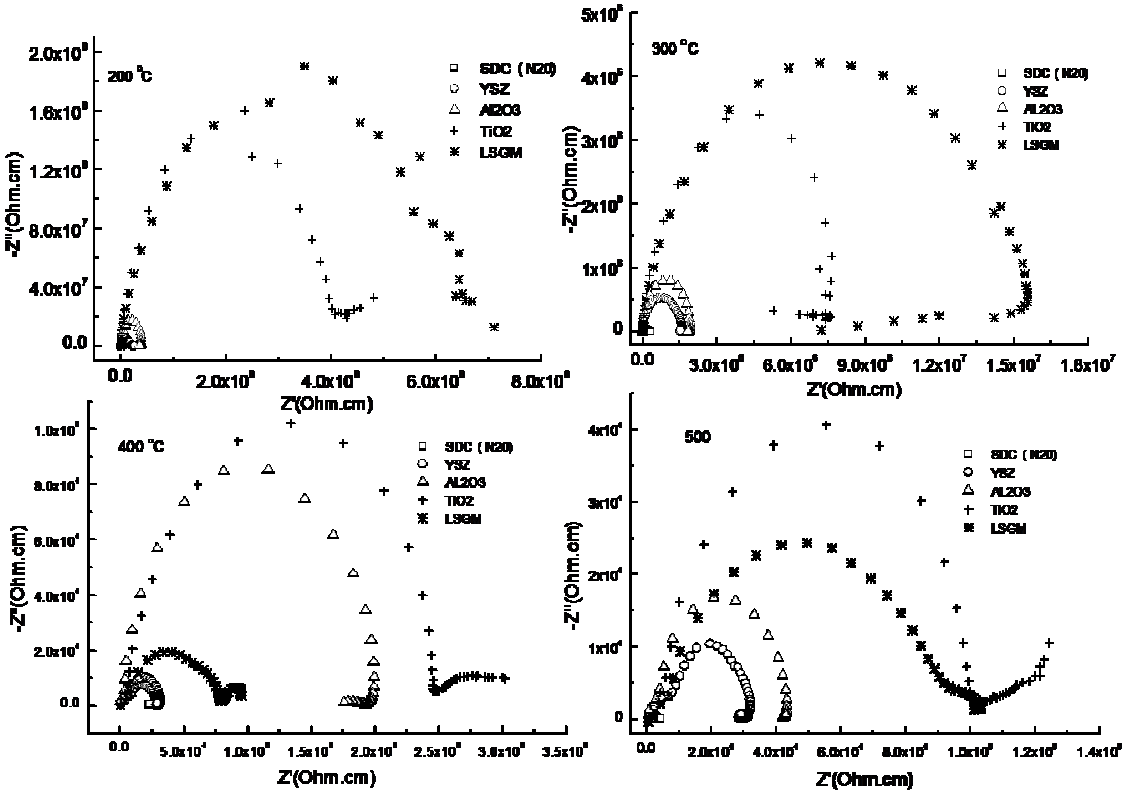

Figure 3.59. Nyquist spectra of 20 wt% of Na_2CO_3 composites with different oxides. All measurements were taken in air at the temperatures between 200 ^oC and 500 ^oC. Composite pellets were heat-treated at 700 ^oC for 1hour.(SDC was represented by squares; YSZ was represented by circles; Al_2O_3 was represented by up-triangle; TiO_2 was represented by cross; LSGM was represented by stars.)

In addition to those oxide materials, the impedance of the composite made up of SiO_2 was also measured for a comparative study. However, due to the huge difference in the resistivity values, it was not possible to plot all the impedance spectra of all the composites including the one with silica particles in one graph. Therefore, the 500 °C Nyquist plot of the SiO_2 composite with 20 wt% Na_2CO_3 was reported alone in Figure 3.60.

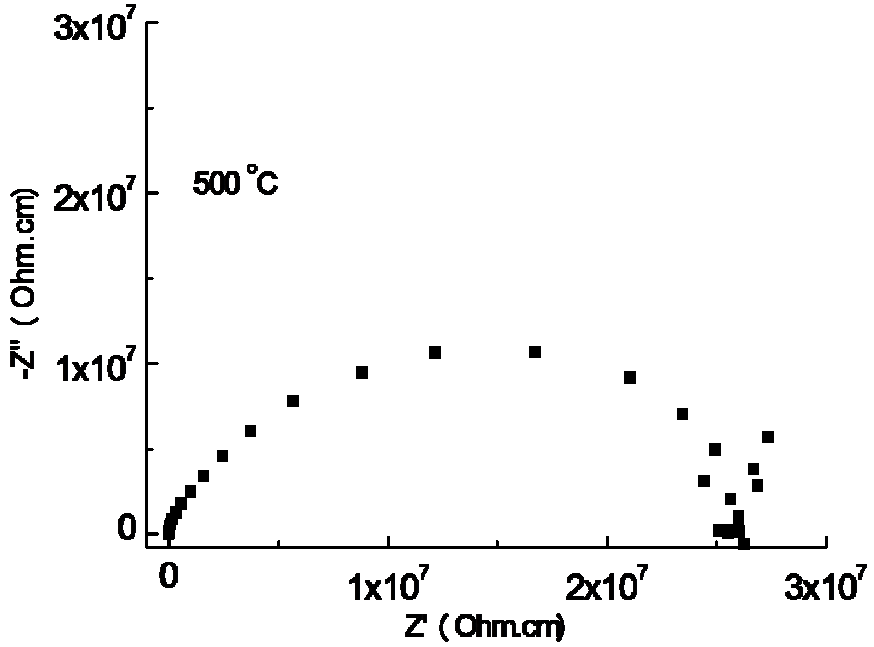

Figure 3.60. Nyquist spectra of the composite which was made of SiO_2 -Na_2CO_3 20 wt%. The measurement was taken in air at the temperatures 500 ^oC. Composite pellets were heat-treated at 700 ^oC for 1hour.

The 600 °C Nyquist plots of the composites with a series of different oxides were displayed in Figure 3.61. Composite electrolyte which was made of SDC (N20) with 20 wt% Na_2CO_3 had a highest conductivity compared to other composites at 600 °C.

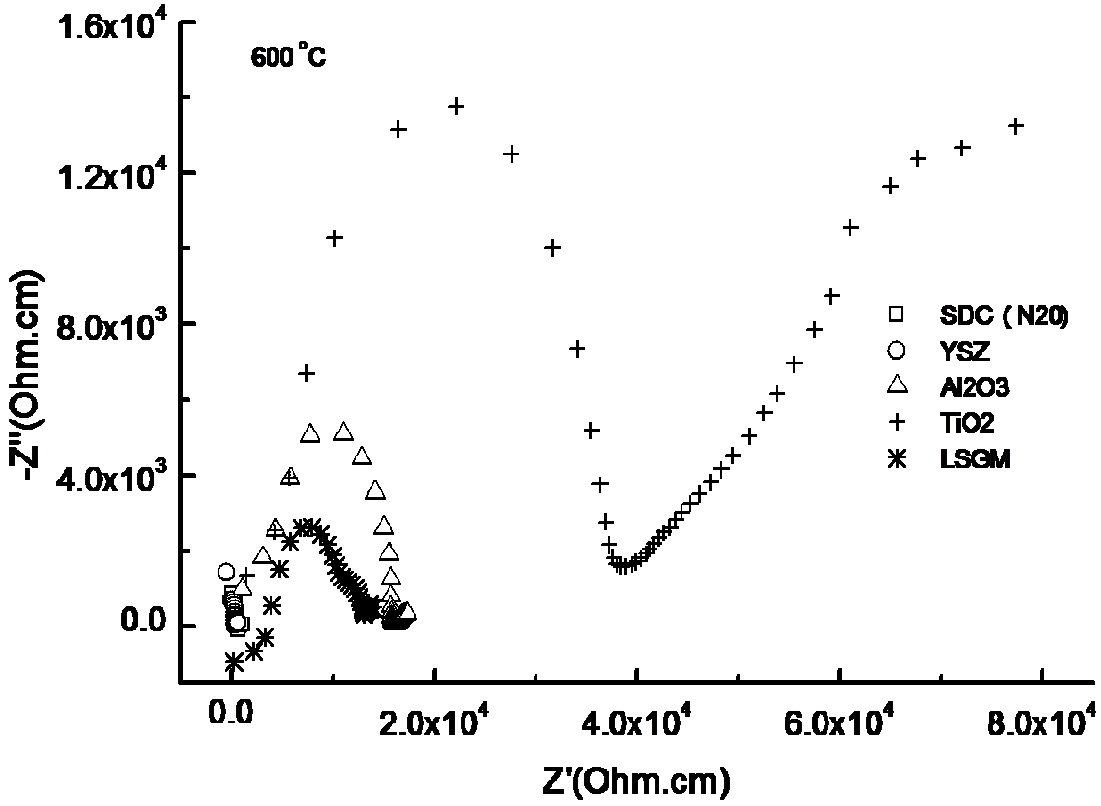

Figure 3.61. The Nyquist spectra of composites (SDC (N20) was represented by squares; YSZ composite was represented by circles; A_2lO_3 composite was represented by cross; LSGM composite was represented by the stars). All composites were containing 20 wt% of Na_2CO_3. Composite pellets were heat-treated at 700 ^oC for 1 hour. The measurements were taken in air at the temperature of 600 ^oC.

Chapter 4: Discussion

The main objective of the dissertation is to address how the properties of interface between the two constituent phases affect ionic transport mechanisms; and under which circumstances, it can particularly improve ionic conduction properties of two phase nano-composite electrolyte.

4.1. Composite Constituent Phases

This section focuses on structural, thermal, and electrical properties of each constituent phase. These phases are (two types of) samarium doped cerium oxide powders (SDC HP or SDC N20) and sodium carbonate (Na_2CO_3). The possible reactions between the constituent phases were investigated prior to producing composites. The investigation began by probing the crystal structure, thermal behavior, and surface morphology of each constituent phase with XRD, STA, and SEM.

4.1.1. Na_2CO_3 Matrix Phase

XRD patterns of both as-received (commercial) Na_2CO_3 and heat-treated (at 700 ^oC for 1 hour) powders (Figure 3.1) showed the purity and crystalline phase of carbonate. XRD of the as-received Na_2CO_3 powders illustrated that the as-received Na_2CO_3 powders consisted of Na_2CO_3, $Na_2CO_3.NaHCO_3.H_2O$, and $Na_2CO_3.H_2O$. In addition, preliminary Ritveld analysis also supported this composition. During the heat-treatment, the $Na_2CO_3.H_2O$ lost its hydride (H_2O); and $NaHCO_3$ decomposed to Na_2CO_3 CO_2 and H_2O. These were supported by both

XRD and SEM analysis. For instance, during the heat-treatment process, the hydrated portion ($NaHCO_3$) of as-received Na_2CO_3 lost its monohydrate water, as could be seen from the disappearance of the monosodium carbonate ($NaHCO_3$) peaks at 2θ values of 32°, 34°, and 36° in Figure 3.1. This decomposition was also confirmed by the changes in the SEM micrograph (in Figure 3.2 (a) and (b)). SEM micrograph suggested that the heat-treatment procedure (at 700 °C) did not change the crystalline state of Na_2CO_3 but just the surface morphology. In Figure 3.2 (b) one can still distinguish the grain boundaries between the fused Na_2CO_3 crystals.

In addition, FTIR analysis was employed to confirm the existence of monosodium carbonate ($NaHCO_3$) phase in the as-received powders (Figure 3.3). Observation of the two bands at the wave-numbers of 1599 cm^{-1} and 1682 cm^{-1} could be associated with the formation of two types of water: hydrogen bonded water and non-hydrogen bonded water. The signal at 1599 cm^{-1} wave number corresponded to the position of the bending mode of free water in the vapor phase whereas, the strong band at the wave-number 1682 cm^{-1} corresponded to hydrogen bonded water. The bands at 996 cm^{-1}, 1300 cm^{-1}, 1604 cm^{-1}, and 1908 cm^{-1} were belonging to $NaHCO_3$. The band at the wave-number 1067 cm^{-1} corresponded to the narrowing of the O-C=O chain during the heat treatment. Together with XRD results, FTIR absorbance spectra taken before and after the heat treatment at 700 °C confirmed that during the heat-treatment, Na_2CO_3 does not change its crystal structure.

After dissolving in water, surface morphology of Na_2CO_3 changed dramatically. For instance, SEM image (in Figure 3.4) revealed different morphologies with significantly different crystal sizes. The long stick-like and more irregular rectangular shaped particles were formed.

In water, Na_2CO_3 reacted with water to from $NaHCO_3.H_2O$. (The SEM image of the as-received $NaHCO_3$ was reported in the appendix 3.)

4.1.2. SDC Skeleton Phase

The primary particle sizes of SDC (N20) nano-powders were in the range of 5 nm to 10 nm (shown in TEM microstructures in Figure 3.5 (a)). SDC (HP) micrometer powders sizes varied from 100 nm to 500 nm, which could be identified from TEM microstructures in Figure 3.5 (b). Micro and nano-crystalline diffraction rings in Figure 3.5 (c) and (d) from both powders confirmed the fluorite structure. Due to the nano- size property, the diffraction rings for the SDC (N20) were more continuous as it is typical for nano-crystalline particles.

XRD spectra for SDC (N20) and SDC (HP) (in Figure 3.6) confirmed that both SDC powders had the same fluorite structure despite having varied particle sizes. The vastly different particle size effect could be observed in the drastically different FWHMs and peak intensities of the peaks in the two spectra. But both had exactly the same number of peaks at the same 2 theta values indicating the same fluorite structure. The peaks were labeled with the (*hkl*) indices of (110), (200), (220), (311), (222), (400), (331), and (420). All peaks appearing in the composite powder, in XRD patterns, were well matched with fluorite structure. Due to the nano-sized property of the SDC (N20) powders, the XRD peaks were broadened in these spectra. This phenomenon was also observed in Figure 3.5 (d).

The SEM micrographs shown in Figure 3.7 were taken from SDC (N20) nano-sized powder compacts (pellets) that were heat-treated at 700 ^oC for 1 hour and 1100 ^oC for 8 hours. The same electron voltage (3 keV) and same magnification (150 K) were used to provide a basis

for visual comparison. Micro-structures in Figure 3.7 (a) and (b) revealed the heat-treatment effect on morphologies that can be summarized as;

1. Figure 3.7 (a) revealed that pure SDC (N20) pellet heat-treated at 700 °C for 1 hour had a porous surface. The individual particles were difficult to distinguish at this magnification. The particles size had not changed from the original (as-received) powder particle size. Obviously not much diffusion had taken place at this temperature. The microstructure was typical of un-sintered ceramics. Thus, this heat-treating condition was not sufficient to densify SDC pellet.
2. Figure 3.7 (b) showed a dense surface with about 200 nm sized, individual SDC (N20) grains. SDC (N20) particle compacts, which were heat-treated at 700 ^{o}C for the same duration of time, disintegrated easily upon application of a slight mechanical force. However, the composite that was under-went similar heat treatment (i.e. 700 °C for 1 hour) could withstand higher mechanical force compared to the single phase SDC. The composites could easily be handled for electrical measurements. This again confirmed that the carbonate phase acted as glue for the SDC particles.

4.1.3. Electrical Properties of Each Constituent of the Electrolyte

The Table 3.1 compared the electrical conductivities of each constituent phase measured by impedance tests under the same experimental conditions (Figure 3.8). The conductivity of the $NaHCO_3$ was also included, since commercial Na_2CO_3 contained small amounts of $NaHCO_3$. For example, at 200 °C, the conductivity value of SDC was 4 times of the conductivity of Na_2CO_3. On the other hand, $NaHCO_3$ conductivity was 1.5 times of the conductivity of Na_2CO_3. When the temperature was gradually increased to 300 °C, the measured conductivity

value of the SDC was 3 times of the conductivity of Na_2CO_3. At the same temperature, $NaHCO_3$ conductivity was 1.3 times the conductivity of Na_2CO_3. However, at 450 °C, the difference in corresponding conductivity values of the SDC to Na_2CO_3 fell to 2 times. This time, the conductivity of Na_2CO_3 was 6 times the conductivity of $NaHCO_3$. From room temperature to 300 °C, the conductivity of $NaHCO_3$ was higher than that of Na_2CO_3. This is the temperature range where $NaHCO_3$ decomposed to Na_2CO_3, H_2O, and CO_2. After 300 °C, the conductivity of the pellet, which was prepared from $NaHCO_3$ was smaller. Around 300 °C, during sintering $NaHCO_3$ decomposed. During the decomposition the evolved CO_2 and H_2O escaped the pellet, which was made of $NaHCO_3$ and fully densified yet. Thus, some pores and channels in the micro-structure formed. Later after sintering these pore channels were where the re-hydration of Na_2CO_3 due to atmospheric moisture took place. During impedance measurements after 300 °C, this re-hydrated Na_2CO_3 portion decomposed and leaving behind the pore channels again. Thus, even though, both compacts have the same chemical formula, they had a different conductivity due to the developed porosity for the pellet which was made of $NaHCO_3$. The calculated activation energies in this temperature range for SDC and Na_2CO_3 conductivities were 1.60 eV and 2.3 eV, respectively.

4.2. Thermal Properties

The DTA thermograms of two SDC powders were identical and no thermal event was identified in the temperature range from 200 °C and 900 °C (in Figure 3.9 (a)). The mass loss at 100 °C was due to the disappearance of adsorbed water. In DTA thermogram of as-received Na_2CO_3 powder, (shown in Figure 3.9 (b)) major weight loss was observed after 850 °C, which happened almost concurrently with the melting of the Na_2CO_3. Melting of a

crystalline solid or boiling of a liquid was usually related to the transfer of heat required for a phase change. Phase transitions in low molecular weight materials could be correlated with the sharp discontinuities in some primary physical properties. These included density, volume, V [$V = (\partial G / \partial P)_T$], and entropy, S, [$-S = (\partial G / \partial T)_P$], which were the first derivatives of Gibbs free energy, and were commonly termed as first order transitions. Melting was also a first order transition [63]. The decomposition of the carbonate salt was followed directly after the melting of the salt which is manifested by the huge weight loss after this temperature.

The step change in DSC spectrum of as-received Na_2CO_3 powder between 350 °C and 450 °C was attributed to a glass transition (Figure 3.10 (a)). This glass transition-like softening was also observed in dilatometer spectrum in Figure 3.10 (b). The thermal dilatation of the SDC 10 wt% Na_2CO_3 composites beyond the temperature of 815 °C (Figure 3.10 (b)) might be related to the possible shrinkage of sample length. This was mainly due to the reduced volume of Na_2CO_3, because Na_2CO_3 starts to decompose just above the melting temperature.

The evaporation of water occurred at 100 °C, an endothermic decomposition peak occurred at 140 °C, and melting peak of Na_2CO_3 occurred at 830 °C (Figure 3.11 (a)) for dried powder of Na_2CO_3 which were dissolved in water. This suggested that no volatile decomposition reaction had occurred in the suggested operating temperatures ranges (from 400 ^oC to 600 ^oC). Those thermal events were very similarly to thermal events in Figure 3.11 (b). The DTA/TGA thermograms of as-received (commercial) $NaHCO_3$ powders showed an endothermic decomposition at 140 °C and melting of the Na_2CO_3 at 830 °C.

The as-received Na_2CO_3 showed a broad peak in the temperature range between 350 °C and 450 °C (Figure 3.10). The step change in the baseline of the DSC thermogram corresponding

to change in the heat capacity was typical of a glass-transition type reaction for an amorphous material. Therefore, portion of Na_2CO_3 was considered being in a glassy state. Above glass transition temperature of the matrix, the composite became soft and flexible which was observed in the dilatometer tests. Those observations also implied that Na_2CO_3 powders were at least partially amorphous. Similarly, a SEM micrograph of the heat-treated Na_2CO_3 pellet (displayed in Figure 3.12) illustrated that the featureless semi-transparent amorphous appearance of Na_2CO_3. SEM micrograph Figure 3.12 suggested that the heat-treatment process led to partial melting of Na_2CO_3.

4.3 The Effect of Sintering Temperature on Electrical Property

In most of the related literature, the heat-treatment temperature for composite was 700 °C for 1 hour [10,11]. In order to find out at which temperature the SDC based composite could reach the highest density (above 95%) and conductivity, 4 different sintering temperatures were investigated. Those 4 temperatures (700 °C, 750 °C, 800 °C, and 850 °C) were just below the melting temperature of Na_2CO_3. The maximum heat-treatment temperature was fixed to 850 °C, which approximately correspond to the melting of the Na_2CO_3.

A conductivity of the composite (SDC (HP) 10 wt% Na_2CO_3) which was sintered at 850 °C had the highest conductivity (Figure 3.13) in the temperature region from 200 °C to 550 °C. For example, at 200 °C conductivity values of the composite which was sintered at 850 °C was 5.6 times of the conductivity of the composite which was sintered at 700 °C. However, difference in conductivity gradually decreased in the temperature ranges from 300 °C to 600

°C. For instance, at 400 °C conductivity ratio between the composite which were sintered at 850 °C and 700 °C was 1.4 times.

All those composites had the same carbonate to oxide ratio (by wt%). There might be two possible reasons which might explain the variation in the conductivity of the composites. One was density and second one was oxide surface effect. In the first case, the density was related to the sintering temperature. The different sintering temperatures possibly led to varied particle sizes and pellet densities of the composites. Therefore, the morphology analyses were performed to monitor the grain growth during the measurement on SDC (HP) composite with Na_2CO_3 10 wt%, which was subjected impedance measurement. The particle size was on the order of 0.5 μm which was 100 times higher of the initial particle size (Figure 3.5). SDC particles were inter-connected and imbedded in the matrix (Figure 3.14). The performed EDX mapping (in Figure 3.14 (c)) from the region in Figure 3.14 (d) indicated that the matrix region was carbonate. Therefore, the varied sintering temperature produced the varied particle size thus the conductivity of the composite was varied accordingly. Density was also very important for the electrolyte material performance due to the fact that the pores would contribute like a grain boundary in terms of resistivity thus decreased the total conductivity of the specimen [71]. Therefore, the density measurements were performed to confirm the argument. The composite which was sintered at 700 °C had the highest density (around 98%) and conductivity compared to the other composites which were sintered at other temperatures (in Figure 3.15). Therefore, 700 °C and 1 hour sintering time were chosen as the standard heat treatment procedure for composite manufacture.

4.4. Variations in the Pellet Fabrication, Their Effects on Microstructure, and Electrical Properties

In the study, both, dry-ball milled and solution-processed composites were investigated. The SE-SEM images (Figure 3.16) of the composites with different processing routes showed very similar morphologies in terms of cross-sectional density and the distribution of the two phases. Both composite morphologies revealed that Na_2CO_3 covered the SDC (N20) particles, constituted the matrix phase, and glued the particles in the composite together. The average grain size of SDC (N20) in the composite was smaller than 200 nm and glued to each other with the help of Na_2CO_3. The relative pellet density was above ≥98%.

The surface morphology of the composite which was prepared by the solution process revealed a core-shell structure (in Figure 3.17 (a)). The calculated thickness of Na_2CO_3 shell was around 20 nm. In addition, the inverse image (Figure 3.17 (b)) revealed that the SDC particles were imbedded in Na_2CO_3 matrix phase in the composite microstructure. In EDX mapping (Figure 3.17 (d)), both constituent phases appeared to be interconnected in 3D and Na_2CO_3 appeared to cover all the SDC surfaces. One of the reasons for observing the core-shell micro-structure might be due to the formed hydrate during the experimental processing. Therefore, the following information could be obtained by STA and Raman analyses (Figure 3.19);

1. The TGA spectrum of the ball milled composite powder revealed ~ 14% weight loss, which corresponded to the loss of monohydrate water of Na_2CO_3 (Figure 3.18). In contrast, the TGA spectrum of the solution processed composite powder revealed ~ 10% weight loss, which corresponds to the decomposition of $NaHCO_3$.

2. The only recognizable difference among the Raman spectra of composites was the weak wiggles in the Raman shifts around 3000 cm^{-1} for the composite by solution processing. They were belonging to the water in the structure (monohydrate water of Na_2CO_3). In Figure 3.19 (b) only one peak could be distinguished at 2000 cm^{-1} which was belonging to CO_2. Monosodium carbonate was an amphoteric compound and its aqueous solutions were mildly alkaline due to the formation of carbonic acid and hydroxide ion []. Since, the solution processed powder had high concentration of $NaHCO_3$, it had high tendencies to absorb the CO_2 compared to the dry ball-milled powder.

Thus, SEM surface morphology, TGA, and Raman analysis confirmed that during the solution process, the carbonate would form higher proportions of NaHCO3. After studying the SEM morphology and thermal analysis, processing effect on electrical property was also investigated (Figure 3.20). At all measured temperatures, processing route of the composite played a minor role on the electrical properties. For instance, at 200 °C dry ball milled composite's impedance conductivity value was $1.18x10^{-6}$, while solution processed composite conductivity value was $1.47x10^{-6}$. Therefore, there was only 15% difference in the resistivity values. At 600 °C, both pellets produced nearly identical spectrum.

To sum up these systematic investigations of the processing parameters on composite's property, 3 conclusions could be achieved.

1. Both dry ball-milled and solution mixed procedure could produce homogeneously distributed and dense micro-structure. Dry ball-milled processed composite formed core-shell morphology.
2. During the solution process, the composite had a higher chance to form monohydrate Na_2CO_3 and $NaHCO_3$. Composite prepared with dry ball milled phases lost 14 wt% up on

heating up to 700 °C, while the composite that was prepared from solution processed powders lost 10 wt% weights up on heating.

3. The difference in the electrical conductivity at low temperature ranges (200-400 °C) was around 12 %. At 600 °C, the difference in the processing was negligible.

4.5. The Effect of Milling on Composite Electrolyte Production

The composites powders were prepared by two routes, such as mixing and dry ball-milling routes. The milling parameters were evaluated according to the feed-backs from XRD, Raman, and DTA analyses (Table 3.2).

The DTA thermogram of Na_2CO_3 powders (in Figure 3.21 (a)) showed 2 thermal events. At 100 °C, an observed mass loss was because of the loss of water. The major weight loss was observed after 850 °C that was after Na_2CO_3 started to melt (Figure 3.21 (b)). There was no difference in DTA spectra of milled and mixed composites.

The main difference between the XRD spectra of simply-mixed composite powders and ball milled composite powders were the weakening of crystalline peaks belonging to sodium carbonate and monosodium carbonate phases. It appeared that ball milling caused the carbonate component of the composite to lose some of it crystalline nature. The main difference between the milled and calcined composite powders was the disappearance (or significant weakening) of the peak at ~34 ° 2 θ which is common peak for the sodium carbonate and mono-sodium carbonate phases. In addition, Raman analysis of the same powders (shown in Figure 3.23) indicated only slight structural changes in Na_2CO_3 where part of the carbonate phases lost their crystallinity. Therefore, both XRD pattern and Raman

patterns confirmed that sample processing through milling did not affect the phase distribution and did not change that fact that it is difficult to detect sodium carbonate phase by XRD.

4.6 The Detection of Na_2CO_3

In the following section, the milling parameters were held constant to systematically evaluate the presence of Na_2CO_3 in the composites. Herein, the following s2 sets of XRD experiments were designed that were also listed in the table 3.3.

1. The XRD spectra taken from samples that was only milled SDC (HP) composites with 10 wt% and 50 wt% Na_2CO_3.
2. The XRD spectra taken from sample that was mixed by ball milling and heat-treated SDC (HP) composites with 50 wt% Na_2CO_3.

XRD pattern of the composite that was made up of SDC (HP) with 50 wt% Na_2CO_3 showed peaks belonging to both SDC powder and carbonate (Na_2CO_3 and $NaHCO_3$) powders. Thus, when carbonate concentration level was increased up to 50 wt% weak intensity diffraction peaks with very weak intensity that was belonging to Na_2CO_3 could be observed (Figure 3.24). Therefore, it signified that increasing the Na_2CO_3 concentration could manipulate the visibility of the Na_2CO_3.

Compared with the diffraction peaks in Figure 3.25 (b), the heat-treated composite powders that were (Figure 3.25 (c)) made up of SDC with 50 wt% Na_2CO_3 revealed reduced relative

intensity of the Na_2CO_3 peaks. Even if there was some crystalline carbonate phase in the composite, a portion of carbonate became amorphous during heat treatment. Thus, decreased intensity of carbonate peaks was observed. Reported XRD investigations in literature on ceria based composites also indicated amorphous nature of Na_2CO_3 [54,73] in their composites. One of the other possible reasons why distinct carbonate peaks were not observed could be the small amount of Na_2CO_3 in the composite. For instance, a maximum of 30 wt% Na_2CO_3 concentration was used in the literature and this was too little to give intense x-ray peaks compared to SDC x-ray peaks [51]. Thus, Na_2CO_3 peaks were not observed.

Raman analysis of the SDC composite with 50 wt% Na_2CO_3 powders (shown in Figure 3.26) indicated only slight structural changes in Na_2CO_3 where part of the carbonate phases lost their crystallinity. The DSC thermogram of only-milled SDC (N20) composite with 50 wt% Na_2CO_3 (in Figure 3.27) revealed one broad signature of a thermal event. This broad feature in the temperature range from 295 °C to 335 °C was due to the glass transition of amorphous Na_2CO_3. Therefore, it suggested that during the milling procedure, Na_2CO_3 became at least partially amorphous. To summarize, it is difficult to prove the crystalline nature of sodium carbonate wit XRD. Only when the presence of Na_2CO_3 was increased the crystalline portions of the carbonate phase gave enough x-ray signals that could be detected. The thermal behavior of the composite also gave strong indicators for both structural modifications of the carbonate phase, *i.e.,* crystalline as well as amorphous portions of the matrix carbonate phase.

4.7. Effect of $NaHCO_3$ and Na_2CO_3 on SDC Composites Properties

In order to investigate the role of $NaHCO_3$ and Na_2CO_3 on both SDC (N20) and SDC (HP) composites, impedance analyses of composites were performed. Both composites contained 20 wt% carbonate salt.

4.7.1 Effect of $NaHCO_3$ and Na_2CO_3 on Nano-SDC Composites Properties

SDC (N20) composites with Na_2CO_3 had slightly low impedance values (*i.e.*, slightly high conductivities) (in Figure 3.29) compared with the SDC (N20) composite with $NaHCO_3$ at temperatures ranges from 200 °C to 500 °C. The difference in conductivity of the composites was negligible due to the fact that both composites had the same weight ratio of SDC to carbonate salt.

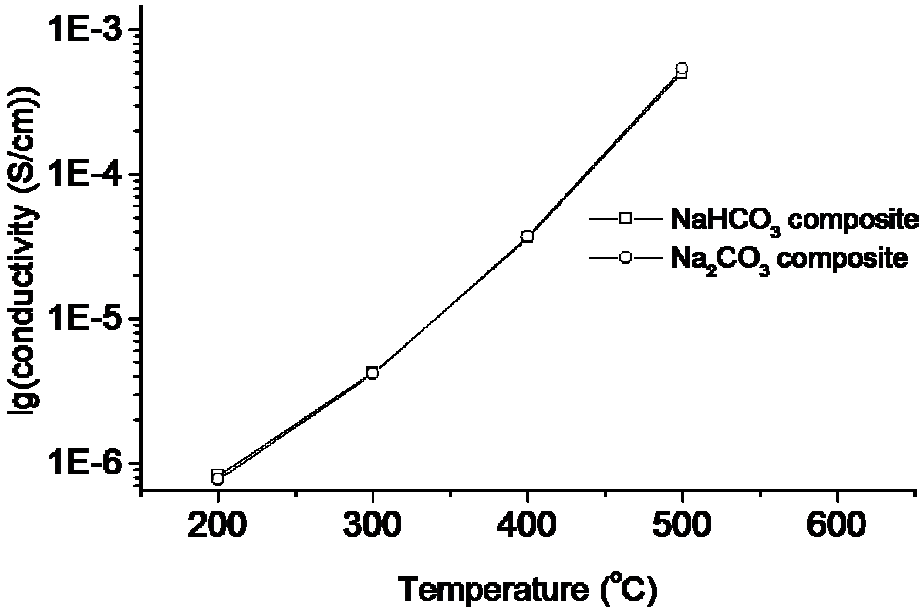

Figure 4.1. The conductivity versus temperature plots of the composites. The SDC (N20) composite with Na_2CO_3 was presented by open circles and the composite with $NaHCO_3$ was presented by open squares. The plots were measured at the temperature between 200 °C and 600 °C. Composite pellets were heat-treated at 700 °C for 1 hour and containing 20 wt% Na_2CO_3 or $NaHCO_3$.

4.7.2 Effect of $NaHCO_3$ and Na_2CO_3 on micro-SDC Composites Properties

In order to investigate the effect of $NaHCO_3$ and Na_2CO_3 on SDC (HP) composite, calculated conductivities were compared in Figure 4.2 (The impedances were presented in Figure 3.30 and 3.31). At temperatures from 200 °C to 500 °C, SDC (HP) composites with Na_2CO_3 had lower impedance, *i.e.*, higher conductivities (Figure 4.2) compared with the composite with $NaHCO_3$.

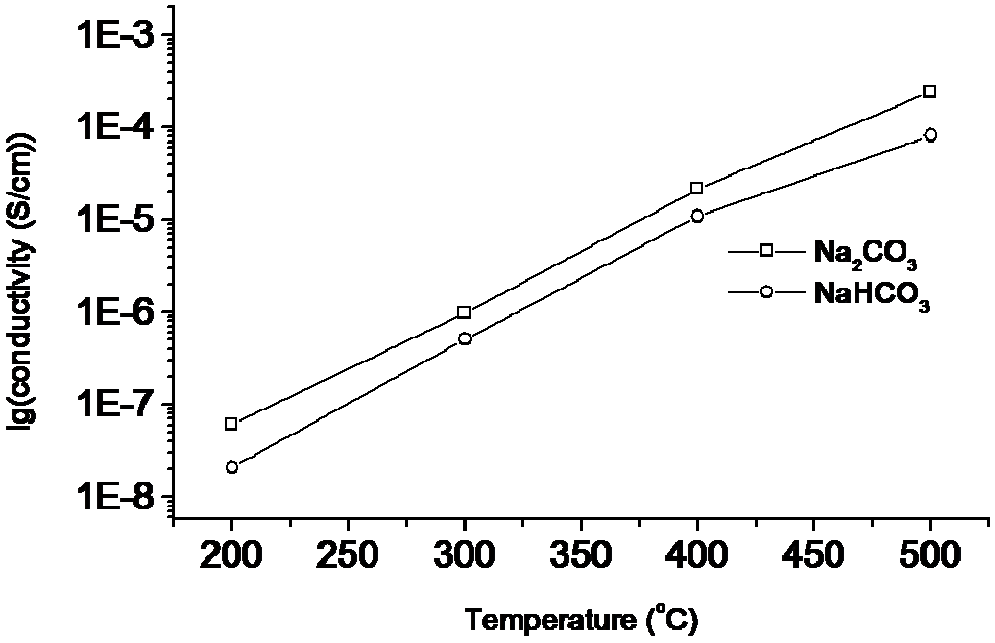

Figure 4.2. The conductivity versus temperature graph of composites. The SDC (HP) composite with Na_2CO_3 was presented by open squares and the composite with $NaHCO_3$ was represented by open circles. The plots were measured at temperatures between 200 °C and 600 °C. Composite pellets were heat-treated at 700 °C for 1 hour and containing 20 wt% Na_2CO_3 or $NaHCO_3$.

The impedance results could be interpreted as summarized below:

1. The incorporation of 20 wt% Na_2CO_3 or $NaHCO_3$ into SDC (N20) composites made no

significant differences in resistivity values. For instance, at 300 °C the resistivity value of the composites with Na_2CO_3 was 3.37 $x10^5$ (Ω.cm) that was nearly equal to the value obtained for the composite with $NaHCO_3$, 2.42$x10^5$ (Ω.cm).

2. The incorporation of 20 wt% Na_2CO_3 or $NaHCO_3$ into SDC (HP) composites led to differences in resistivity values (in Figure 3.31). For instance, at 200 °C the resistivity value of the composites with Na_2CO_3 (1.65$x10^7$ (Ω.cm)) was 1.9 times of the value obtained for the composite with $NaHCO_3$ (4.81$x10^7$ (Ω.cm)).

There were 2 possible reasons that might explain the similarity in conductivity values of the two SDC (N20) composites. Firstly, both composites have the same ratio of SDC (N20) to carbonate salt. Secondly, the high surface areas of the SDC may have overturned the influence of salt type variation in the composite. (The effects of oxide surface and interface will be discussed in details in the section 4.11 and 4.12).

On the other hand, the observable differences in conductivity of the SDC (HP) composites were due to the combination of developed porosity and less surface areas of the SDC (HP) particles. Even though, both compacts had the same amount of carbonate salts, they had different conductivities due to the developed porosity that was left by the decomposition of the monosodium carbonate to carbonate phase for the composite pellet which was made of $NaHCO_3$. This phenomenon also might happen for the SDC (N20) composite; however, as mention earlier, the surface area effect may have overturned the variation of salt type. Thus, composite with SDC (HP) was more sensitive to the variation of the salts.

4.8 Effect of Na_2CO_3 and $LiNaCO_3$ on SDC (N20 or HP) Composite Properties

The SEM morphology and thermal property analyses of the (SDC) composites with $LiNaCO_3$ exhibited two significant features, as follows;

1. The incorporation of 20 wt% $LiNaCO_3$ on both SDC (N20 or HP) composites effectively improved both SDC (N20 or HP) particles dispersion in $LiNaCO_3$ matrix (Figure 3.32). In addition, the SDC particles size distributions were also homogeneous compared with the composite with single phased Na_2CO_3.

2. The incorporation of 20 wt% $LiNaCO_3$ in the SDC (HP) composite effectively reduced melting temperature of the composite to 492 °C that was around 350 °C lower than SDC (HP) composite with 20 wt% Na_2CO_3 (Figure 3.33).

3. The STA spectrum of the SDC (HP) $LiNaCO_3$ 20 wt% composite pellet revealed a small endothermic peak at 840 °C. This temperature also corresponded to the starting of the decomposition of the pellet (Figure 3.33). Effectively the LiNaCO3 containing composite showed both melting behavior, i.e. the melting of Li-carbonate and malting of Na-carbonate.

The measured resistivities of the SDC (HP) composites with 20 wt% Na_2CO_3 and $LiNaCO_3$ (Figure 3.34 and Figure 3.35) were included in Table 4.1. For all measured temperatures (*i.e.,* between 200 °C and 500 °C), the impedances of the composites with Na_2CO_3 were smaller than that of composite with $LiNaCO_3$. For instance, at 200 °C, the impedance of the composites, which was made with $LiNaCO_3$, was 3 times of the impedance of the composite which was made with Na_2CO_3. Similar trend was observed at 300 °C. For instance,

impedance of the composite with Na_2CO_3 was 4 times smaller than that of the impedance of the composite with $LiNaCO_3$. As the measurement temperature was increased, composite that was made of $LiNaCO_3$ underwent softening phenomena earlier than the composite that was made of Na_2CO_3. Those results suggested that incorporating binary salt may not increase the total conductivity in the ceria based composite. Though, binary salt decreased the effective melting temperature of the composite around 350 °C.

Table: 4.1 The calculated resistivity form the impedance spectra (Figure 3.35)

Temperature (°C)	**SDC (HP) $LiNaCO_3$ 20 wt% (Ω.cm)**	**SDC (HP) Na_2CO_3 20 wt%(Ω.cm)**
200	$4.8x10^7$	$1.6 x10^7$
300	$4.0 x10^6$	$1.0 x10^6$
400	$2.0 x10^5$	$4.8 x10^4$
500	$5.5 x10^3$	$3.8 x10^3$

4.9. Percolation of the Oxide-Matrix Interface

It was widely known that the incorporation of Na_2CO_3 into ceria-based oxide increased the electrical conductivity of the composites in LT-SOFC [58,61]. However, depending on the surface area characteristic of oxide particles, composites exhibited a different electrical conduction behavior under the same experimental conditions. The Na_2CO_3 concentration in the composite was varied at constant temperature in order to explore the percolation behavior

of the constituent phases and the interfaces between them, and determine the optimum set of parameters.

When comparing the XRD of series of composites (Figure 3.36), all the diffraction indices were coming from SDC diffraction except for the XRD spectra of the 50 wt% composite. Only for the composite with 50 wt% carbonate concentration, some characteristic peaks were observed at the 2θ of 31° and 33° which are belonging to Na_2CO_3 peaks. Therefore, there might be 3 possibilities for not observing the carbonate in the composite XRD spectra. Firstly, the XRD peaks were not visible due to the fact that the carbonate amount in the composite was low. Secondly, Due to the strong difference in the structure factors, for instance, the Sm (58) and Ce (62) elements had high atomic numbers compared to the carbonates. Therefore, difference in structure factors influences the intensity of the diffraction peaks. Thirdly, the carbonate phase turned amorphous during the composite processing even if it was crystalline when it was by itself.

4.10. The Percolation of the Interface in SDC (N20) Composites: Electrical Characterization

The impedance curves of the composites with the varied Na_2CO_3 concentrations were illustrated for 300 °C in Figure 3.37. The Nyquist curves of composite, SDC and Na_2CO_3 (Figure 3.37), can be interpreted as follows;

1. The incorporation of 10 wt% Na_2CO_3 into the composite significantly reduced resistivity compared to that of pure SDC (in Figure 3.38 and appendix 4). For instance, at 300 °C the resistivity value of pure SDC pellet was 3.8 $x10^5$ (Ω.cm), which was 2 times higher than the

value obtained for 10 wt% concentration Na_2CO_3 (~24 vol%) $1.1x10^5$ (Ω.cm).

2. At 300 °C, all complex impedance spectra exhibited two overlapping semi-circular arcs in the spectra of composite (in Figure 3.37). These two semicircles could be attributed to phenomena occurring in at least two chemically distinct components even without considering any interfaces or grain boundaries in between or within them. From these two semi-circular arcs one could determine two different relaxation frequencies based on the change of RC values related to the two coexisting phases [59,69]. Moreover, the depressed high frequency arcs for composites with 5 wt% and 10 wt% Na_2CO_3 concentrations were verifying the coexistence two phases with very different relaxation times [59].

Both, impedance loss (-Z″) and real portion of the impedance (Z′) values decreased significantly upon increasing Na_2CO_3 concentration up to 10 wt%. For instance, the resistivity value of the composite with 5 wt% concentration Na_2CO_3 (~13 vol%), was in the order of $1.89x10^5$ (Ω.cm), while the composite with the 10 wt%, (~24 vol%) resistivity value was at around $1.11x10^5$ (Ω.cm) at 300 °C. The resistance of 5 wt% Na_2CO_3 composite was 2 times higher than the resistance of the composite with 10 wt% Na_2CO_3 .However, when Na_2CO_3 concentration increased to 20 wt% in the composite, the complex impedance revealed a semi-circular arc with a resistivity value of $2.44x10^5$ (Ω.cm). That value is higher than the value for 10wt% NaCO3 containing composite. At all temperatures, Nyquist plots of the composites with 10 wt% Na_2CO_3 showed the lowest resistivity.

One important factor at influenced the impedance of those composites was the ratio of Na_2CO_3 to SDC phases. Another factor was their relative distribution in the composite micro-structure (Figure 3.39). There was an optimum value for the relative ratio of the two

constituent phases. Below and above this optimum value, the conductivity of the composite showed a marked decrease. This behavior was interpreted in the literature as the typical percolation behavior of the composite (Figure 4.3).

Therefore in the study presented here, the conductivity percolation was observed with 10 wt% carbonate amount. Those resistivity values depended on 3 factors, such as homogeneity of the composites, pellet density and interface amount between two phases.

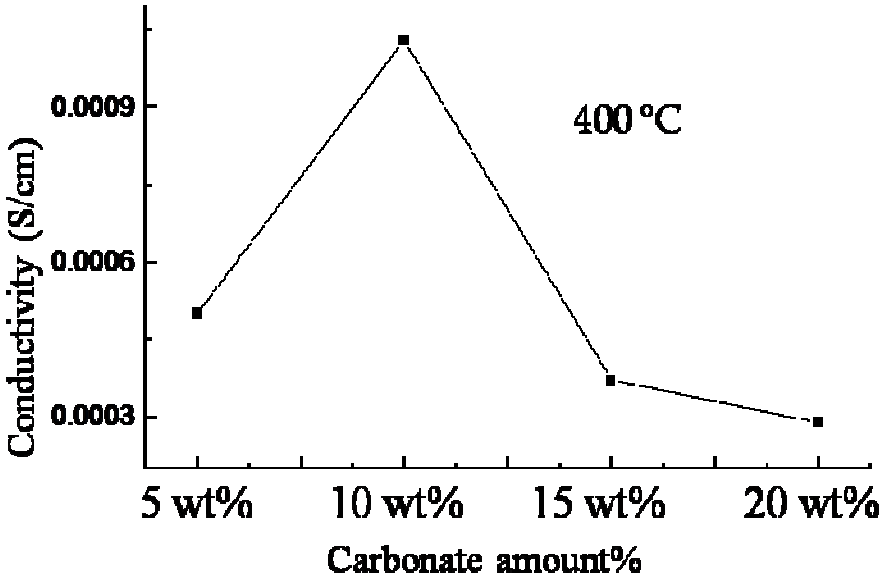

Figure 4.3: The calculate conductivity of all the composites at 400 ^{o}C. The all composites were containing 5 wt%, 10 wt%, 15 wt%, and 20 wt% of Na_2CO_3. Composite pellets were heat-treated at 700 ^{o}C for 1hour. (Plotted again here for better explanation and same with Figure 3.43)

Above a certain Na_2CO_3 concentration the carbonate phase was continuous. For example, in our studies, the 10 wt% composite reached a homogeneous micro-structure with a continuous SDC phase. However if the carbonate phase would have been critical for conduction at all

concentrations above the threshold value, the conductivity would have at least stayed high. If it were the SDC phase which would have been critical for conduction at low concentrations of Na_2CO_3 the composite conductivity should have been high as well. However, the conductivity was a maximum at a critical value of the carbonate. This could only happen if the feature that was determining for the conductivity was common to both phases. This common feature was the interface between the two constituent phases. Therefore, it could be concluded that the conductivity of the composite was ultimately linked with the amount and the state of the interfaces between the oxide particles and the sodium carbonate matrix.

The shape of the impedance curves changed with changing Na_2CO_3 concentration in the composite. Overlapped semi-circular arcs in the composites with 1 wt% and 5 wt% Na_2CO_3 concentrations were very asymmetric compared to the arcs of the composites with 10 wt%, 15 wt%, and 20 wt% Na_2CO_3 concentrations (Figure 3.37). The difference, depending on Na_2CO_3 concentrations, was the consequence of the volume variations of two constitute phases. For example, 1 wt% Na_2CO_3 in the composite approximately equals to ~4.7 vol% in the composite, while 5 wt% Na_2CO_3 approximately equals to ~13 vol%. These significant volume differences of each constituent phase in the composite in this range, led to an asymmetric overlapping of the two semi-circles in the spectrum. The impedance spectra of the composites with 10 wt% (~24 vol) and 20 wt% (~41 vol%) Na_2CO_3 concentrations produced symmetric high frequency and low frequency semi-circles since volume ratios of each constituent phases were most comparable to ratio 1/3. For example, for the composites 10 wt% (24 vol) which contain Na_2CO_3 phase to SDC phase with the volume ratio of ~24 vol%/ 76 vol% (~0.3). In addition, the composites 20 wt% (41 vol) which contain Na_2CO_3 phase to SDC phase corresponding to the volume ratio of ~41 vol% and 59 vol% respectively (~0.31).

Those particular volume ratios could be explained by taking the Bruggeman symmetric effective medium model into account [69]. This model did not make a distinction between the continuous and discontinuous phases and therefore, the relevant expression was symmetrical in φ_1, φ_2. The Bruggeman symmetric model was described by Equations (4.1, 4.2, and 4.3)

$$\varphi_m = \frac{1}{4}\left\{q + \left(\sqrt{q^2 + 8\varphi_1\varphi_2}\right)\right\} \quad \text{Equation (4.1)}$$

Where

$$q = (3x_1)\varphi_1 + (3x_2 - 1)\varphi_2 \quad \text{Equation (4.2)}$$

and

$$x_1 + x_2 = 1 \quad \text{Equation (4.3)}$$

φ was the complex conductivity, x was the volume fraction. In the effective medium model consideration, Equation (4.2) became dominant in calculations by the volume fraction of the high conductivity phase approaches 1/3. This could be verified by substituting two unequal values of real conductivity. Thus, the model provided an elementary and mathematical description of the phase percolation. According to this model, when the second phase reached 30 vol%, the composite reaches it's optimum electrical properties. Figure 3.38 compared the impedances of the SDC (N20), Na_2CO_3, and SDC (N20) composite with 10 wt% Na_2CO_3.

The SEM micro-structure confirmed homogeneously dispersed SDC (N20) and Na_2CO_3 phase at 10 wt% and 15 wt% concentrations (in Figure 3.39). The SEM morphology of the composite with 1 wt% carbonates showed SDC (N20) phases only. The two phases could be differentiated by the difference in their contrast in 5 wt% composite SEM morphology. The bright regions were due to SDC oxide particles and the glassy and featureless region were due

to carbonate. Those were confirmed by the further EDX analysis (Figure 3.40). The composite had a 98% dense microstructure, which was because Na_2CO_3 phase filled all the pores in the composite pellet during the heat-treatment at 700 °C. The heat-treatment caused the Na_2CO_3 phase to act as a glue for the SDC particles. The carbonate amounts were further increased to 20 wt% and 50 wt% to check the phase distribution (in Figure 3.41 and 3.42). The 20 wt% Na_2CO_3 containing composite contain the 41 vol% Na_2CO_3 matrix. SEM image in Figure 3.41 displayed a large portion of featureless matrix phase signifying that the Na_2CO_3 matrix phase was in an amorphous state. In the composite with 50 wt% carbonate, the oxide particles were separated from each other (in Figure 3.42). Thus, one of the reasons for the higher resistivity values of the composites was due to dominating carbonate phase. The concentration of the Na_2CO_3 already exceeded the percolation limit in these composites.

The conductivity values of the composite with various carbonate concentrations were shown in Figure 3.43. For the SDC (N20) Na_2CO_3 composites, the percolation of interface occurs at 10 wt% (~24 vol%) Na_2CO_3 concentration. Further increase in Na_2CO_3 to SDC ratios in the composite led to a decrease in the total electrical conductivity. In the appendix 5, the calculated conductivity was listed for comparison.

4.11. The Design of Interface by Specific Surface Area

The inverse relationship between the particle size and specific surface area of oxide particles in the composite allowed us to observe the effects of total interface area in the composite, while keeping the amount of the constituent phases constant. In this way it was possible to isolate the interface effects from the phase ratios in the composite.

The SEM images of all composites were analyzed to check the density and SDC size distributions in the composite (Figure 3.44). The 203 SSA composite had a high interface area with homogeneously distributed SDC (N20) particle sizes. On the other hand, the composite micro-structures with mixed SDC (N20) and SDC (HP) powders showed bimodal particle size distribution. For instance, other composites with different SSAs contained both nano sized powders whose particle sizes were below 50 nm and bigger sized powders which had particles around 200 nm in size.

Ionic conductivity behavior and electrical properties of the electrolyte nano-composite were determined by AC impedance analysis. The impedance analyses of composites with different SSAs (*i.e.*, interface area) revealed the influence of the amount of oxide surface on conductivity (Figure 3.45). Decrease in total resistivity with rising temperature indicated a negative temperature coefficient of resistance (NTCR) for the composites [76]. With increasing SSA, *i.e.*, smaller sized oxide particles, both ($-Z''$) and (Z') values decreased monotonically at all measurement temperatures (Figure 3.45).The resistivity values of the composite with a high SSA (specific surface area), *i.e.*, ~203 $m^2.g^{-1}$, were on the order of 1.2 x 10^5 (Ω.cm), while the one for the composite with a lower SSA, ~93 $m^2.g^{-1}$, was around 3.8 x 10^5 (Ω.cm) at 350 °C. This resistivity was 3 times higher in magnitude than the resistivity of the composite with the larger (203 $m^2.g^{-1}$) surface area. At room temperature, due to the very high resistivity values of the composite, it was difficult to fit the experimental data in the Nyquist plots to semi-circles. A depressed semi-circular shape for the arcs of Nyquist plots was observed in EIS spectra for all composites indicating several concurrent conduction phenomena. All Nyquist plots of the composites with different SSA exhibited two overlapping semi-circular arcs at 350 °C. The Nyquist plots for the composite were rather different from that of a single phase electrolyte material, such as LSGM, which usually

exhibits only one semi-circular arc in the complex impedance curve [32,77]. These overlapping semi-circular arcs were a consequence of at least two coexisting conduction events with different relaxation times [71]. Two maxima associated with a distribution of relaxation times at the complex resistivity level (representative of a dispersive behavior of the impedance) were observed (in Figure 3.45). The curve would be reduced to that of a single time-constant behavior; if there will be no dispersion [71]. The measured τ-values for the composite were not corresponding to the τ-values calculated for SDC or Na_2CO_3 phases. In addition, it was observed that the SSA of the oxide powders had a strong influence on the resistivity of the composite. The higher interface area between the oxide powder and the Na_2CO_3 matrix caused higher ionic conductivity. In addition, the short time constants were the consequence of the mobile species in the composite responding to high frequencies. The synergistic interaction between the matrix phase and the oxide surface apparently generated a new path, where the mobile ions can move faster and/or with greater ease than before. Therefore, it was reasonable to suggest that the two or more relaxation time constants originated from the synergy formed at the interfaces. These highly mobile ions in the interface regions were expected to follow the ac field up to high frequency due to shift at the peak maxima towards high frequencies (Figure 3.45). Those shift also resulted in the short relaxation times [61].

At temperatures above 450 °C, the complex impedance response (Nyquist plots) of all composites revealed only one dominant semi-circular arc indicating one conduction phenomenon overpowering the rest. For all measured temperature ranges, the so-called Arrhenius conductivity (σT) of the composites with higher SSA was larger than the conductivity of the composites with lower SSA (Figure 3.46). At the temperature around 350 °C, the composite and ball milled Na_2CO_3 showed a glass transition-like thermal behavior

(Figure 3.47). It was believed that above 350 °C, Na_2CO_3 started taking a dominating role in the conductivity, due to its softened amorphous structure. Therefore, around 450 °C only a single semi-circle was visible in the impedance curves, due to the dominant conduction in the matrix phase. Below 350 °C, *i.e.,* below the softening of the matrix phase, SSA played a dominant role. The ionic conductivity of the SDC - Na_2CO_3 with the highest 203 SSA (203 $m^2.g^{-1}$) was 3 times larger in magnitude than the conductivity of composite with the 47 SSA (47 $m^2.g^{-1}$) in this temperature range. All composites had exactly the same weight ratio of the Na_2CO_3 phase in their corresponding composition. Therefore, the only difference was the oxide particle size and the amount of SSA of the oxide particles, which were related to each other as SSA ~[1/particle size]. For the conductivities of the SDC pellets prepared with nano-sized or micrometer-sized, there was no significant difference. Therefore, the observed effect can be attributed to the interaction of the oxide surface with the Na_2CO_3 phase.

The high conductivity measured in the composite with the highest surface area could be attributed to one of two phenomena: (i) the hygroscopic nature of the Na_2CO_3 and (ii) the surface charges on the oxide particles. Due to its hygroscopic nature, the Na_2CO_3 absorbs moisture from ambient environment to form $NaHCO_3$. Therefore, in actuality the virgin composite electrolyte material was composed of SDC, Na_2CO_3, and $NaHCO_3$.

Figure 4.4 shows a simplified sketch of the composite material consisting of crystalline SDC particles (large circles) and a second carbonate phase (a mixture of Na_2CO_3 and $NaHCO_3$). In this model, the interfaces in composite electrolyte configuration included the regions of the ionic conductor SDC grains with some of the sodium ions adsorbed on them. Next to the oxide particles carbonate ions (the $(CO_3)^{-2}/(HCO_3)^{-1}$) formed a rim. This interphase might lead to the enhancement effect in the conductivity of composite materials at low temperature.

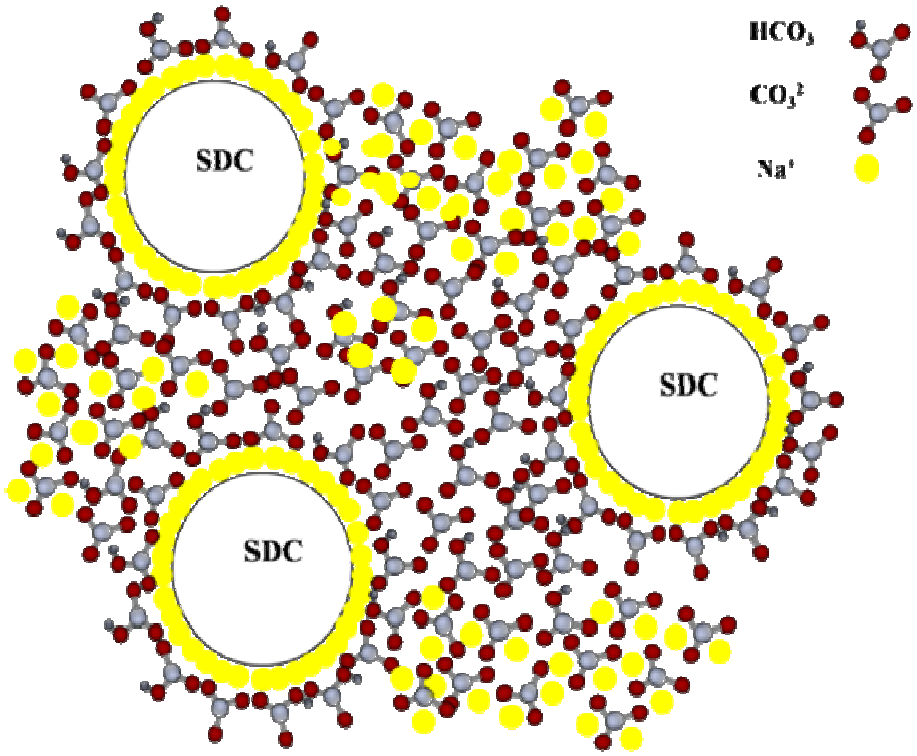

Figure 4.4. Schematic illustration of composite electrolyte materials of SDC and Na_2CO_3, $NaHCO_3$. The networks of interfaces consist of an interface between oxygen ion conductor SDC grains and Na_2CO_3.$NaHCO_3$ phase.

Liang discovered that when the insulator Al_2O_3 was added to the Li-ion conductor LiI, the overall conductivity of the composite electrolyte LiI:Al_2O_3 increases [36]. This unexpected benefit of an insulating oxide was explained by an enhanced conductivity in the interfacial regions that forms between the charged oxide particle surfaces and the electrolyte phase. Such systems were termed "dispersed ionic conductors" or better known as ''soggy-sand'' [78]. Conventionally, these composites were made up of liquid (electrolyte) matrix phase and dispersed sub-micrometer insulator particles. With the addition of oxide particles, the composite showed significant improvement in the ionic conductivity. There were several attempts to explain this unexpected behavior, such as a formation of space charge layers, an

enhanced concentration of defects, and/or the formation of new phases [58]. The model gaining widespread acceptance was the ‘‘soggy-sand’’ model, in which the oxide surface attracts one type of ionic species from the liquid electrolyte, so that the other ionic species were accommodated in the region (the rim) surrounding the oxide particles, where they formed a “super-ionic” interphase [58]. The presence of highly conducting interphases (which were wrongly termed interfaces in the existing literature) led to a pronounced increase in the total ionic conductivity. Our experiments with varying volume of oxide particles showed a percolation type of behavior, validating the model of conductive interphases around the particles.

In the investigated series of composite electrolytes, the conductivity plots of all composites followed a unique trend. The important features were the SSA dependent conductivity of the composites and two distinct conductivity regimes in two different temperature ranges above and below 350 °C. For instance, above 350 °C, the composite thermally softened and thus the conductivity became less dependent on the variation of the interface area. A lower activation energy observed at low temperatures (below 350 °C) was attributed to the contributions from Na_2CO_3, as well as $NaHCO_3$, to the ionic conductivity in composite electrolyte. The activation energy of the composite calculated from the plots differs from the activation energy for pure Na_2CO_3 or pure SDC pellet samples. Calculated activation energies for Na_2CO_3 and composite were found to be around 2.3 eV and 1.5 eV respectively, as shown in Figure 4.5. The difference between the activation energy of the composite and pure Na_2CO_3 was very close to the dissociation energy for the carbonate phase [79].

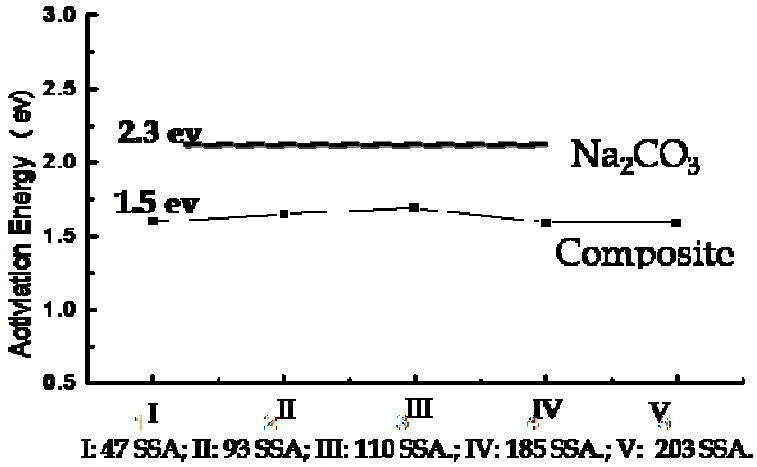

Figure 4.5.The calculated activation energy for composite SDC-Na_2CO_3 10 wt% as a function of SSA ((1) 47 $m^2.g^{-1}$, (2) 93 $m^2.g^{-1}$, (3) 110 $m^2.g^{-1}$ (4) 185 $m^2.g^{-1}$, (5) 203 $m^2.g^{-1}$,) and activation energy values for Na_2CO_3 pellet and $NaHCO_3$ pellet. The activation energy was calculated from the measured temperature range of 300 °C to 550 °C.

The ‘‘soggy-sand’’ model was based on an oxide surface acting as a dissociation agent for the electrolyte molecule, as proposed for liquid electrolytes in Li-ion batteries. An analogous function could be presumed for SDC particles in the nano-composite due to measured activation energies in these solid composite electrolytes. The relationship between ionic conductivity, SSA, and the type of oxide surface supported this interpretation. A description of the influence of different oxide surfaces and the conductivity of the composite was given in section 4.13.

The conductivity plots (which were taken at 200 °C in Figure 3.46) proved that at constant amount of carbonate, the conductivity values of the composite with highest SSA were several times higher than the composite with lowest SSA. Above 350 °C, the amount of interface area did not play a significant role as they did below this temperature. Furthermore, the conductivity enhancement at low temperatures was not observed at the second measurement

taken just after exposing the sample to temperatures above 350 °C. This was expected to be to the consequence of the decomposition of $NaHCO_3$ into Na_2CO_3 at a temperature of around 150 °C. Therefore, in reality the composite electrolyte material consists of SDC, Na_2CO_3 and $NaHCO_3$. At higher temperatures, such as above 350 °C, all composites gave similar conductivity values, due to the dominant matrix carbonate phase in the electrolyte composites; and at 600 °C, total conductivities were within the measurement uncertainty. However, below the softening point of the amorphous matrix phase, the conductivity enhancement of SDC - Na_2CO_3 composites could be attributed to interface region (interphase) between SDC and Na_2CO_3 phases.

4.12. HR-Transmission Electron Microscopy Characterization of Composite Electrolytes in Pellet Form

FIB technique was employed to prepare the TEM specimen which can reflect the original microstructure and interfaces in the sintered samples. The 3 D-pin structured TEM sample (Figure 3.48 (a)) revealed the microstructure of the as-sintered composite. The features of this thinned column could be summarized as follows:

1. TEM-BF micrographs revealed that the pin-from structure consisted of two layers: a 3-micrometer thick bright region (self-formed carbonate) and a darker region containing (SDC (HP) -Na_2CO_3 composite). In addition, bright layer (which was probably made up of lower atomic number elements) was very sensitive to e-beam radiation, while the darker layer was quite stable against e-beam exposure.

2. Na_2CO_3 was accumulated at the surface of the cross section where they had a higher chance of absorbing the moisture from the environment. During the FIB sample preparation, the irradiated carbonate phases could have re-precipitated on the surface of the composite; and thus, have formed layers of light colored region.

In order to find out the possible initiating factors for developing carbonate layer on the surface, the freshly made composite was thinned to prepare another specimen. 0.5μm thickness Na_2CO_3 was also observed on this specimen surface (Figure 3.49). The diffraction patterns of brighter and darker layers (Figure 3.50) confirmed amorphous nature of the surface re-precipitated and the polycrystalline nature of SDC (HP) particles, respectively. The carbonate phase constituted the matrix of the darker regions as well (Figure 3.52 (a)). The Figure 3.52 is the bright field image of the composite microstructure where both the particles and matrix phase were intact. Figure 3.53 is an arrangement of micrographs taken with the help of energy filtered imaging where every micrograph showed images built with only signal coming from one element. The highly concentrated carbon rims around the ceria particles suggested that there was happening different region forming around the particles (Figure 3.53). The image made with Na signal (in Figure 3.53 (b)) suggested that Na element was located where SDC particles were (in Figure 3.53 (c)). This could be due to the two facts: (i) in EELS spectra, Na k_α signal and Sm M signal are very close in the spectra *i.e.,* 1075 ev and 1074 ev, respectively [67]. Therefore, sodium map might also show samarium locations. Thus, since the particles are samarium doped ceria, the two signals would overlap. The other reason why sodium and cerium signal were overlapping could be because sodium ions were adsorbed on the oxide particles. New experiments are underway to clarify this confusion. However, the most reliable and accurate elemental analysis information was based on the carbon elemental spectral mapping.

TEM-BF micrographs (Figure. 3.52) together with XRD results supported that a carbonate matrix phase was in an amorphous form. TEM-BF micrographs (Figure 3.52) combined with the elemental spectral mapping (Figure 3.53), supported the schematic illustration for the composite electrolyte in Figure 4.3. In the composite, the ceria particle surface acted as the dissociation agent for the Na_2CO_3. Thus, the Na^+ ion was attracted to the surface of the ceria particle, leaving the liberated CO_3^{2-} ion behind; on the other hand, it may also be possible that the Na^+ ion was incorporated into ceria oxide structure. In order to eliminate the possibility of incorporation of Na in the SDC particle, both EDX results and EELS analysis were performed (Figure 3.54). The analysis was performed on the washed composite powder to remove the surface adsorbed sodium and carbonate phases. The performed EDX investigation result suggested that no Na element was incorporated in the SDC particles. Thus, a highly conducting interphase (which may wrongly be termed interfaces in the existing literature) was formed in the composite between SDC and carbonates. This interphase can lead to positive effects in the conductivity of composite materials at all temperatures However, the strongest impact would be observed at lower temperatures, such as 200 °C-300 °C, since at these temperatures the matrix effect was low.

This could be explained by the schematic illustration in Figure 4.3. Due to the hygroscopic nature of the Na_2CO_3, it absorbed moisture from the ambient environment to form $NaHCO_3$. Therefore, the composite electrolyte material was actually composed of SDC, Na_2CO_3 and $NaHCO_3$. In the composite, the SDC oxide particle acted as the dissociation agent for Na_2CO_3. In the ceria-based composite, the function of the oxide surface was to facilitate the dissociation of Na_2CO_3 (and $NaHCO_3$), *i.e.,* split into Na^+, (H^+) and CO_3^{2-} liberated ion complexes. On the other hand, it may also be possible that the Na^+ ion was incorporated into ceria oxide structure. However, further EDX analysis eliminated possibility of Na element

incorporation into the ceria particles. Thus, the interphase (which was wrongly termed "interface" in the existing literature) was formed in the composite between SDC and carbonates matrix. This interphase could lead to positive effects such as a lower activation energy for ion conduction in the composite materials, especially at lower temperatures, such as 200 °C-300 °C where the matrix contribution to ionic conduction is limited.

4.13. Oxides with Different Surface Charges

In the earlier section, a model for ceria based carbonate composite electrolyte which could be used in LT-SOFC was proposed. Depending on the different oxide nano-particles used, the model might alter. The oxide surface charge was one of the possible factors leading to the enhanced electrical conductivity in the composite. To confirm this possibility, electrical measurements were conducted on composites with various oxide nano-particle fillers. All the composites with different oxides had a fixed Na_2CO_3 concentration.

We examined a list of different oxide particles that included alumina (Al_2O_3), YSZ, silica (SiO_2), titania (TiO_2), YSZ, and Y_2O_3. Some of these oxides were chosen for applications in the ''soggy sand'' model electrolytes for lithium batteries, which had the high ionic conductivity at room temperature [44]. Both mobility and concentration of the charges were expected to significantly influence the resulting liquid-based composite systems. The ionic transport mechanism in ''soggy sand'' electrolytes was originally developed for a heterogeneously doped composite system. In such system, the beneficial influences of insulator dispersions in weak electrolytes were discussed [35,44]. When basic surface charged oxide powders, such as Al_2O_3, were dispersed in LiI solution, Li^+ ions were adsorbed

at the oxide surface. Thus, incorporation of Al_2O_3 lead to an increased vacancy concentration in the Li sub-lattice [36]. On the other hand, in the case of an acidic surface charged oxide dispersion in CaF solution, such as (SiO_2), the F^- ions were adsorbed at the silica surface. Therefore, fluorine ion vacancies were increased due to acidic surface charged SiO_2 oxides. In SDC based nano-composites, which was slightly acidic oxide media, preliminary TEM/EFTEM analysis indicated that Na^+ ions were absorbed at the SDC oxide surfaces. Thus, SDC oxides positively initiated dissociation of sodium carbonate molecule to liberate CO_3^{2-} ions. This greatly facilitates the ions transportation from one side to other side in the composite electrolyte. Therefore, slightly acidic oxide supposed to produce higher ionic conductivity at room temperature, which indeed we observed. The literature reported iso-electric points of the oxides were as follows: SiO_2= 3, TiO_2=5, Al_2O_3=8.5, YSZ=4.7, SDC=6.7-8.6, MgO=12-13, YSZ=8.7, Y_2O_3=11, [64].

In order to increase the accuracy of the evaluation, the iso-electric point measurements were performed using the Malvern Nano-sizer. The zeta potential plots of SDC (N20) and SDC (HP) were reported as a function of pH in Figure 3.56. The iso-electric points of the SDC (N20) and SDC (HP) had pH levels of about 5.8 and 6.2, respectively. Despite having exactly the same chemical formula, smaller the particle size resulted in a surface that was slightly more acidic. The iso-electric points of the Al_2O_3 and TiO_2 were also recorded at the pH levels of 8.3 and 7.1, respectively (Figure 3.57), whereas for SiO_2 the iso-electric point was at a pH level of 2.3 (Figure 3.57).

The influence of different oxide on the electrical properties of the composite was elucidated by comparing electrical property of single phase oxides from literature. The literature values

for Arrhenius conductivity of the pure YSZ, TiO_2, and Al_2O_3 were also included for a comparison in Figure 4.6.

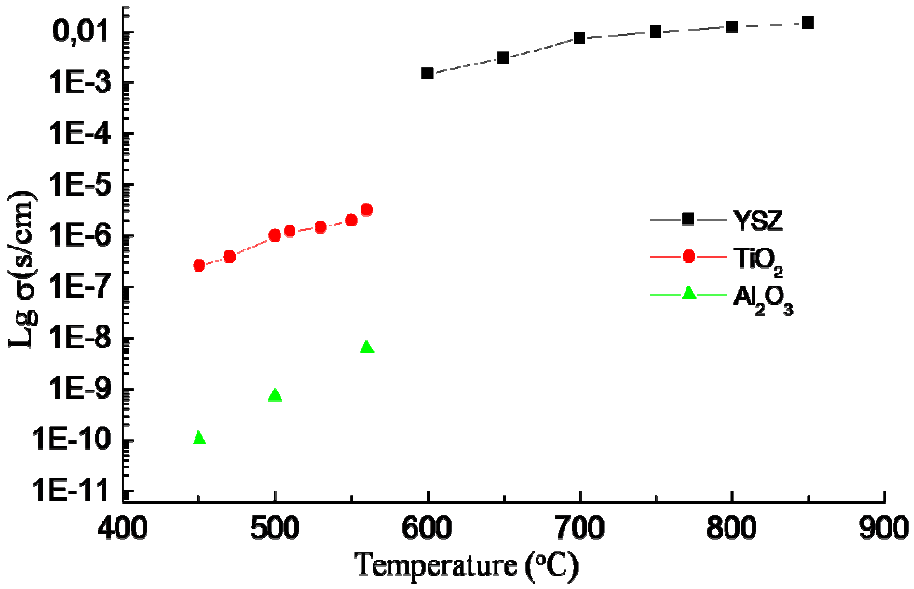

Figure 4.6. Arrhenius plots of the conductivity of YSZ, TiO_2 and Al_2O_3 measured between 200 °C and 900 °C [72-74].

In order to correlate the electrical properties of all the different oxides, the particle sizes were also measured by SEM images (Figure 3.58). The measurements revealed that the average agglomerated particle sizes were in the order of 120 nm-400 nm for the SDC (N20) oxide powder, 66 nm-130 nm for the YSZ oxide powder, and 84 nm-200 nm for the Al_2O_3 oxide powders and 150 nm to 300 nm for TiO_2.

Table 4.2. The measured conductivities and iso-electric points of the oxides.

Oxide	Iso-electric point	σ($S.cm^{-1}$) 600 °C
SDC(N20)	5.8	$6.41x10^{-3}$

SDC(HP)	6.2	$6.41x10^{-3}$
Al_2O_3	8.3	$6.21x10^{-5}$
TiO_2	7.1	$2.66\ x10^{-5}$
SiO_2	2.3	$1.51\ x10^{-7}$
LSGM	≥9	$7.44\ x10^{-5}$
YSZ	8.7	0.00373
MgO	12	$2.21\ x10^{-6}$

In summary, the electrical performances of the alternative oxides were not as good as the composites which were made up of SDC and YSZ oxide powders. According to all the measured conductivity and iso-electric points of the alternative oxide composites (listed in the table 4.2), we still could not conclude a satisfactory correlation between impedance results and alternative oxide surface charges.

CHAPTER 5: CONCLUSION

This study was concluded in four major steps. The findings of each step could be summarized as follows:

1. A systematic research on developing the optimum ratio between SDC to Na_2CO_3, which could provide highest ionic conductivity, was carried out on ceria-based composite electrolyte. Both solutions processed and dry ball-milled composite fabrication procedures were applied and compared. After an comparative evaluation of the micro-structure and electrical properties, dry-ball milled fabrication method was chosen to produce composite electrolytes. The unique feature of the dry-ball milled method was its micro-structures. For instance, SDC particles were uniformly embedded in Na_2CO_3 matrix and Na_2CO_3 covered SDC particles as a rim. In addition, it was shown that constituent phases of the electrolyte (SDC and Na_2CO_3) were distributed homogenously during the dry-ball milling procedure. The carbonate percolation in SDC-based composites was evaluated by EIS and SEM analysis. A uniformly dispersed and homogeneous SDC-Na_2CO_3 nano-composite micro-structure was observed for SDC composite with 10 wt% Na_2CO_3. The impedance curves were analyzed as a function of the carbonate amount in the composite. Phase percolation in the conductivity of the composite was also correlated with the Bruggeman symmetric, effective medium model.

It was shown that the SDC-Na_2CO_3 composite could be sintered at moderately low temperatures, such as, 700 °C for 1 hour. The density of thus sintered composites was in excess of 95% of the theoretical density. Thermal analysis demonstrated that glass transition of the composite occurred in temperature range between 300 °C and 400 °C. Dry ball milling technique was chosen the production of samples. The carbonate phases in the composite were

studied by XRD, SEM, and STA. Our studies showed that with low carbonate concentration, the carbonate phases were invisible in XRD spectra. XRD analysis coupled with SEM imaging and TEM diffraction studies revealed that at least a large portion of the carbonate matrix to be amorphous. However, when the carbonate phases amount were increased up to 20 wt% in the composites, the diffraction peaks belonging to the carbonate phase became visible in the RXD spectra of the composite..

2. AA unique feature of nano-composite electrolyte was the nano-scale interfacial region, associated with the oxide-matrix interface. A higher interfacial area helped to facilitate the ionic conduction behavior in the ceria based nano-composites. The measurements via impedance spectroscopy revealed a significant increase in the ionic conductivity with increasing SSA of SDC particles. For a fixed SDC oxide to carbonate phase amount, the enhancement was attributed to the combined effect of the interface and the surface charge of the oxide leading to the dissociation of Na_2CO_3/$NaHCO_3$ matrix. Once dissociated, one type of ion was absorbed on the oxide surface and the counter ion was liberated to move easier under the influence of the external electrical field. Electron microscopy investigation was employed to address the interface property at nano-scale in nano-composites. Coupled with a series of experimental study on the interface, we proposed a model to elucidate the physical mechanisms.

Overall, the idea of specific design of interface in composites with carbonate matrix was remarkably effective. Our results showed that the knowledge of the matrix system and a proper choice of oxide scaffolding provided high interfacial region and improved ionic transport properties.

3. A characteristic feature of nano-composite electrolyte was the nano-scale interfacial area, and the percolation of the oxide-matrix interface. High interfacial area facilitated enhancing ionic conduction behavior in the nano-composites. The objective of this part was to image the characteristic interface of two phase nano-composite. Consecutively, this part traced the effect of the Na_2CO_3 via multi-scale electron microscopy investigation including SEM and TEM-BF measurements. In order to image the unique interface of the composite, heat-treated pellet was thinned by FIB technique. TEM/EFTEM imaging of the interface were used to support the model for further elucidating the physical mechanisms.

The model proposed here claims that sodium ions are absorbed on the SDC particle surface leaving behind a region of liberated carbonate ions around the particles. This region rich in liberated carbonate ions constitute a fast diffusion pathways for carbonate ion conduction in the composite. When these pathways percolate in the structure at the appropriate carbonate to oxide particle ratio the composite acts as a fast ion conductor.

4. Different oxides (SDC, LSGM, YSZ, TiO_2, Al_2O_3, LSGM, and SiO_2) with different surface charges mixed with 20 wt% Na_2CO_3 were fabricated as the potential candidate composite electrolyte materials. These composites' electrical performances and oxides' iso-electric point were compared. Among these oxides, SDC and YSZ had better electrical performances even though SDC oxide surface was slightly acidic surface and YSZ had a weakly basic surface. However, more analyses are needed to improve to understand the relationship between iso-electric point and electrical performance. Furthermore, detailed electron microscopy and impedance investigations are required to enhance the utilization of other possible oxides in the composite electrolyte and to establish the optimal conditions of a new composite with different oxides.

References

[1] Fuel cell hand book, 7th edition, US department of energy office of fossil energy, national energy technology laboratory, EG&G Technical service, Inc, 2004.

[2] Kordesch, K., Simader, G. Fuel Cell and Their applications. New York. VCH Publishers Inc. 1996.

[3] Carrette, L., Friedrich, K. A., Stimming, U. Fuel Cells 2001; 1: 5.

[4] Chadwick, AV. 2000, Nanotechnology: Solid Progress in Ion Conduction, Nature, 2000; 408 (6815): 925-926.

[5] Barnett, S. A., B. D. Madsen and J. Liu (2003) Direct Hydrocarbon Solid Oxide Fuel Cells, The Electrochemical Society. 2003: 53.

[6] Steele, B. C. H. and A. Heinzel, Materials for Fuel-Cell Technologies, Nature, 2001; 414 (6861): 345-352.

[7] S. G. Chalk, J. F. Miller and F. W. Wagner, Journal of Power Sources. 2000; 86: 40.

[8] M. Cassir, C. Belhomme, Technological Application of Molten Salts: The Case of the Molten Carbonate Fuel Cell, Plasmas & Ions, 1999; 1: 3-15.

[9] L. Carrette, J. Collins, A. Dickinson and U. Stimming, Bunsenmagazin der Deutschen Bunsengesellschaft für Physikalische Chemie, 2000; 27.

[10] Zhu, B., Functional Ceria-Salt-Composite Materials for Advanced IT-SOFC Applications,Journal of Power Sources, 2003; 114 (1):1-9.

[11] H. Jianbing, M. Zongqiang, L. Zhixing, W. Cheng, J. Power Source. 2008; 175: 238.

[12] R. Doshi, V. L. Richards and M. Krumpelt, Proceedings of the 5th International Symposium on Solid Oxide Fuel Cells (SOFC-V), 1997; 379.

[13] B. C. H. Steele, in Ceramic Oxygen Ion Conductors and Their Technological Applications, the Institute of Materials, British Ceramic Proceedings, 1996.

[14] R. Doshi, V. L. Richards, J. D. Carter, X. Wang and M. Krumpelt, Journal of The Electrochemical Society. 1999; 146: 1273.

[15] J. P. P. Huijsmans, F. P. F. van Berkel and G. M. Christie, J. Power Sources. 1998; 107.

[16] R. J. Gorte R.J., AIChE Journal. 2005; 51:2377.

[17] H. G. Dusterwald, B. Hohlein, H. Kraut, J. Meusinger, R. Peters and U. Stimming, Chemical Engineering and Technology. 1997; 20: 617.

[18] H. P. Buchkremer, KFA SOFC-Industrieseminar, KFAJ ülich. 1995; 166.

[19] Namrata Shringare, Bloom's Energy Server™ , Fuel Cell Technology for Green Innovation -Livable New York. Resource Manual, Division of Policy, Research, and Legislative Affairs , New York. 2010.

[20] Ahmed, S., Krumpelt, M. Int. J. Hydrogen Energ. 2001; 26: 291.

[21] Sammes, N. M. in AIChE Spring Natl. Meet., Conf. Proc. 2004.

[22] Brett, D. J. L., Atkinson, A., Brandon, N. P., Skinner, S. J. Chem. Soc. Rev. 2008; 37:1568.

[23] Mc Evoy A. J. Laboratoire de Photonique et des Interfaces. Ecole Polytechnique Fe´derale de Lausanne, Fuel Cell Technology Status and Prospects. 1998.

[24] Inaba, H., Tagawa, H. Solid State Ionics 1996; 83: 1.

[25] Ralph, J. M., Schoeler, A. C., Krumpelt, M. J. Mater. Sci. 2001; 36: 1161.

[26] Yamamoto, O. Electrochim Acta 2000; 45: 2423.

[27] Minh, N.Q., Ceramic Fuel Cells. Journal of the American Ceramic Society,1993; 76(3): 563-588.

[28] Oncel, Cinar. 2009. Novel Production Technique for High Power Density SOFCand Its Essential Key Points. PhD dissertation. Sbanci University.

[29] Mogensen, M., Sammes, N. M., Tompsett, G. A. Solid State Ionics 2000; 129: 63.

[30] Wang, S., Inaba, H., Tagawa, H., Dokiya, M., Hashimoto, T. Solid State Ionics. 1998; 107: 73.

[31] Chaing, Yet-Ming, Dunbar Birnie III, and W.David Kingery, Physical ceramics: principles for ceramic science and engineering, Jhon Wiley & Sons, Inc. 1997

[32] Goodenough, J. B., Huang, Y. Journal of Power Sources 2007; 173: 1.

[33] Fleig, J., Kreuer, K.D., Maier, J., Handbook of Advanced Ceramics, in Materials, Applications and Processing, Academic Press. 2001; 1-60.

[34] Singhal, S.C., Advances in solid oxide fuel cell technology. Solid State Ionics, 2000; 135(1-4): 305-313.

[35] C.C. Liang, J. Electrochem. Soc. 1973; 120: 1289.

[36] Bhattacharyya, A. J., Maier, J. Adv. Mater 2004; 16: 811.

[37] Chung, R. W. J. M., Leeuw, S. W. Solid State Ionics 2004; 175: 851.

[38] Hariharan, K., Maier, J. J. Electrochem. Soc. 1995; 142: 3469.

[39] Lee, J., Adams, S., Maier, J. J. Electrochem. Soc. 2000; 147: 2407.

[40] Maier, J., Reichert, B. Ber. Bunsen-Ges. Phys. Chem. 1986; 90: 666.

[41] Maier, J. J. Phys. Chem. Solids 1985; 46: 309.

[42] A. Bunde, W. Dieterich, H.E.Roman, Phys.rev.lett. 1985; 55: 5.

[43] Maier, J. J. Phys. Chem. 2003; 217: 415.

[44] Anna Jarosik, Uwe Traub, Joachim Maier, and Armin Bunde, Phys. Chem, Phys., 2011;13: 2663-2666.

[45] B. Zhu, Int. J. Energy Res. 2006; 30: 895-903.

[46] B.Zhu, and Mahmnut D.Mat, Int. J. Electrocehm.Sci. 2006; 1: 383-402.

[47] B.Zhu, Int.J.Energy Res. 2009; 33:1126-1137.

[48] M.C. Martin, M.L. Mecartney, Solid state Inoic, 2003; 161: 67-79.

[49] Tscho¨ pe A. Solid State Ionics 2001; 139:267.

[50] Zhu B, Xia CR, Luo XG, Niklasson G. Thin Solid Films 2001; 385:209.

[51] Zhu, B. Key Eng. Mater. 2005; 280-283: 413.

[52] Maier, J. Solid State Ionics 2004; 175: 7.

[53] Tuller, H. L. Solid State Ionics 2000; 131: 143.

[54] Zhu, B., Li, S., Mellander, B. Electrochem. Commun. 2008; 10: 302.

[55] Xiao Di, 2010, PhD thesis, Ionic Conducting Composite as Electrolyte for Low Temperature Solid Oxide Fuel Cells, University of KTH.

[56] Ying Ma, 2009, PhD thesis, Ceria-based Nanocomposite Electrolyte for Low-Temperature Solid Oxide Fuel cells, University of KTH.

[57] C.M. Lapa et al. International Journal of Hydrogen Energy. 2010; 35(7):2953–2957.

[58] L.Qinghua and B. Zhu. Appl. Phys. Lett. 2010; 97: 183115.

[59] Benamira, M., A. Ringuedé, V. Albin, R. N. Vannier, L. Hildebrandt, et al. Journal of Power Sources, 2011;196 (13):5546-5554.

[60] B. Zhu, X.R. Liu, M.T. Sun, S.J. Ji and J.C. Sun, Solid State Sciences 2003; 5: 1127.

[61] W. Xiaodi, M. Ying, R. Raza, M. Muhammed and B. Zhu, Electrochem. Commun. 2008; 10:1617.

[62] G. Abbas, R.Raza, M. Ashraf Ch. B. Zhu, J. Fuel Cell Sci. Technol. Research Papers, 2011; 8: 041013.

[63] Ying Ma, Xiaodi Wang, RizwanRaza, Mamoun Muhammed, Bin Zhu, Journal of Hydrogen Energy, 2010; 35:2580-2585.

[64] James S. Reed, 1995, Ceramic Processing, Wiley-Interscience, 2nd edition.

[65] Peter haines, Principles of Thermal Analysis and Calorimetrry, RSC. 2002.

[66] David Brandon, wayne D. Kaplan, Microstructural Characterization Of Materials, 2nd edition, wiley. 2013.

[67]David B.; Williams, C. Barry Carter, Transmission Electron Microscopy: A Textbook for Materials Science, Springer; 2nd edition. 2009.

[68] Giannuzzi, L.A.; Stevie, F.A.; Introduction Focus Ion beam, Springer, 2005.

[69]R.E. Egerton, Electron Energy Loss Spectroscopy in the electron microscopy, 3rd, Springer, 2011.

[70] Jhon Ferroy, Kazuo Naknoto, Chris W.Brown, Introdcutory Raman Spectroscopy, academic press. 2003.

[71] E.Barsoukov, J. Ross Macdonald , 2nd Edition, John Wiley & Sons. New Jersy. 2005; 252.

[72] Fuel Cell Materials Company Archives, <http://www.fuelcellmaterials.com>

[73] Knauth, H.L. Tuller,J. Appl. Phys.,1999; 85:897–902.

[74] V. Trnovcova´ et al, Solid State Ionics. 2000; 136–137: 11–17.

[75] Z. Tang, Q. Lin, B. Mellander, B. Zhu. Int. J. Hydrogen Energy, 2010; 35: 2970.

[76] Lily, K. Kumari, K. Prasad, and R. Choudhary, Impedance Spectroscopy of $(Na_{0.5}Bi_{0.5})(Zr_{0.25Ti0.75})O_3$ lead-free ceramic, J. Alloy.Comp. 2008; 453 (1–2): 325–331.

[77] E.J. Abram, D.C. Sinclair and A.R. West, J. Electroceramics, 2001; 7(3): 179–188.

[78] P. Heitjans and S. Indris, J. Phys.: Condens. Matter. 2003; 15:1257.

[79] B. Rajaskhar and J.M.C.Plane, Geophysical Research Letters, 1993; 20: 21.

Appendix 1:

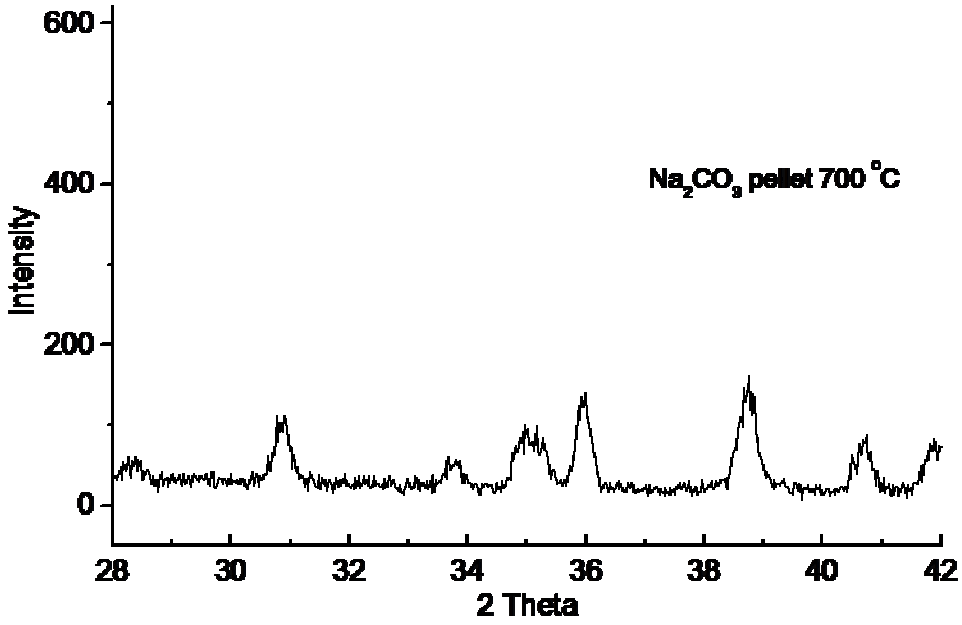

Figure: The room temperature XRD patterns of the Na_2CO_3 after the heat-treatment at 700 °C for 1 hour.

Appendix 2:

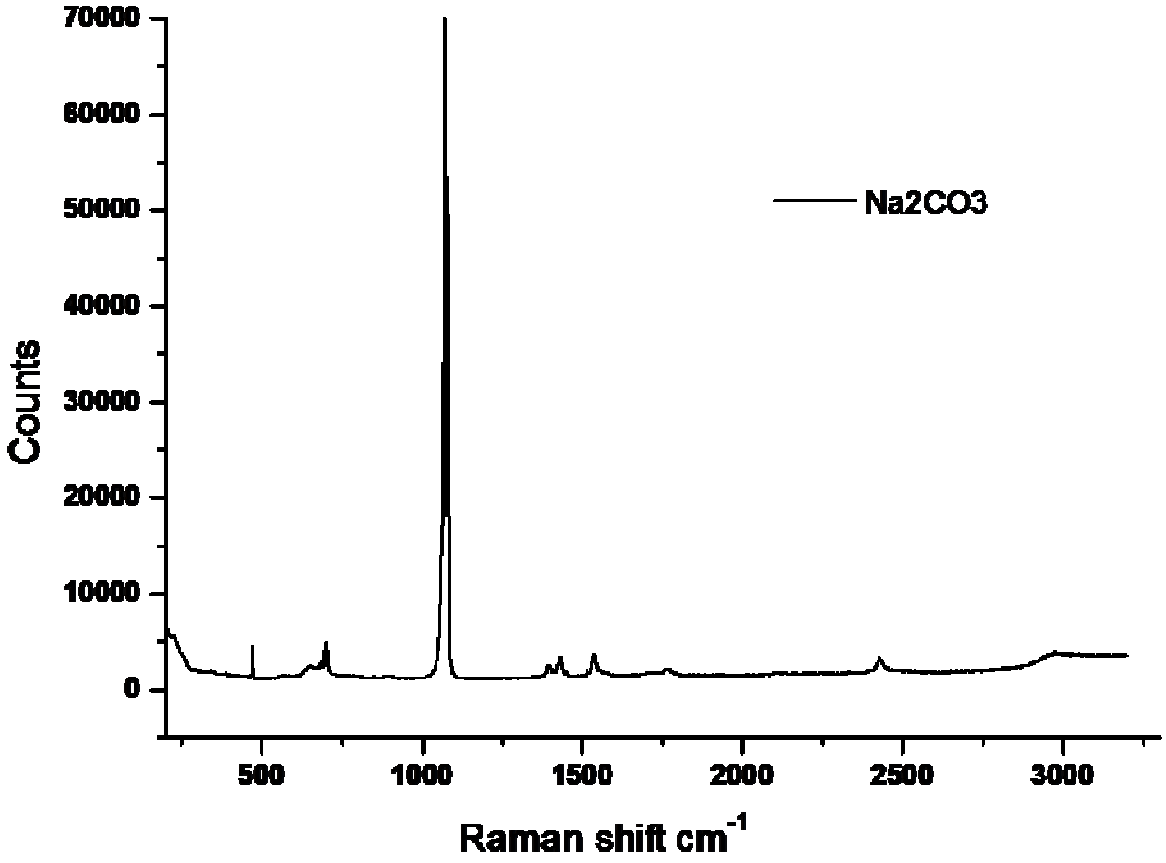

Figure: The Raman patterns of the as received Na_2CO_3.

Appendix 3:

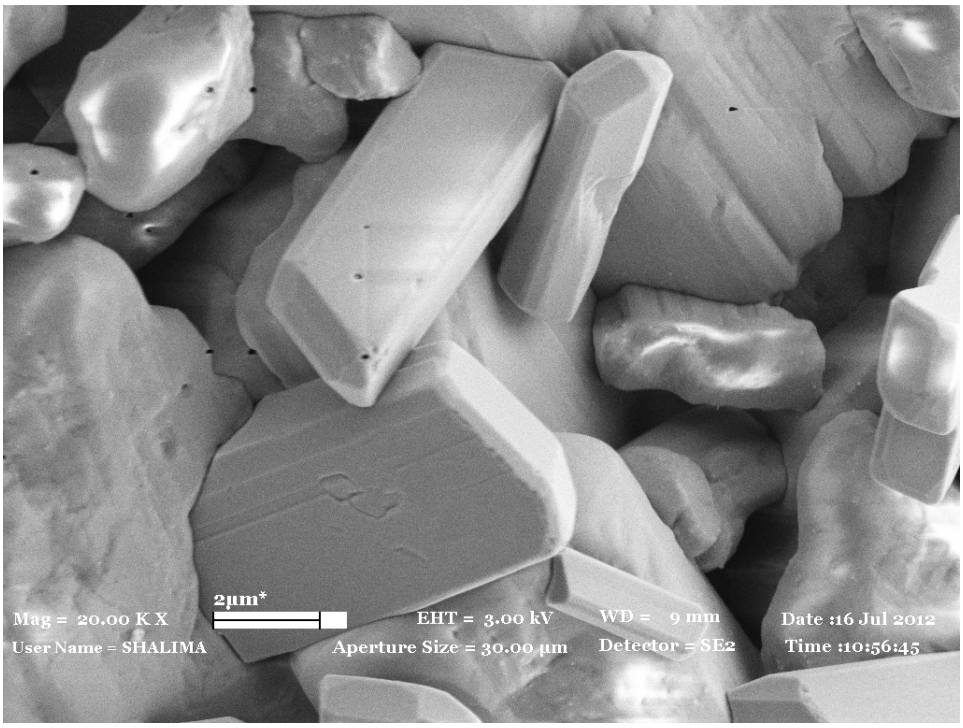

Figure: The SEM of the as-received $NaHCO_3$

Appendix 4:

The composite Impedance	First circle conductivity ($S.cm^{-1}$)	Second circle conductivity ($S.cm^{-1}$)
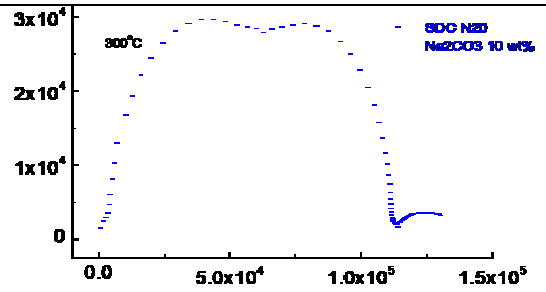	$2.06x10^{-5}$	$2.06x10^{-5}$
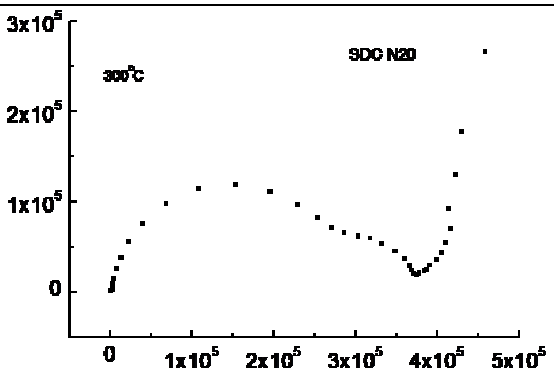	$3.32x10^{-6}$	$1.28x10^{-5}$
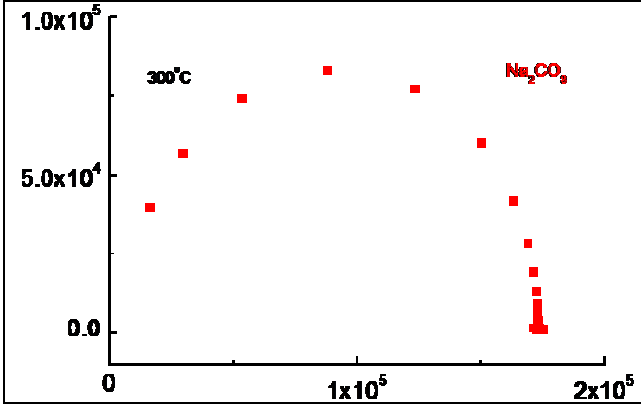	$5.9x10^{-6}$	

Table: Impedance plots of composite SDC (N20) Na_2CO_3 10 tw%, SDC (N2O), and Na_2CO_3 were listed separately with corresponding conductivity values.

Appendix 5:

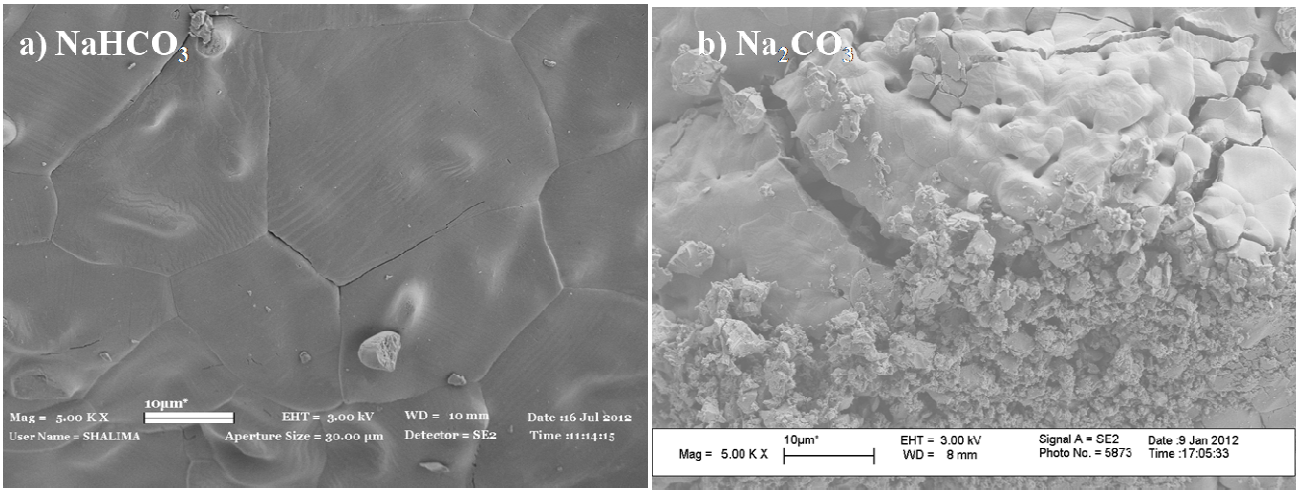

Figure: The SEM of the (a) $NaHCO_3$ and (b) Na_2CO_3 powders (The powders were heat-treated at 700 °C for 1 hour).